Tunnel Field Effect Transistors Based on Two-Dimensional Materials

Jiang Cao

Communauté
UNIVERSITÉ Grenoble Alpes

THÈSE

Pour obtenir le grade de

DOCTEUR DE LA COMMUNAUTE UNIVERSITE GRENOBLE ALPES

Spécialité : **Nano électronique, nano technologies**

Arrêté ministériel : le 6 janvier 2005 - 7 août 2006

Présentée par

Jiang CAO

Thèse dirigée par **Dr. Marco PALA** et
co-encadrée par **Dr. Alessandro CRESTI**

préparée au sein du **Laboratoire IMEP-LAHC**

dans **l'École Doctorale EEATS**

Transistors à effet tunnel à base de matériaux bidimensionnels

Thèse soutenue publiquement le **23 janvier 2017**,
devant le jury composé de :

Prof. Giuseppe IANNACCONE
Professeur, Université de Pise, Pise (Rapporteur)
Dr. Philippe DOLLFUS
Directeur de Recherche, CNRS, C2N, Orsay (Rapporteur)
Dr. Mireille MOUIS
Directeur de Recherche, CNRS, IMEP-LAHC, Grenoble (Président du jury)
Dr. Fabienne MICHELINI
Maitre de conférence, Im2np, Ecole Polytech' Marseille (Examinateur)
Dr. Alessandro CRESTI
Chargé de Recherche, CNRS, IMEP-LAHC, Grenoble (Co-encadrant)
Dr. Marco PALA
Chargé de Recherche, CNRS, C2N, Orsay (Directeur de thèse)

UNIVERSITÉ GRENOBLE ALPES

Abstract

Doctor of Philosophy

Tunnel Field Effect Transistors Based on Two-Dimensional Materials

by Jiang CAO

The successful isolation of graphene in 2004 has attracted great interest to search for potential applications of this unique material and other newborn members of the two-dimensional (2D) family in electronics, optoelectronics, spintronics and other fields. Compared to graphene, the 2D transition metal dichalcogenides (TMDs) have the advantage of being semiconductors, which would allow their use for logic devices. In the past ten years, significant developments have been made in this area, where opportunities and challenges co-exist.

This thesis presents the results of quantum transport simulations of novel 2D-material-based tunnel field-effect transistors for ultra-low-power digital applications. Due to their size, such devices are intrinsically dominated by quantum effects. This requires the adoption of a fairly general theory of transport, such as the nonequilibrium Green's functions (NEGF) formalism, which is a method extensively used for the simulation of electron transport in nanostructures.

In the first part of this thesis, a brief introduction about the 2D materials, their synthesis and applications is presented. Then, the NEGF formalism is concisely reviewed. This approach is applied to the simulation of two different models of vertical tunnel field-effect transistors based on 2D-TMD van der Waal heterojunctions (MoS_2 and WTe_2). To properly describe the system, a coupled effective mass Hamiltonian has been implemented and carefully calibrated to experimental measurements and density functional theory to reproduce the band structure in the energy range of interest for the simulations.

This thesis not only demonstrates the ultra-steep subthreshold slope potentially expected for these devices, but also provides a physical insight into the impact of the transistor geometry on its performances. In the last and more exploratory part of the manuscript, the effect of rotational misalignment within the two layers of the heterostructure is investigated. Experimentally, such a disorder is difficult to avoid, and it can substantially affect the device performances.

Through accurate quantum simulations and deep physical analysis, this study sheds light on the design challenges to be addressed for the development of efficient tunnel field-effect transistors based on 2D materials.

Résumé

L'isolement du graphène a suscité un grand intérêt vers la recherche d'applications potentielles de ce matériau unique et d'autres matériaux bidimensionnels (2D) pour l'électronique, l'optoélectronique, la spintronique et de nombreux autres domaines. Par rapport au graphène, les dichalcogenides de métaux de transition (TMD) 2D offrent l'avantage d'être des semi-conducteurs, ce qui permettrait de les utiliser pour des circuits logiques. Au cours des dix dernières années, de nombreux développements ont déjà été réalisés dans ce domaine où les opportunités et les défis coexistent.

Cette thèse présente les résultats de simulations de transport quantique d'une nouvelle structure de dispositif logique à très faible consommation à base de matériaux bidimensionnels : le transistor à effet tunnel à base d'hétérostructures verticales de TMDs 2D. A cause de leur petite taille, ces dispositifs sont intrinsèquement dominés par des effets quantiques. Par conséquent, l'adoption d'une théorie générale du transport s'impose. Le choix se porte ici sur la méthode des fonctions de Green hors équilibre (NEGF), une approche largement utilisée pour la simulation du transport électronique dans les nanostructures.

Dans la première partie de cette thèse, les matériaux 2D, leur synthèse et leurs applications sont brièvement introduits. Ensuite, le formalisme NEGF est illustré. Cette méthode est ensuite utilisée pour la simulation de deux structures de transistor à effet tunnel vertical basées sur l'hétérojonction van der Waals de MoS_2 et WTe_2. La description du système se base sur un modèle de masse effective calibré avec des résultats ab-initio (afin de reproduire la structure de bandes dans l'intervalle d'énergie intéressé par les simulations de transport) et aux mesures expérimentales de mobilité (pour le couplage électron-phonon). Les résultats non seulement démontrent la possibilité d'obtenir une forte pente sous seuil avec ce type de transistors, mais présentent une étude de la physique qui en détermine les performances en fonction de leur géométrie et de l'interaction entre électrons et phonons. Dans la dernière partie, les effets du malignement rotationnel entre les deux couches 2D sont investigués. Expérimentalement, ce type de désordre est difficile à éviter et peut considérablement affecter les performances du transistor.

Par le moyen de simulations quantiques précises et d'analyses physiques, cette thèse montre les défis à relever dans la conception des transistors à effet tunnel à base de matériaux 2D performants.

Keywords

Quantum transport, non-equilibrium Green's function formalism, electron-phonon interactions, two-dimensional materials, tunnel field effect transistors, van der Waals

Contents

List of Figures

List of Tables

List of Abbreviations

2DEG	2-**d**imensional **e**lectron **g**as
2DM	2-**d**imensional **m**aterial
BTBT	**b**and-**t**o-**b**and **t**unneling
CVD	**c**hemical **v**apor **d**eposition
DFT	**d**ensity **f**unctional **t**heory
DIBL	**d**rain-**i**nduced **b**arrier **l**owering
EMA	**e**ffective **m**ass **a**pproximation
FET	**f**ield-**e**ffect-**t**ransistor
ITRS	**I**nternational **T**echnology **R**oadmap for **S**emiconductors
LDOS	**l**ocal **d**ensity **o**f **s**tates
MOSFET	**m**etal-**o**xide-**s**emiconductor **f**ield-**e**ffect-**t**ransistor
NEGF	**n**on-**e**quilibrium **G**reen's **f**unction
SS	**s**ubthreshold **s**wing
SCE	**s**hort-**c**hannel **e**ffects
TFET	**t**unnel **f**ield-**e**ffect-**t**ransistor
TMD	**t**ransition **m**etal **d**ichalcogenide
SCBA	**s**elf-**c**onsistent **B**orn **a**pproximation
vdW	**v**an-**d**er-**W**aals

List of Symbols

m	Effective electron mass
T	Temperature
I_{D}	Drain current
I_{OFF}	Drain current in off-state
I_{ON}	Drain current in on-state
V_{DS}	Source-drain bias
V_{DD}	Supply voltage
V_{T}	Gate threshold voltage
V_{TG}	Top gate voltage
L_{ext}	Top gate extension length
L_{OV}	Overlap length
T_{BOX}	Bottom oxide thickness
G	Contour-ordered Green's function
G_c	Chronologically time-ordered Green's function
G_a	Anti-chronologically time-ordered Green's function
G^R	Retarded Green's function
G^A	Advanced Green's function
$G^<$	Lesser Green's function
$G^>$	Greater Green's function
Σ	Contour-ordered self-energy
Σ^R	Retarded self-energy
Σ^A	Advanced self-energy
$\Sigma^<$	Lesser self-energy
$\Sigma^>$	Greater self-energy
SS	Subthreshold swing
ϕ	Electrostatic potential
ρ	Charge density

Chapter 1

Introduction

1.1 Trends of micro/nanoelectronics

The invention of the transistor in 1948 is arguably the major technological breakthrough of the 20th century. The transistors are the building blocks of today's microprocessors and computers that are everywhere around us. Nowadays, billions of transistors are integrated on a microchip of only a square centimeter. Since the Nobel prize attributed to Shockley, Brattain and Bardeen in the 1956, and the invention of integrated circuits in the same decade, considerable efforts have been put to keep miniaturizing the metal oxide semiconductor field effect transistors (MOSFETs). A conventional MOSFET structure with descriptions of its working principle are shown in Fig.1.1. From one technology node to the other, MOSFETs are conceived to be smaller (following Moore's law), faster and less power consuming. Thirty years of aggressive scaling have pushed the device dimensions close to the atomic range. The downscaling of MOSFETs has slowed down since the 65 nm node was reached. Issues related to the nanoscale dimensions of the devices started arising.

When the channel length is decreased below 1 μm, additional problems appear and are commonly called short-channel effects (SCEs). The SCEs for the MOSFETs are important when the channel length becomes comparable to the width of the depletion region. When the gate length is scaled down, the gate starts to lose the electrostatic control over the channel, on the other hand the source-drain bias (V_{DS}) gains a larger influence on the barrier. Such an effect is named drain-induced barrier lowering (DIBL). This loss of electrostatic integrity leads to a continue increase of the current and decrease of the off-state potential.

Moreover, the electron mobility is reduced due to collisions with the semiconductor/oxide interface. This surface scattering effect is enhanced by the increase of electric field in the confined regions, which pushes the electrons toward the surface of the device. The reduction of electron mobility is also caused by the necessity of using high doping levels in such scaled MOSFET. Finally, the average velocity of carriers does no longer linearly depend on the electric field in such small devices, which is called the velocity saturation.

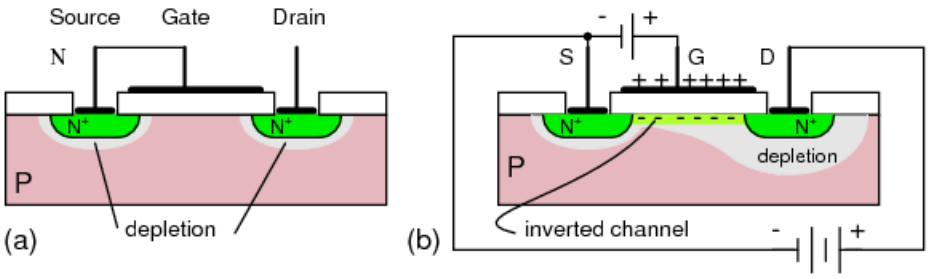

FIGURE 1.1: Schematic cross-section of a N-channel MOSFET: (a) 0 V gate bias, (b) positive gate bias that charges the gate. The P-type substrate below the gate takes on a negative charge. An inversion region with an excess of electrons forms below the gate oxide. This region connects the source and drain N-type regions, forming a continuous N-region from source to drain.

The drawbacks of traditional bulk planar transistors have promoted the search for new architectures alternative to MOSFETs. The International Technology Roadmap for Semiconductors (ITRS) [1], which evaluates the technology requirements for the next-generation semiconductor device technology, predicts that additional new materials and transistor geometries will be needed to successfully address the formidable challenges of transistor scaling in the next 15 years. In Table 1.1, some main figures of merit extracted from the ITRS for the short- (2018) and long-term (2026) technologies, both for high-performance and low-power applications. Since the late '90s, it has been suggested to replace single-gate transistors by multi-gate structures in order to enhance the electrostatic control of the gate. Intel has already switched to the TriGate FET, also known as the FinFET, technology since the 22 nm node. Silicon-on-insulator has also been widely used to improve the performances of transistors, especially decreasing leakage currents [2].

To meet the requirements set by the ITRS for future nodes, scaling down the gate length is critical. The two-dimensional materials (2DMs) provide the ability to control the channel thickness at the atomic level, which will result in improved gate control over the channel and in reduced SCEs. In next Chapter, I will discuss the properties of 2DMs and their numerous possible applications in the electronic devices.

1.2 Power consumption issues

Power consumption is a fundamental problem for nanoelectronic circuits. To give some examples, all the smartphones need to be recharged everyday; the data centers in the US used 91 billion kilowatt-hours of electricity in 2013. The power consumption in logic devices closely depends on the supply voltage (V_{DD}) through the following relation

$$P = \underbrace{\alpha f_c C_L V_{DD}^2}_{\text{operating}} + \underbrace{I_{OFF} V_{DD}}_{\text{stand-by}} , \tag{1.1}$$

TABLE 1.1: Figures of merit extracted from ITRS [1] for the short- (2018) and long-term (2026) technologies, both for high-performance and low-power applications. V_{DD} is the supply voltage; I_{OFF} and I_{ON} are the drain currents per unit width in the off- and on-state; τ is the intrinsic delay time.

	HP2018	**LP2018**	**HP2026**	**LP2026**
Channel length (nm)	10.2	11.7	4.9	5.6
V_{DD} (V)	0.78	0.78	0.66	0.66
I_{OFF} (nA/μm)	100	0.01	100	0.04
I_{ON} (μA/μm)	1,610	556	1,030	337
τ (ps)	0.488	1.564	0.432	1.514

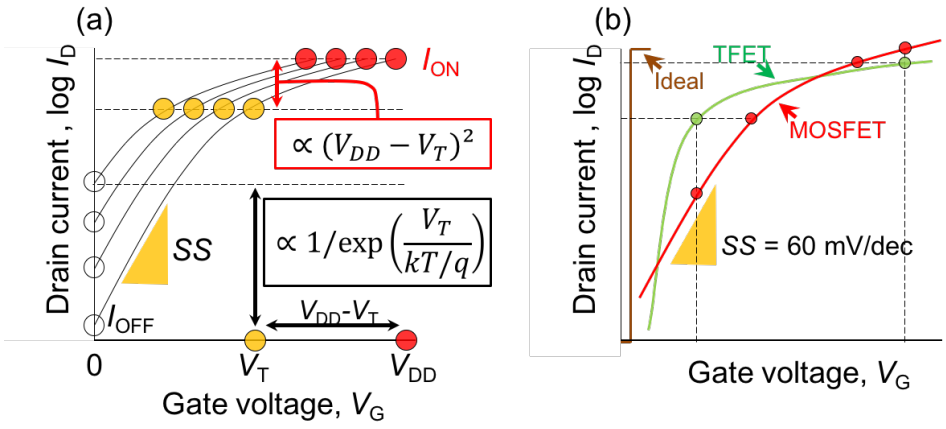

FIGURE 1.2: (a) Transfer characteristics (drain current I_D vs. gate voltage V_G) of a MOSFET switch showing an exponential increase in I_{OFF} because of the thermionic limit of the subthreshold swing SS. Here the simultaneous scaling down of the supply voltage V_{DD} and the threshold voltage V_T, keeping the same I_{ON} by keeping the (V_{DD}-V_T) constant. (b) Qualitative comparison of the MOSFET switch (red) with a TFET (green) which has a steep off-on transition and a lower I_{OFF}. At low V_G, because of the subthermionic SS, the TFET offers a better performance and power reduction. At high V_G, the MOSFET switch becomes a better solution for higher performance thanks to the higher I_{ON}.

where α is called the activity factor, f_c denotes the clock frequency, C_L is the load capacitance (mostly gate and wire capacitance, but also drain and some source capacitances), and I_{OFF} is the off-state current. In the formula above, we can identify an operating and a stand-by power that both depend on V_{DD}. Lowering V_{DD} is thus necessary to decrease the consumption. However, a strong V_{DD} reduction significantly affects the performances of MOSFETs, as illustrated in Fig.1.2(a). Indeed, the problem resides in the speed at which the transistor passes from the off- to the on-states as a function of the gate voltage. In the subthreshold regime of MOSFETs, the thermionic effect entails that at least 60 mV are necessary to increase the current by one order of magnitude at room temperature. In other words, the subthreshold

swing (SS), i.e. the inverse of the derivative of the subthreshold slope

$$\mathrm{SS} = \left(\frac{\partial \log_{10} I_{\mathrm{DS}}}{\partial V_{\mathrm{G}}} \right)^{-1}, \tag{1.2}$$

has a minimum value of

$$\mathrm{SS}_{\mathrm{min}} = \frac{k_B T}{e} \ln(10) = 60 \text{ mV/dec}, \tag{1.3}$$

where k_B is the Boltzmann constant, T is the temperature taken at 300 K and e is the absolute value of electron charge. If we keep the same on-current I_{ON} for the transistor while reducing V_{DD}, then I_{OFF} increases exponentially, see Fig.1.2(a).

A possible way of reducing the voltage supply without performance loss is to increase the turn-on steepness, which means decreasing the average SS below the $\mathrm{SS}_{\mathrm{min}}$. Such devices, called steep-slope switches, are expected to effectively enable power scaling. Because of these MOSFET limitations, other device architectures are under active investigation, including the negative-capacitance FET (NC-FET) and the Tunnel FETs (TFETs) [3].

1.3 Tunnel field-effect transistors

In this work, I focus on the TFETs [4–6]. In contrast to MOSFETs, where charges are thermally injected over a potential barrier, the primary injection mechanism is band-to-band tunneling (BTBT), *i.e.* charge carriers transfer from one energy band into another. This tunneling mechanism was first identified by Zener in 1934 [7].

A typical TFET is composed of a p-i-n structure with a gated intrinsic region, see Fig.1.3(a). Its working mechanism can be explained as follows. When a low voltage is applied to the gate, electrons tunneling from the valence band of the source to the conduction band of the drain is suppressed due to the gap in the intrinsic region, see Fig.1.3(b). This is the off-state. When the potential applied to the gate brings the conduction band of the intrinsic limit at the same level as the source valence band, electrons can easily tunnel from source to drain, see Fig.1.3(b). This is the on-state. In the ideal case, the transition from the off-state to the on-state is very fast, since the thermal tail of the injected electrons is cut by the top of the valence band in the source and the off-current is exponentially suppressed when the source Fermi level is within the gap of the intrinsic region. This would allow, in principle, very low SS, below $\mathrm{SS}_{\mathrm{min}}$, see Figure 1.2(b).

Here, I briefly summarize the history of TFETs. The gated p-i-n structure was proposed in 1978 by Quinn *et al.* [8]. In 1992, Baba [9] fabricated TFETs called surface tunnel transistors in group III-V materials. In 1995, Reddick and Amaratunga [10] reported experiments on silicon surface tunnel transistors. In 2000, Hansch *et al.* [11] published experimental results on a reverse-biased vertical silicon TFET fabricated

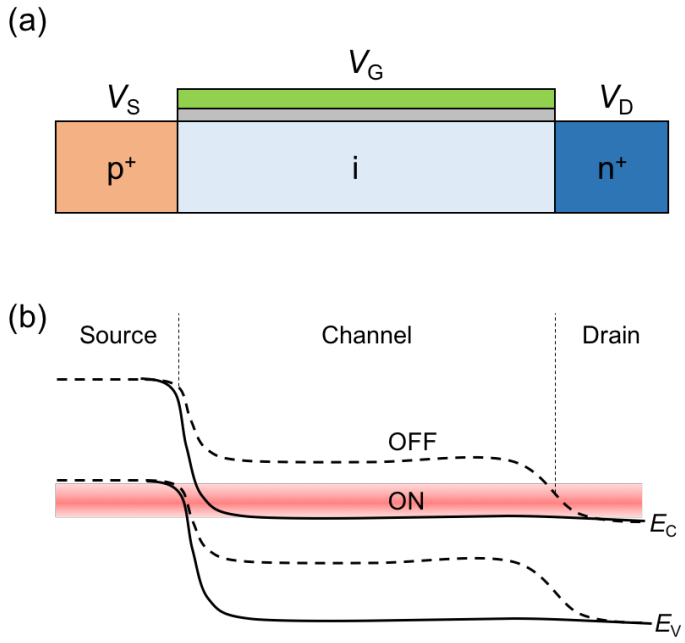

FIGURE 1.3: (a) Schematic cross-section of n-type TFET with applied source (V_S), gate (V_G) and drain (V_D) voltages. (b) Schematic energy band profile for the off-state (dashed lines) and the on-state (solid lines) in a n-type TFET.

by molecular beam epitaxy. Aydin *et al.* [12] fabricated lateral TFETs on silicon-on-insulator in 2004. Recently, TFETs fabricated in various materials (carbon, silicon, SiGe and group III-V materials) have emerged experimentally as the most promising candidates for switches with ultralow standby power and sub-0.5 V supply voltage.

The goals for TFET optimization are to simultaneously achieve the highest possible I_{ON}, the lowest average SS over many orders of magnitude of drain current, and the lowest possible I_{OFF}. For TFETs, SS decreases with the gate voltage, therefore they are naturally optimized for low-voltage operation. To achieve a high tunneling current and a steep slope, the transmission probability of the tunneling barrier should pass from 0 to close to 1 for a small change in gate voltage around the threshold potential. This requires a strong modulation of the channel bands by the gate and a very thin channel barrier.

As mentioned above, there have already been many experimental attempts to build TFET with bulk silicon and III-V group materials. Even though encouraging experimental results have been reported for the on-current and SS in Si- and III–V-based TFETs, these devices are very demanding in terms of gate control [13]. Moreover, their transfer characteristics can be seriously degraded by the presence of interface or bulk defects enabling inelastic trap-assisted tunneling in the OFF-state [14, 15].

The 2-D materials (2DMs) may overcome some of the above issues [16], and have great potential for TFETs, due to their scalability and absence of dangling bonds at interface. They can be stacked to form a new class of tunneling transistors based on an interlayer tunneling occurring in the direction normal to the plane of the 2DMs

[17]. In the next Chapter, I will review the properties of various different 2DMs and their applications in the electronic devices.

1.4 Quantum transport simulations

The fabrication of novel devices is a long and expensive process. Theoretical investigations are then necessary to guide the semiconductor industry toward more efficient architectures. In this work, simulation tools based on state-of-the-art semiconductor physics have been developed for studying and designing future TFETs, with emphasis on 2DMs-based TFETs. To properly describe and model the tunneling current flow in TFETs, we need to develop a simulation approach able to take into account quantum phenomena as well as non-ideality effects due to phonon assisted tunneling. With appropriate simplifications to overcome the computational difficulties, the Non-Equilibrium Green's Function (NEGF) formalism provides a suitable framework to simultaneously treat the quantum transport of coherent carriers and the impact of diffusive phenomena such as electron-phonon interaction.

In the literature, there exists some simulation works on the 2DMs-based TFETs and MOSFETs [18–25]. However the design of the van der Waals TFET (vdW-TFETs) is still largely unexplored [20], because of the complexity to model the interlayer tunneling between the two 2D layers. The effects of electron-phonon scattering on the device performance also need better understanding. My thesis work trys to clarify these questions by implementing the NEGF formalism including the electron-phonon self-energy within the self-consistent Born approximation for the vdW-TFETs.

The theoretical elements of this approach will be reviewed and discussed in Chapter 3, especially with external perturbations *via* the so-called self-energy. In Chapter 4 the numerical implementation of the NEGF formalism is provided. These two Chapters build up the heart of all the calculations carried out in the rest of the thesis. The first application of the developed numerical code is reported and analyzed in Chapter 5, and regards a 2-D TMD-based vertical TFET. In Chapter 6, electron transport in van der Waals TFET (vdW-TFETs) based on MoS_2 and WTe_2 monolayers is studied. In the last years, a special attention has been addressed on the van der Waals tunneling and Esaki diodes [26, 27], and a first device with subthermionic characteristics realized [28]. Then in Chapter 7, an exploratory investigation of the effect of rotational misalignment within stack of 2-D materials will be presented. Experimentally, such a disorder is difficult to avoid, thus the importance to evaluate its influence on the device performance. Finally, Chapter 8 contains the conclusion and outlook of my thesis work.

Chapter 2

Brief Introduction to 2-D Materials

2.1 History of 2-D material research

For a long time, the 2-D materials were thought to be unstable [29]. In the first half of the last century, the scientists predicted [30] that a 2DM would likely disintegrate at finite temperature under the displacement of lattice atoms caused by thermal fluctuations. This theory was further supported by experiments observing that the melting temperature of thin film materials rapidly reduce with decreasing film thickness.

This belief remained unchanged until 2004, when Geim and Novoselov successully isolated graphene by the mechanical exfoliation technique [31, 32]. Although there have been other independent reports of monolayer carbon materials isolation [33, 34] , some even long before the reports from the Manchester group, the works in 2004 and 2005 unveiled the unusual electronic properties of graphene, thus generating an intensive research by physicists and chemists in the field of 2DMs and inspiring 2DMs-based nanoelectronics [35]. Since then, we have seen an exponential increase in the research activity in graphene and other 2DMs (such as the transition metal dichalcogenides, h-BN, black phosphorus, silicene and gemanene) [36–39].

2.2 Basics of 2DMs

In this Section, I summarize the basic properties of 2DMs. Even though our focus will be on TMDs, I start by the presenting the progenitor 2DM (graphene) and also include other materials of technological interest.

2.2.1 Electronic properties of graphene

In 1946, Wallace first calculated the band structure of graphene and showed uncommon semimetallic behavior in this, at that time imaginary, 2-D material [40]. Actually, Wallace's studies of graphene served him as a starting point to study graphite.

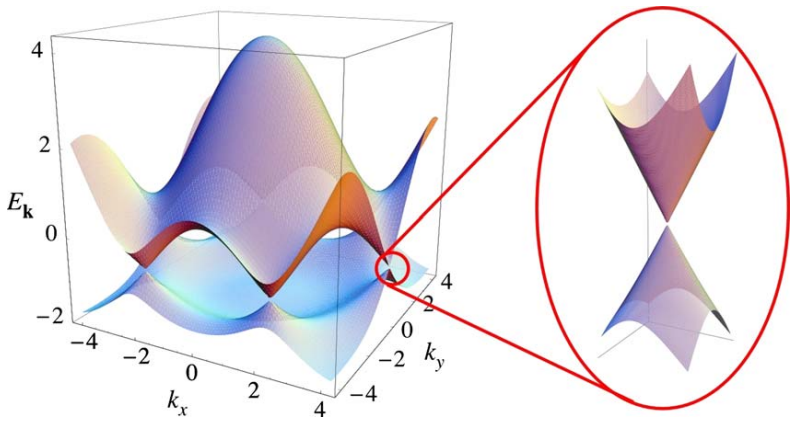

FIGURE 2.1: (Color) Electronic dispersion in the graphene lattice. Left: energy spectrum. Right: zoom in of the energy bands close to one of the Dirac points. Figure adapted from Ref.[35].

Between 1957 and 1958, other works by McClure [41] and Slonczewski and Weiss [42] followed.

One of the most interesting aspects of the graphene is its low-energy band structure [35, 43], which is linear around the K and K' points of the Brillouin zone, see Fig.2.1. In neutral graphene, the Fermi energy crosses exactly these points, which are also called Dirac points, because there electrons can be described by a 2-D Dirac Hamiltonian for masseless fermions, except for the fact that in graphene the electrons move with a speed v_F, which is 300 times smaller than the speed of light, and that the spin degree of freedom in replaced by the so-called pseudospin degree of freedom corresponding to the two graphene sublattices. This determines the observation of very unconventional properties with respect to the usual 2-D electron gases (2DEGs) obtained in doped semiconductor heterostructures. For example, in the presence of a strong magnetic field, Landau levels form at both positive and negative energies (with respect to the Dirac points) at energies proportional to the square root of the magnetic field and of the level index. This gives rise to the anomalous integer quantum Hall effect [44, 45], which, compared to the case of 2DEGs, can be observed at relatively low magnetic field and high temperature, with interesting perspective applications in metrology [46]. The linear dispersion of the graphene energy bands also entails a very high electron mobility, up to 200,000 $\mathrm{cm}^2/(\mathrm{Vs})$ at low temperature for suspended graphene [47].

Another interesting property of graphene is when laterally confined into nanoribbons, its electronic and transport properties are strongly affected by the geometry of the edges (armchair, zigzag or mixed) and the nature of their passivation. For example, under certain condition the ribbon can show a band gap, whose size is proportional to the inverse of the ribbon width. Such a gap might be important for applications in logic devices [48], which are however compromised by the huge mobility degradation due to the increase of the effective mass from one side, and the presence of edge roughness from the other.

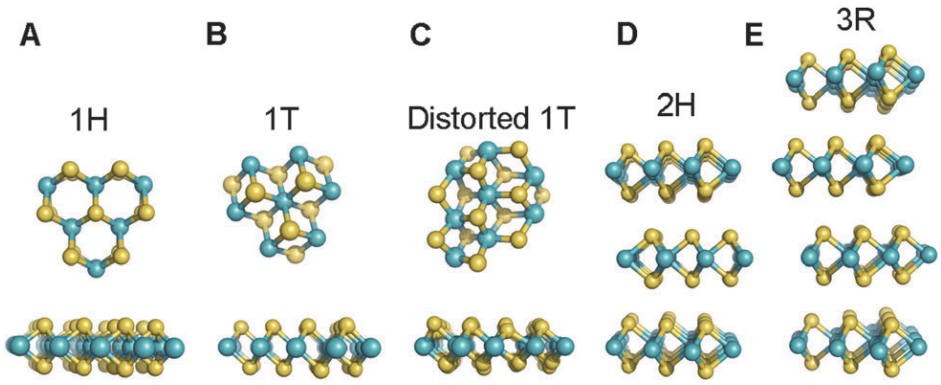

FIGURE 2.2: Different polymorphs or phases of single-layer and stacked single-layer TMDs: (A) 1H phase, (B) ideal (a×a) 1T phase, (C) distorted (2a×a) 1T phase, (D) 2H phase and (E) 3R phase. Figure adapted from Ref.[52].

2.2.2 Crystal structures of other 2DMs

There are more than 40 types [38] of 2-D non-graphene materials making a great range of possible choices. On the basis of chemical composition, they can be divided into the different categories as: TMDs in the form of MX_2 (M stands for transition metal, like Mo, W, Nb, Re, Ni and V, X stands for chalcogens, including S, Se and Te); layered insulator as h-BN; single element materials like black phosphorus (BP), silicene and gemanene; V–VI group of topological insulators (TIs) of Bi_2Te_3,Sb_2Se_3 and Bi_2Se_3; transition metal oxides/hydroxides, such as MoO_3,V_2O_5, $Ni(OH)_2$.

As shown in Fig.2.2, the TMDs has layered structures similar to graphite: covalently bonded 2-D X-M-X layers loosely coupled by weak van der Waals forces [38, 49, 50]. Variation in the stacking sequence leads to five different polymorphs or phases [51, 52]. Among them, 1T and 2H are usually the most stable states. In the 1T phase, metal atoms are coordinated with six neighboring chalcogens, whereas the coordination in 2H is trigonal prismatic [51, 52], see Fig.2.2. In general, the TMDs formed from metals of the groups IVB and VIB show semi-conducting properties, hence they are suitable materials for digital transistor applications.

TIs are materials with an insulating bulk state and a metallic state at the surface or at the edges [53, 54]. TIs are expected to find application in novel spintronic devices [55, 56]. Layered TIs are of great interest for their large surface-to-volume ratio, which favors the manipulations of surface states [57, 58]. Each layer consists of covalently bonded X (Se and Te)-M (Bi and Sb)-X-M-X sheets, and these quintuple layers (with a thickness of about 1 nm) are stacked together by weak van der Waals forces [59].

BP (phosphorene) is another single element layered material besides graphene [60, 61]. Its crystal structure is represented in Fig.2.3. In a layer, each phosphorous atom is covalently bonded with three neighbors forming a zigzag configuration. Weak

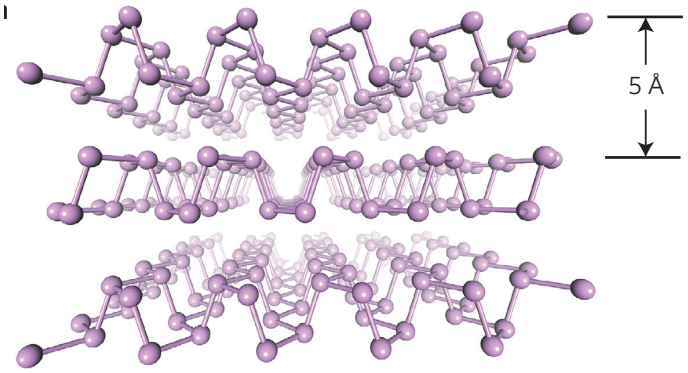

FIGURE 2.3: Atomic structure of monolayer black phosporus. Figure adapted from Ref.[60].

van der Waals forces stack the layers together to form a puckered honeycomb structure. BP has sparkeled great interest [23, 62] for its relatively high charge carrier mobility, tunable gap (depending on the number of layers) and mass anisotropy. Unfortunately, it is not very stable when exposed at air [63].

2.2.3 Electronic properties of 2-D TMDs

Differently from the traditional bulk semiconductors, such as Si and III-V group materials, 2-D TMDs have ultra thin thickness, no surface dangling bonds, and high flexibility, which make them promising candidates [64] to solve the new challenges the semiconductor industry is facing today, including short-channel effects, power dissipation, integration and flexible applications. Recently, one of the large research interests in the field of 2DMs is the understanding of the fundamental electronics properties.

MoS_2 is a typical and well-studied TMD material [49, 65]. Its layers consist of hexagons with the Mo and S_2 atoms located at alternating corners as shown in Fig.2.2. The most striking feature of bulk MoS_2 is that, compared to zero-bandgap graphene and insulating h-BN, it is a semiconductor with an indirect band gap of 1.29 eV [66]. Several studies have confirmed a transition from an indirect band gap to a direct band gap for MoS_2 as the thickness of bulk MoS_2 is decreased to that of a monolayer. Such a similar transition is also demonstrated for other TMD materials. Kuc *et al.* [67] performed an extended study of the influence of quantum confinement on the electronic structures of monolayer and few-layer MS_2 (M = W, Nb, Re) using first-principles calculations. They found that WS_2, which is similar to MoS_2, exhibits an indirect (bulk, E_g=1.3 eV) to direct (monolayer, E_g=2.1 eV) band gap transition. Figure.2.4 shows the band alignment of various monolayer semiconducting TMDs and monolayer SnS_2 obtained from first-principle calculations [68].

Electrical characterizations of single-layer MoS_2 have shown n-type conductivity with a room temperature mobility in the range of 0.5-3 $cm^2/(V\,s)$ [32, 69]. Compared to the mobility 200-500 $cm^2/(V\,s)$ [70] of bulk MoS_2, the mobility of the single-layer

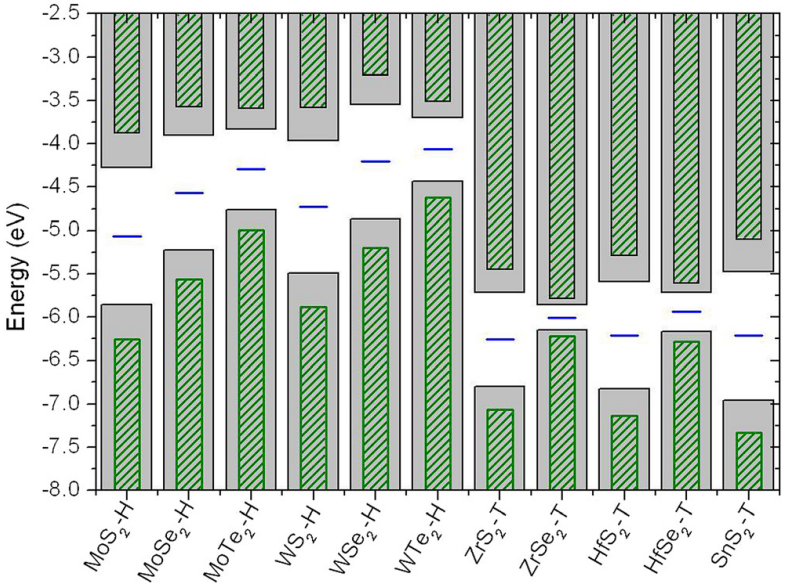

FIGURE 2.4: Band alignment of monolayer semiconducting TMDs and monolayer SnS_2. Conduction band minimum and valence band maximum obtained by DFT calculations are indicated by the filled grey columns. The band edges obtained with the GW correction are indicated by the narrower olive columns. The Fermi level is indicated by the blue horizontal line and the vacuum level is at 0 eV. Figure adapted from Ref.[68].

MoS_2 sheets is rather low and comparable to that of graphene nanoribbons but still much lower than that of either pristine graphene or Si transistors. Because of the low mobility, MoS_2 transistors are probably more suited for low-power applications compared to Si transistors, rather than for high-performance applications.

2.3 Synthesis of 2DMs

The development of efficient synthesis techniques for 2DMs is a fundamental step toward the realization of future applications, especially in the perspective of a large-scale industrial production. The synthesis of 2DMs can follow the top-down approach, such as mechanical exfoliation or chemical exfoliation, or the bottom-up approach, such as chemical vapor deposition (CVD) and, for graphene, vacuum graphitization of SiC. In this section, three key methods for synthesizing single- and few-layer 2DMs will be discussed.

2.3.1 Mechanical exfoliation

The mechanical exfoliation takes advantage of the weak van der Waals forces between layers that make possible individual 2-D layers to be separated. The famous

"scotch tape" method is the first technique used to obtain monolayer graphene [31]. This method is highly flexible and permits the exfoliation of not just graphene, but also other 2DMs such as h-BN, MoS_2, etc [39, 49, 71]. The few-layer, even monolayer 2DMs produced by the mechanical exfoliation method exhibit high purity and cleanliness, very suitable for building single devices and for fundamental research. However, the size of the 2DM sheets that can be obtained is limited to only tens of micrometers. Such a limitation, together with the high time cost of this procedure, makes this approach not suitable for large-scale production. This fabrication method is thus more indicated for preparing 2DMs for laboratory experiments, studying theoretical behavior, or as a reference for benchmarking other synthesis techniques.

2.3.2 Liquid-phase exfoliation

Liquid-phase exfoliation (LPE) is another popular method to obtain individual sheets from bulk materials by breaking the weak van der Waals bonds between the layers. It consists in creating dispersions of 2DMs in diverse solvents with the assistance of sonication [72]. Mixtures of single-layer and multilayered 2DMs are usually produced. Organic solvents [72, 73], such as N-methyl-pyrrolidinone (NMP), isopropanol, low-boiling-point solvent mixture, and lithiumion intercalation are involved in this process. Unfortunately, due to the slow evaporation, it is difficult to remove the solvent from the 2DMs after exfoliation. As a consequence, the structural and electronic quality of LPE-prepared 2DM films is significantly lower than that obtained by mechanical exfoliation or CVD. For MoS_2, annealing at 300 °C can cause a phase change from 1T-MoS_2 to 2H-MoS_2, restoring the Mo atom coordination, and restoring the semiconducting bandgap. The main advantage of LPE approach is that it gives a high yield of monolayers [74]. For a number of applications, for example radio-frequency tags, energy applications, photonic devices, and 2DM-based inks, where large quantities are required, it is possible that LPE will be preferred. Printable 2DM inks can open up new applications and markets, enabling economically viable device manufacturing [75].

2.3.3 Chemical vapor deposition

CVD based techniques offers what is probably the most flexible and promising method to grow large-scale 2DMs, with uniform thickness and high yield.

The successful synthesis of single layer graphene with high homogeneity and reproducibility was achieved in 2009 by low-pressure CVD on copper foils with methane as the carbon source [76]. The graphene growth on Cu is based on several reactions: first dissociation of the hydrocarbon followed by carbon atoms diffusion on the surface leads to nucleation, island growth, and finally completion of a monolayer [77]. This process is justified by the extremely low carbon solubility in Cu even at the growth temperature of about 1040 °C that inhibits the diffusion of C into

the bulk Cu, thus making Cu foil an excellent substrate for the growth of large-area graphene. The graphene grain size could be increased by raising the growth temperature and reducing the partial pressure of methane. One of the main drawbacks of CVD graphene is that it is intrinsically polycrystalline.

In contrast to graphene, other layered systems are composed of two or more elements, which makes the synthesis more complex. Mainly, there are two different approaches to grow the 2DMs by CVD technique. One strategy is to use the 2DM powders as the precursors directly, for example, a straight forward growth method using WSe_2 power as the evaporation source to synthesize monolayer WSe_2 nanosheets [78]. Another strategy is utilizing reaction precursors to grow 2DM through chemical reaction processes, such as sulfurization [79, 80].

2.3.4 Molecular beam epitaxy

Molecular beam epitaxy (MBE) has traditionally been used to grow multicomponent heterostructures of II–VI, III–V and metal oxide materials. MBE can enable the growth of van der Waals heterostructures by allowing the individual components to be chosen on demand, thus achieving good-quality films on different substrates. Results of growing 2DMs, such as graphene [81], $HfSe_2$ [82], $MoSe_2$ [83], WSe_2 [84], *h*-BN [82] etc by MBE have been reported in the very recent years. Heterostructure of graphene/*h*-BN on Co(0001) by MBE was demonstrated by Kelber *et al.* [81] (2016), and has shown good azimuthal registry between each layer. Another heterojunction of $MoTe_2/MoS_2$ has been grown with MBE by Diaz *et al.* [85] (2016), though with high density of line defects due to Te-deficiency during growth. The advantage provided by MBE is the direct growth of different 2DMs layers on top of each other with van der Waals interlayer couplings. This approach will create opportunities for scalable production of the 2-D heterostructures with desirable band alignments that can be useful in the fabrication of future nanoelectronic devices.

2.4 Applications

In recent years, various research teams have reported encouraging results about using the 2DMs to make actual electronic and optoelectronic devices [23, 64, 86, 87]. In this Section, I list some examples of these possible applications and the existing experimental 2DM-based devices. By exploiting the unique properties of 2DMs, those devices can provide interesting performance boosts comparing to the corresponding bulk semiconductor devices. Some novel device structures are also discussed briefly.

2.4.1 Digital applications

Apart from the main technological challenges in geometric scaling, a bigger intrinsic challenge is represented by the material properties: carrier mobility in silicon strongly decreases with body thickness reduction or increased doping, thus undermining possible improvements in the device switching speed. In this context, the 2DMs with their extreme thinness can serve as a convenient alternative. Considering digital electronic applications, graphene-based FETs cannot conform to the ITRS requirements because of its zero band gap, which leads to at most a few tens I_{ON}/I_{OFF} ratio, and large I_{OFF}. Many attempts have been made in order to open an energy gap in graphene, for example by applying a strong electric field over bilayer graphene [88], by quantum confinement in graphene nanoribbons with well-controlled width [89–91], by doping graphene with adatoms like boron atoms [91, 92].

The advantage of 2-D TMDs over graphene is the existence of an energy gap, which is crucial for low I_{OFF} and high I_{ON}/I_{OFF} ratio. Comparing to bulk materials, semiconducting 2-D TMDs have unique features that make them attractive as a channel material for FETs: their atomic thinness, the lack of dangling bonds, and a mobility comparable to Si [93]. One of the earliest uses of TMDs in FETs was reported in 2004, where WSe_2 crystals showed mobility comparable to the best single-crystal Si FETs (up to 500 $cm^2/(Vs)$ for p-type conductivity at room temperature), and a 10^4 I_{ON}/I_{OFF} ratio at a temperature of 60 K [94]. This result was soon followed by devices based on thin films of MoS_2 with a back-gated configuration, resulting in mobility values in the range 0.1–10 $cm^2/(Vs)$ [32, 95].

The first implementation of a top-gated transistor based on monolayer MoS_2 was reported by Kis *et al.* [96], as shown in Fig.2.5. This device showed excellent I_{ON}/I_{OFF} ratio (10^8), n-type conduction, room-temperature mobility of >200 $cm^2/(Vs)$ and SS of 74 mV/dec [96]. The top-gated geometry allowed a reduction in the voltage necessary to switch the device and the integration of multiple devices on the same substrate. The high-k dielectric used in this device, HfO_2, also gave the additional benefit of improving the mobility of monolayer MoS_2. Top-gating with a high-k dielectric was also used in a p-type FET with an active channel made of a monolayer flake of WSe_2, which showed room-temperature hole mobility of 250 $cm^2/(Vs)$, close to 60 mV/dec SS and 10^6 I_{ON}/I_{OFF} ratio [97].

Although 2-D TMDs may not compete with conventional III–V transistors on the mobility values, for devices with very short channel length the transport becomes nearly ballistic, thus mitigating this issue. The ultimate thin body of 2-D TMDs provides high degree of electrostatic control that is important for device scaling and for reducing the SCEs. Furthermore, the relatively large effective mass for electrons and holes in TMDs represents an advantage, since a larger effective mass implies a larger density of states and therefore a larger ballistic I_{ON}. Taking into account the above facts, 2-D TMDs are promising candidates for future digital electronics. Recently, a demonstration of extremely scaled transistor based on a MoS_2 channel and 1-nanometer carbon nanotube gate was successfully implemented by Desai *et*

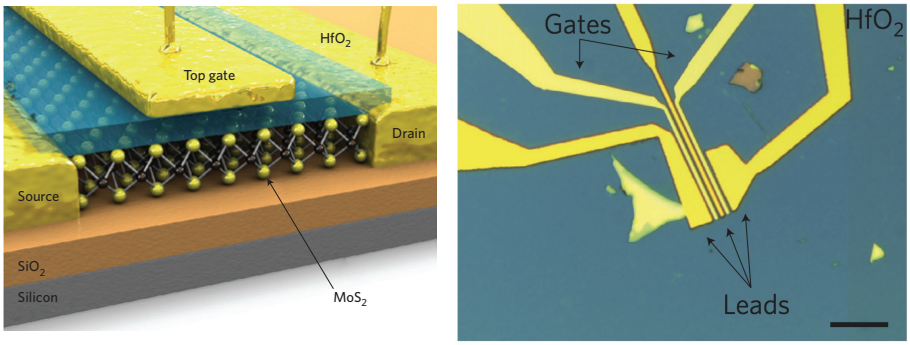

FIGURE 2.5: (left) Schematic illustration of HfO_2-top-gated monolayer MoS_2 FET device. (right) Optical image of a CMOS device based on the structure shown in the left panel. The device consists of two FETs connected in series and defined by three gold leads that serve as source and drain contacts for the two transistors. Figures adapted from Ref.[96].

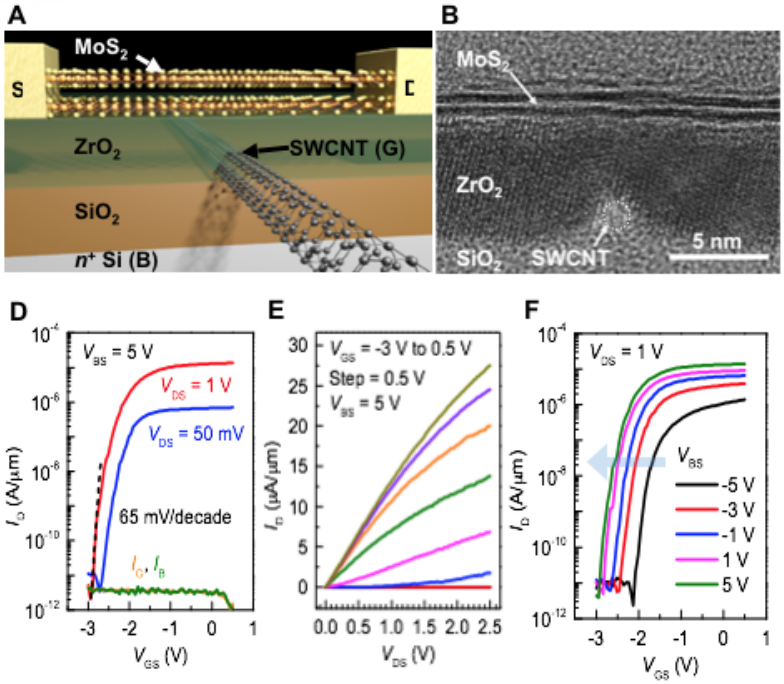

FIGURE 2.6: (A) Schematic and (B) Cross-sectional TEM image of a transistor with a MoS_2 channel and 1-nanometer carbon nanotube gate. (D) I_D-V_{GS} and (E) I_D-V_{DS} characteristics of the device with back-gate bias V_{BS}=5 V. (F) I_D-V_{GS} characteristics at V_{DS}=1 V and varying V_{BS}. Figures adapted from Ref.[98].

al. [98], as shown in Fig.2.6. This device exhibited SS of 65 mV/dec (near ideal value for MOSFET), and I_{ON}/I_{OFF} ratio of 10^6.

In addition to the conventional MOSFET structure, another promising research direction is the stacking of different 2-D layered materials and/or 3-D bulk materials for fabricating vertical heterostructures with novel operation principles [99, 100]. A TFET was demonstrated to work by Britnell *et al.* [101] using two independently

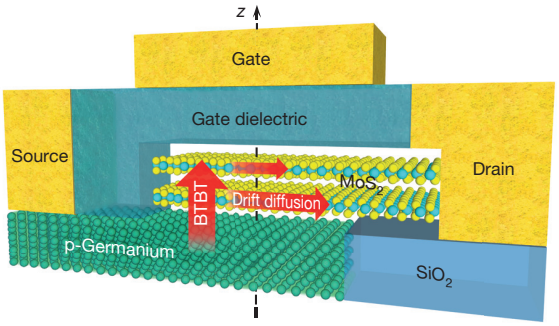

FIGURE 2.7: Schematic of the atomically thin and layered semiconducting-channel TFET with bilayer MoS_2 as the channel and degenerately doped p-type Ge as the source. Figure adapted from Ref.[28].

controlled graphene layers separated by thin hexagonal boron nitride (h-BN) layers acting as tunneling barrier. Recently, a vertical TFET based on bilayer MoS_2 as the channel and degenerately doped p-type Ge as the source, as shown in Fig.2.7, was fabricated by Sarkar *et al.* [28] and showed rather low SS of 31 mV/dec over 4 decades, and quite high on-current in TFETs, with V_{DD} as low as 0.1 V. The van der Waals gap between the 2-D MoS_2 and Ge acts as an extremely thin tunneling barrier, which enhances the tunneling and the on-current.

2.4.2 Analog and high-frequency applications

High-frequency (HF) electronics is currently dominated by III-V and SiGe-based semiconductor transistors with the highest reported maximum oscillation frequency f_{max} values in the range of 1-2 THz, enabling simple circuits to operate up to a few hundred GHz. These technologies are very mature, and the margin left to increase speed is becoming small. Nevertheless, the growing demand for larger bandwidth in communication systems and new sensor applications will need devices to operate in the THz regime.

Parasitic capacitance scaling, high electric mobility, and saturation velocity are the keys to boost device speed. From this perspective, graphene can play a significant role in the HF applications, having shown the highest mobility [102–104] and saturation velocity [105, 106] among any other FET channel material so far. Further, the limit of intrinsic cutoff frequency f_T, well beyond 1 THz, has been predicted through simulation. Tremendous efforts have been carried out to improve the quality of graphene layer and remove possible contaminants during the fabrication process of the devices. During the recent years, the reported f_{max} values of graphene transistors are significantly improving. In a recent work by Wu *et al.* [107], a graphene transistor with 60 nm gate length has experimentally exhibited a f_{max} of 106 and 200 GHz before and after de-embedding respectively. This work shows potential for future improvement in the graphene-based HF transistors. Currently, the f_{max} values of graphene transistors still lie behind III-V and Si-based transistors. A reduction of

the parasitic effects in graphene transistors is needed to increase f_{max} significantly. The absence of a band gap in graphene may prevent proper current saturation and thus limiting f_{max} in the end. Other 2DMs such as MoS_2 show pronounced current saturation and therefore could provide a good alternative to graphene. However, the mobility and saturation velocity in MoS_2 are significantly lower not only than in graphene, but also than in Si and III–V materials [108, 109].

2.4.3 Optoelectronics

Optoelectronic devices (photodetectors, solar cells and LEDs etc.) are electric devices that can generate, detect, interact with light. Due to a large area/volume ratio, strong light–matter interaction and novel electrical properties, optoelectronic devices based on 2DMs have attracted much interest since the beginning.

The direct band gaps of monolayer TMDs make them attractive as light-absorbing materials in alternative thin-film solar cells, including flexible photovoltaics that could coat buildings and curved structures. The first trial was on MoS_2 [110]. This was inspired by the finding that MoS_2 has a direct band gap of about 1.8 eV when its thickness is reduced to a single layer. Lopez-Sanchez *et al.* conducted a landmark research in 2013 [111]. They reduced charged impurities scattering and contact resistance by the careful treatment on a dielectric layer and an annealing process. After these processes, an impressive high responsivity of 880 AW^{-1} was achieved. Stimulated by the pioneering works on MoS_2, photo-detectors based on other TMDs, like $MoSe_2$, WS_2 and WSe_2, have attracted growing attention in recent years [112–114]. In addition, combining different 2-D materials together to form heterostructures may be a possible solution [115, 116].

2.4.4 Flexible electronics

Numerous applications demand the development of large-area, flexible and versatile electronics. For example, wearable electronics requires flexible displays, the cost of installing solar panels could be significantly reduced through the use of roll-to-roll processes, and embedded electronic devices and sensors could start revolution in the healthcare technologies.

2DMs, in general, could be an ideal choice for future flexible electronics. They have excellent mechanical properties [117, 118], can be compatible with flexible device fabrication, and unlike CNTs [119, 120] do not require any sorting process [121]. At the same time, the mobility of 2DMs, when grown over large areas by CVD, can be larger than some of the organic semiconductors [122], thus enabling higher frequency at low power. For transparent conductors, graphene high conductivity and low broadband absorption makes it a promising flexible replacement for the current leading material, indium tin oxide, which is inflexible and increasingly expensive.

The large variety of 2DMs provides a wide selection to choose for device optimization.

Chapter 3

Quantum Transport Model

The non-equilibrium Green's function (NEGF) formalism is one of the most common approaches to describe transport in nanodevices. The concept and the first applications of the NEGF were given by Schwinger [123], Kadanoff and Baym [124], Fujita [125], and Keldysh [126] at the beginning of the 1960s. The main advantages of NEGF are that is it full quantum, adaptable to different Hamiltonian types (effective mass, $k \cdot p$, tight-binding), and able to deal with many-body interactions through the introduction of self-energy operators.

In Section 3.1, I review some of the basic concepts and theorems of quantum mechanics in the second quantization representation, including the evolution operator and the contour ordering. Then in Section 3.2 the NEGF formalism is reviewed, discussing its definition in the time domain, its equation of motion, its stationary solution in the energy domain, the inclusion of scattering, the open boundary conditions and the calculation of observables like charge and current densities. Finally, in Section 3.4, the self-energies of electron-electron and electro-phonon interactions are presented. Several assumptions are made in this work to obtain the final set of equations. For example, I will only consider the steady-state condition and neglect the transient effects. Also, I only include the electron-phonon interactions and neglect other scattering mechanisms such as those due to impurities and surface/edge roughness. For the electron-electron interactions, I use the Hartree approximation that assumes that each electron moves independently and sees only the mean field generated by all the other electrons. The average electrostatic field is obtained from the self-consistent solution of the Poisson equation. Note that the exchange and correlation energies are neglected.

3.1 A brief review of quantum mechanics

I will briefly revise some basics concepts of quantum mechanics that are useful for the understainding of the Green's function method.

3.1.1 Second quantization

To deal with many arbitrary identical particles, such as electrons, we define a collection $\mathcal{F}$ of Hilbert spaces, also known as *Fock space*, according to

$$\mathcal{F} = \{\mathcal{H}_0, \mathcal{H}_1, ..., \mathcal{H}_N, ...\}, \tag{3.1}$$

with $\mathcal{H}_N$ the Hilbert space for N identical particles. Since the probability of finding $M \neq N$ particles in a N-particle ket is zero, any two Hilbert spaces with different numbers of particles are orthogonal between them. The Hilbert space $\mathcal{H}_0$ is the space with *zero* particles. Since an empty system has zero degree of freedom, Hilbert space $\mathcal{H}_0$ contains only one normalized ket, which we denote by $|0\rangle$,

$$\langle 0|0\rangle = 1, \tag{3.2}$$

which just means that the probability of finding nothing in an empty space is 1.

3.1.2 Field operators

Next, we define a *field operator* $\hat{\psi}^\dagger(\mathbf{x}) = \hat{\psi}^\dagger(\mathbf{r}\sigma)$ that generates the position-spin kets by repeated action on the empty ket, i.e.,

$$\begin{aligned} |\mathbf{x}_1\rangle &= \hat{\psi}^\dagger(\mathbf{x}_1)\,|0\rangle \\ |\mathbf{x}_1\mathbf{x}_2\rangle &= \hat{\psi}^\dagger(\mathbf{x}_2)\,|\mathbf{x}_1\rangle = \hat{\psi}^\dagger(\mathbf{x}_2)\hat{\psi}^\dagger(\mathbf{x}_1)\,|0\rangle \\ |\mathbf{x}_1...\mathbf{x}_N\rangle &= \hat{\psi}^\dagger(\mathbf{x}_N)...\hat{\psi}^\dagger(\mathbf{x}_1)\,|0\rangle \end{aligned} \tag{3.3}$$

The field operator $\hat{\psi}^\dagger(\mathbf{x})$ creates a particle in position-spin $\mathbf{x}$. It is therefore called the *creation operator*. Since the position-spin kets change a plus sign under interchange of particles, the creation operator follows that

$$\begin{aligned} \hat{\psi}^\dagger(\mathbf{x}_n)\hat{\psi}^\dagger(\mathbf{x}_m)\,|\mathbf{x}_1...\mathbf{x}_N\rangle &= |\mathbf{x}_1...\mathbf{x}_N\mathbf{x}_m\mathbf{x}_n\rangle = \pm\,|\mathbf{x}_1...\mathbf{x}_N\mathbf{x}_n\mathbf{x}_m\rangle \\ &= \pm\hat{\psi}^\dagger(\mathbf{x}_m)\hat{\psi}^\dagger(\mathbf{x}_n)\,|\mathbf{x}_1...\mathbf{x}_N\rangle \end{aligned} \tag{3.4}$$

where the upper sign in $\pm$ refers to bosons and the lower sign to fermions. This identity is true for any ket $|\mathbf{x}_1...\mathbf{x}_N\rangle$, i.e. for all states in $\mathcal{F}$, and hence

$$\hat{\psi}^\dagger(\mathbf{x}_n)\hat{\psi}^\dagger(\mathbf{x}_m) = \pm\hat{\psi}^\dagger(\mathbf{x}_m)\hat{\psi}^\dagger(\mathbf{x}_n). \tag{3.5}$$

By defining the (anti)commutator between two operator $\hat{A}$ and $\hat{B}$ according to

$$\left[\hat{A}, \hat{B}\right]_\mp = \hat{A}\hat{B} \mp \hat{B}\hat{A}, \tag{3.6}$$

we can rewrite the above relation (3.5) as

$$\left[\hat{\psi}^\dagger(\mathbf{x}_n), \hat{\psi}^\dagger(\mathbf{x}_m)\right]_\mp = 0. \tag{3.7}$$

Corresponding to the operator $\hat{\psi}^\dagger(\mathbf{x})$ there is the adjoint operator $\hat{\psi}(\mathbf{x})$. The operator $\hat{\psi}(\mathbf{x})$ removes a particle from the position-spin $\mathbf{x}$. For this reason, it is called the *annihilation operator*. Below are its properties and how it acts on the position-spin kets.

$$\left[\hat{\psi}(\mathbf{x}_n), \hat{\psi}(\mathbf{x}_m)\right]_\mp = 0 \tag{3.8}$$

$$\hat{\psi}(\mathbf{x}_n)\,|\mathbf{x}_m\rangle = \delta(\mathbf{x}_n - \mathbf{x}_m)\,|0\rangle \tag{3.9}$$

$$\left[\hat{\psi}(\mathbf{x}_n), \hat{\psi}^\dagger(\mathbf{x}_m)\right]_\mp = \delta(\mathbf{x}_n - \mathbf{x}_m) \tag{3.10}$$

3.1.3 Basis transformation

The position–spin is just one possible choice of quantum observables to characterize a particle. The field operator can be used to construct states of many identical particles in which every particle is labeled by general quantum numbers, such as momentum and energy. The one-particle ket $|n\rangle$ can be expanded in the position–spin kets using the completeness relation

$$|n\rangle = \int \mathrm{d}\mathbf{x}\,|\mathbf{x}\rangle\,\langle\mathbf{x}|n\rangle = \int \mathrm{d}\mathbf{x}\varphi_n(\mathbf{x})\,|\mathbf{x}\rangle = \int \mathrm{d}\mathbf{x}\varphi_n(\mathbf{x})\hat{\psi}^\dagger(\mathbf{x})\,|0\rangle\,. \tag{3.11}$$

The ket $|n\rangle$ is obtained by applying to the empty ket $|0\rangle$ the operator

$$\hat{c}_n^\dagger \equiv \int \mathrm{d}\mathbf{x}\varphi_n(\mathbf{x})\hat{\psi}^\dagger(\mathbf{x}), \tag{3.12}$$

i.e., $\hat{c}_n^\dagger\,|0\rangle = |n\rangle$. We may say that $\hat{c}_n^\dagger$ creates a particle with quantum number n. Similarly, if we take the adjoint of (3.12)

$$\hat{c}_n \equiv \int \mathrm{d}\mathbf{x}\varphi_n^*(\mathbf{x})\hat{\psi}(\mathbf{x}), \tag{3.13}$$

we obtain an operator that destroys a particle with quantum number n. The operator $\hat{c}_n$ and $\hat{c}_n^\dagger$ can act on states with arbitrary number of particles. Below are some important relations when the set $\{|n\rangle\}$ forms an orthonormal basis in the one-particle Hilbert space

$$\left[\hat{c}_n, \hat{c}_m^\dagger\right]_\mp = \langle n|m\rangle = \delta_{nm}, \tag{3.14}$$

$$[\hat{c}_n, \hat{c}_m]_\mp = \left[\hat{c}_n^\dagger, \hat{c}_m^\dagger\right]_\mp = 0. \tag{3.15}$$

3.1.4 The density operator

A quantum mechanical system is said to be in a *pure state* if it is in a given state $|\Psi_i\rangle$. On the other hand, a *mixed state* is a statistical ensemble of pure states $\{|\Psi_i\rangle\}$ with probabilities $\{p_i\}$, which have to add to unity

$$\sum_i p_i = 1. \tag{3.16}$$

A mixed state is described by the *density operator*

$$\hat{\rho} = \sum_i p_i \left|\Psi_i\right\rangle\!\left\langle\Psi_i\right|. \tag{3.17}$$

The statistical average of the expectation values of an arbitrary observable $\hat{O}$ can be calculated as

$$\left\langle \hat{O} \right\rangle = \sum_i p_i \left\langle \Psi_i | \hat{O} | \Psi_i \right\rangle = \mathrm{Tr}\left[\hat{\rho}\,\hat{O}\right]. \tag{3.18}$$

When the system is at thermodynamical equilibrium, we can make use of the statistics of the *grand-canonical* ensamble, with given temperature T and chemical potential μ, to write the density operator as

$$\hat{\rho}_{\mathrm{G}}^{\mathrm{eq}} = \frac{e^{-\beta(\hat{H}-\mu\hat{N})}}{\mathcal{Z}_{\mathrm{G}}}, \tag{3.19}$$

where $\beta = 1/k_B T$, $\mathcal{Z}_{\mathrm{G}} = \mathrm{Tr}\left[e^{-\beta(\hat{H}-\mu\hat{N})}\right]$ is the grand-canonical partition function, and $\hat{N}$ is the number operator that counts the particles.

3.1.5 Hamiltonian operator

For our purposes, we consider systems of identical interacting electrons. The Hamiltonian operator can thus be split into two contributions as $\hat{H} = \hat{H}_0 + \hat{V}$, where $\hat{H}_0$ is a single-particle operator that includes the kinetic energy of the electrons and their coupling with the (lattice and external) electrostatic potential

$$H_0(\mathbf{r}) = \phi(\mathbf{r}) + \frac{p^2}{2m_0}, \tag{3.20}$$

while $\hat{V}$ is the two-particle electron-electron (Coulomb) interaction. In the second quantization notation, this Hamiltonian reads

$$\hat{H} = \hat{H}_0 + \hat{V} = \int \mathrm{d}\mathbf{r}\hat{\psi}^\dagger(\mathbf{r}) H_0(\mathbf{r})\hat{\psi}(\mathbf{r}) + \frac{1}{2}\int \mathrm{d}\mathbf{r}\mathrm{d}\mathbf{r}'\hat{\psi}^\dagger(\mathbf{r})\hat{\psi}^\dagger(\mathbf{r}')V(\mathbf{r}-\mathbf{r}')\hat{\psi}(\mathbf{r}')\hat{\psi}(\mathbf{r}). \tag{3.21}$$

3.1.6 Schrödinger equation

The time evolution of a quantum system is governed by the *Schrödinger equation*

$$\mathrm{i}\hbar\frac{\mathrm{d}}{\mathrm{d}t}\left|\Psi(t)\right\rangle = \hat{H}(t)\left|\Psi(t)\right\rangle \tag{3.22}$$

with $|\Psi(t)\rangle$ the state of the system at time t. The Schrödinger equation is a first order differential equation. The state of the system at any time is completely determined once the initial state of the system $|\Psi(t_0)\rangle$ is given. For a time independent Hamiltonian operator $\hat{H}$, Eq.(3.22) is solved by

$$\left|\Psi(t)\right\rangle = e^{-\mathrm{i}\hbar\hat{H}(t-t_0)}\left|\Psi(t_0)\right\rangle . \tag{3.23}$$

3.1.7 Evolution operator and time-ordering

To generalize Eq.(3.23) we look for an *evolution operator* $\hat{U}(t,t_0)$ that transforms $|\Psi(t_0)\rangle$ to $|\Psi(t)\rangle$, i.e.

$$\left|\Psi(t)\right\rangle = \hat{U}(t,t_0)\left|\Psi(t_0)\right\rangle . \tag{3.24}$$

In order to find $\hat{U}(t,t_0)$, we divide the time interval $[t_0,t]$ into equispaced points $\{t_p\}$, with small spacing Δt. By approximating the Hamiltonian operator $\hat{H}(t)$ as constant inside each short time interval $(t_p, t_p+\Delta t)$, we can use Eq.(3.23) repeatedly

$$\left|\Psi(t_{n+1})\right\rangle = e^{-\mathrm{i}\hbar\hat{H}(t_n)\Delta t}e^{-\mathrm{i}\hbar\hat{H}(t_{n-1})\Delta t}\ldots e^{-\mathrm{i}\hbar\hat{H}(t_0)\Delta t}\left|\Psi(t_0)\right\rangle . \tag{3.25}$$

Because the Hamiltonian operators do not generally commute at different times, the ordering in Eq.(3.25) is important. The *chronological ordering operator* $\mathcal{T}$ rearranges the Hamiltonians according to the rule: later times go to the left. We can thus rewrite Eq.(3.25) as

$$\left|\Psi(t_{n+1})\right\rangle = \mathcal{T}\left\{e^{-\mathrm{i}\hbar\Delta t\sum_{p=0}^{n}\hat{H}(t_p)}\right\}\left|\Psi(t_0)\right\rangle . \tag{3.26}$$

Increasing n and reducing Δt, the approximated ket $|\Psi(t_{n+1})\rangle$ approaches the exact one $|\Psi(t)\rangle$ and eventually coincides with it when we replace the summation by the integral

$$\left|\Psi(t)\right\rangle = \mathcal{T}\left\{e^{-\mathrm{i}\hbar\int_{t_0}^{t}\mathrm{d}\tau\hat{H}(\tau)}\right\}\left|\Psi(t_0)\right\rangle . \tag{3.27}$$

The evolution operator in (3.24) is then

$$\hat{U}(t,t_0) = \mathcal{T}\left\{e^{-\mathrm{i}\hbar\int_{t_0}^{t}\mathrm{d}\tau\hat{H}(\tau)}\right\} . \tag{3.28}$$

Now we consider the evolution operator $\hat{U}(t_0,t)$ for $t > t_0$. By definition,

$$\hat{U}(t_0,t)\hat{U}(t,t_0) = \mathbb{1}. \tag{3.29}$$

Taking into account (3.27) we have

$$\hat{U}(t_0,t) = \mathcal{T}^a \left\{ e^{\mathrm{i}\hbar \int_{t_0}^{t} \mathrm{d}\tau \hat{H}(\tau)} \right\}, \tag{3.30}$$

with the *anti-chronological ordering operator* $\mathcal{T}^a$ whose action is to move the operators with later times to the right. The operator $\hat{U}(t_0,t)$ can be interpreted as the operator that evolves a ket backward in time from t to t_0.

3.1.8 Heisenberg picture

In the Heisenberg picture, the states, denoted as $|\Psi_H\rangle$, do not depend on time

$$|\Psi_H\rangle \equiv \hat{U}(t_0,t)\,|\Psi(t)\rangle = |\Psi(t_0)\rangle\,. \tag{3.31}$$

The dependence on time is shifted on operators, which are denoted by $\hat{O}_H$ and defined as

$$\hat{O}_H(t) = \hat{U}(t_0,t)\hat{O}(t)\hat{U}(t,t_0) \tag{3.32}$$

and obey the equation of motion

$$\mathrm{i}\hbar \frac{\mathrm{d}}{\mathrm{d}t}\hat{O}_H(t) = \left[\hat{O}, \hat{H}_H(t)\right]_- + \mathrm{i}\hbar \frac{\partial}{\partial t}\hat{O}_H(t). \tag{3.33}$$

The last term is the derivative with respect to the explicit time dependence of $\hat{O}(t)$.

3.1.9 Contour ordering

In the Heisenberg picture, the expectation value $O(t) \equiv \left\langle \hat{O}(t) \right\rangle$ of an operator $\hat{O}(t)$ over a system prepared in the state $|\Psi_H\rangle$ is given by

$$O(t) = \langle \Psi_H | \hat{U}(t_0,t)\hat{O}(t)\hat{U}(t,t_0) | \Psi_H \rangle\,. \tag{3.34}$$

Equation (3.34) can be interpreted as the evolution of the system from the initial time t_0 until the time t, when the operator $\hat{O}$ acts. Then the evolution is backward from time t to time t_0. The expectation value of a given observable can thus be seen as the result of the system evolution on a *contour*, as represented in Fig.3.1. The upper branch C_1 corresponds to the chronological ordering, while the lower branch C_2 is the anti-chronological ordering. It is now possible to define the *contour ordering operator* $\mathcal{T}_c$ that orders the operators along the contour C in Fig.3.1. The equation (3.34) can be rewritten as

$$O(t) = \langle \Psi_H | \mathcal{T}_c \left\{ e^{\mathrm{i}\hbar \int_C \mathrm{d}\tau \hat{H}(\tau)} \hat{O}(t) \right\} | \Psi_H \rangle\,. \tag{3.35}$$

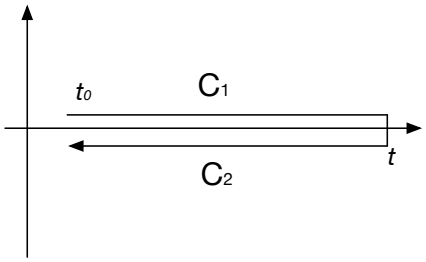

FIGURE 3.1: Time contour used to evaluate the expectation value of a given operator at time t. The system evolves from an initial time t_0 to the time t, after which it returns to the initial time again. The coutour C has thus two branches labeled C_1 and C_2, which run on the axis but for clarity are shown slightly away.

3.2 Non-equilibrium Green's function formalism

At this point, we have all the "ingredients" to define the non-equilibrium Green's function of a quantum mechanical system. Here, I only outline the main results without providing a detailed demonstration. For a more detailed derivation, I refer the reader to dedicated textbooks [127–130]

3.2.1 Definition of Green's function

The one-particle non-equilibrium Green's function, denoted by $G(\mathbf{r},t;\mathbf{r}',t')$, is defined as

$$G(\mathbf{r},t;\mathbf{r}',t') = -\frac{\mathrm{i}}{\hbar}\left\langle \mathcal{T}_c\left\{\hat{\psi}_H(\mathbf{r},t)\hat{\psi}_H^\dagger(\mathbf{r}',t')\right\}\right\rangle \tag{3.36}$$

where $\hat{\psi}_H$ is the field operator in the Heisenberg picture evolving with the Hamiltonian, and $\mathcal{T}_c$ is the contour ordering operator defined in Sec.3.1.9. The Green's function describes the correlation between two points in the space-time $\mathbf{r},t$ and $\mathbf{r}',t'$. For t later than t' on C, $G(\mathbf{r},t;\mathbf{r}',t')$ describes the propagation of a particle created at position $\mathbf{r}'$ and time t' to position $\mathbf{r}$ and time t. Similarly, for t' later on C than t, $G(\mathbf{r},t;\mathbf{r}',t')$ describes the propagation of a hole at position $\mathbf{r}$ and time t to position $\mathbf{r}'$ and time t'.

3.2.2 Equation of motion

To calculate the time evolution of the Green's function in the Heisenberg picture, we derive $G(\mathbf{r},t;\mathbf{r}',t')$ with respect to time t.

$$\begin{aligned}\frac{\mathrm{d}}{\mathrm{d}t}\mathcal{T}_c\left\{\hat{\psi}_H(\mathbf{r},t)\hat{\psi}_H^\dagger(\mathbf{r}',t')\right\} &= \mathcal{T}_c\left\{\frac{\mathrm{d}}{\mathrm{d}t}\hat{\psi}_H(\mathbf{r},t)\hat{\psi}_H^\dagger(\mathbf{r}',t')\right\} + \delta(t-t')\left[\hat{\psi}_H(\mathbf{r},t),\hat{\psi}_H^\dagger(\mathbf{r}',t')\right]_+ \\ &= \mathcal{T}_c\left\{\frac{\mathrm{d}}{\mathrm{d}t}\hat{\psi}_H(\mathbf{r},t)\hat{\psi}_H^\dagger(\mathbf{r}',t')\right\} + \delta(t-t')\delta(\mathbf{r}-\mathbf{r}').\end{aligned} \tag{3.37}$$

Let us consider the Hamiltonian operator $\hat{H} = \hat{H}_0 + \hat{V}$ defined in (3.21). To evaluate (3.37), it is necessary to express the derivative of the field operator $\hat{\psi}_H(\mathbf{r}, t)$ with respect to time t

$$\mathrm{i}\hbar\frac{\mathrm{d}}{\mathrm{d}t}\hat{\psi}_H(\mathbf{r},t) = \left[\hat{\psi}_H(\mathbf{r},t), \hat{H}_H(t)\right]_- = H_0(\mathbf{r})\hat{\psi}_H(\mathbf{r},t) + \int \mathrm{d}\mathbf{r}_1 V(\mathbf{r}-\mathbf{r}_1)\hat{\psi}_H^\dagger(\mathbf{r}_1,t)\hat{\psi}_H(\mathbf{r}_1,t)\hat{\psi}_H(\mathbf{r},t). \tag{3.38}$$

By means of Eq.(3.38), the time derivative of the non-equilibrium Green's function can be obtained. The result yields the equation of motion for $G(\mathbf{r}, t; \mathbf{r}', t')$

$$\begin{aligned}\left(\mathrm{i}\hbar\frac{\mathrm{d}}{\mathrm{d}t} - H_0(\mathbf{r})\right)G(\mathbf{r},t;\mathbf{r}',t') &= \delta(t-t')\delta(\mathbf{r}-\mathbf{r}') \\ &\quad - \mathrm{i}\int \mathrm{d}\mathbf{r}_1 \int_C \mathrm{d}t_1 V(\mathbf{r}-\mathbf{r}_1)\delta(t_1-t)G^{(2)}(\mathbf{r}_1,t_1,\mathbf{r},t;\mathbf{r}_1,t_1,\mathbf{r}',t'),\end{aligned} \tag{3.39}$$

where $G^{(2)}$ is the *two-particle* Green's function

$$G^{(2)}(\mathbf{r}_1,t_1,\mathbf{r},t;\mathbf{r}_1,t_1,\mathbf{r}',t') = -\frac{1}{\hbar}\left\langle \mathcal{T}_c\left\{\hat{\psi}_H(\mathbf{r}_1,t_1)\hat{\psi}_H(\mathbf{r},t)\hat{\psi}_H^\dagger(\mathbf{r}_1,t_1)\hat{\psi}_H^\dagger(\mathbf{r}',t')\right\}\right\rangle. \tag{3.40}$$

By differentiating the two-particle Green's function (3.40), we get an equation of motion containing the three-particle Green's function, whose equation of motion depends on the four-particle Green's function, and so on.

Equation (3.39) gives us a clear view of why G is called the *Green's function*, since G describes the impulse response, of both time and space, for the given Schrödinger equation.

3.2.3 Self-energy

Instead of solving the infinite hierarchy of the Green's functions, the irreducible self-energy is introduced, which is represented with the symbol Σ, and which is a functional of the single-particle Green's function G. We can replace

$$-\mathrm{i}V(\mathbf{r}-\mathbf{r}_1)\delta(t_1-t)G^{(2)}(\mathbf{r}_1,t,\mathbf{r},t;\mathbf{r}_1,t,\mathbf{r}',t') \Rightarrow \Sigma(\mathbf{r},t,\mathbf{r}_1,t_1)G(\mathbf{r}_1,t_1;\mathbf{r}',t') \tag{3.41}$$

into (3.39) to get

$$\begin{aligned}\left(\mathrm{i}\hbar\frac{\mathrm{d}}{\mathrm{d}t} - H_0(\mathbf{r})\right)G(\mathbf{r},t;\mathbf{r}',t') &= \delta(t-t')\delta(\mathbf{r}-\mathbf{r}') \\ &\quad - \int \mathrm{d}\mathbf{r}_1 \int_C \mathrm{d}t_1 \Sigma(\mathbf{r},t,\mathbf{r}_1,t_1)G(\mathbf{r}_1,t_1;\mathbf{r}',t').\end{aligned} \tag{3.42}$$

3.2.4 Other Green's functions

The Green's function G is defined by the contour ordering along the contour C shown in Fig.3.1. Since it is not obvious to keep track of the time-branch in the evaluation of the integral, four new Green's functions are defined

$$G(\mathbf{r},t;\mathbf{r}',t') = \begin{cases} G_c(\mathbf{r},t;\mathbf{r}',t') & t,t' \text{ on } C_1, \\ G_a(\mathbf{r},t;\mathbf{r}',t') & t,t' \text{ on } C_2, \\ G^<(\mathbf{r},t;\mathbf{r}',t') & t \text{ on } C_1, t' \text{ on } C_2, \\ G^>(\mathbf{r},t;\mathbf{r}',t') & t \text{ on } C_2, t' \text{ on } C_1, \end{cases} \tag{3.43}$$

with G_c the chronologically time-ordered Green's function, G_a the anti-chronologically time-ordered Green's function, $G^<$ the lesser Green's function and $G^>$ the greater Green's function. These four functions are not independent since $G_c+G_a = G^>+G^<$. As we will see, the greater and lesser Green's functions are directly related to the hole density and electron density in the system. We also define the advanced and retarded Green's functions

$$\begin{aligned} G^A &= G_c - G^>, \\ G^R &= G_c - G^<, \end{aligned} \tag{3.44}$$

with

$$G^R - G^A = G^> - G^<. \tag{3.45}$$

We can define the same quantities for the Σ self-energy leading to the lesser $\Sigma^<$, the greater $\Sigma^>$, the advanced Σ^A and the retarded Σ^R self-energies. We also have the relation

$$\Sigma^R - \Sigma^A = \Sigma^> - \Sigma^<. \tag{3.46}$$

In the equation of motion (3.42), we need to deal with terms of the form

$$D(t,t') = \int_C \mathrm{d}t_1 A(t,t_1)B(t_1,t'), \tag{3.47}$$

where C is the contour of Fig.3.1. The lesser $D^<$ and retarded D^R quantities of the D function is provided by the Langreth's rules [131]

$$\begin{aligned} D^<(t,t') &= \int_t^{t'} \mathrm{d}t_1 [A^R(t,t_1)B^<(t_1,t') + A^<(t,t_1)B^A(t_1,t')], \\ D^R(t,t') &= \int_t^{t'} \mathrm{d}t_1 A^R(t,t_1)B^R(t_1,t'). \end{aligned} \tag{3.48}$$

Therefore the equation of motion for the other Green's functions with respect to time t become

$$\left(\mathrm{i}\hbar\frac{\mathrm{d}}{\mathrm{d}t} - H_0(\mathbf{r})\right) G^R(\mathbf{r},t;\mathbf{r}',t') = \delta(t-t')\delta(\mathbf{r}-\mathbf{r}') - \int \mathrm{d}\mathbf{r}_1 \int_{t_0}^{\infty} \mathrm{d}t_1 \Sigma^R(\mathbf{r},t,\mathbf{r}_1,t_1) G^R(\mathbf{r}_1,t_1;\mathbf{r}',t'), \tag{3.49}$$

$$\left(\mathrm{i}\hbar\frac{\mathrm{d}}{\mathrm{d}t} - H_0(\mathbf{r})\right) G^A(\mathbf{r},t;\mathbf{r}',t') = \delta(t-t')\delta(\mathbf{r}-\mathbf{r}') - \int \mathrm{d}\mathbf{r}_1 \int_{t_0}^{\infty} \mathrm{d}t_1 \Sigma^A(\mathbf{r},t,\mathbf{r}_1,t_1) G^A(\mathbf{r}_1,t_1;\mathbf{r}',t'), \tag{3.50}$$

$$\left(\mathrm{i}\hbar\frac{\mathrm{d}}{\mathrm{d}t} - H_0(\mathbf{r})\right) G^<(\mathbf{r},t;\mathbf{r}',t') = \int \mathrm{d}\mathbf{r}_1 \int_{t_0}^{\infty} \mathrm{d}t_1 \Sigma^R(\mathbf{r},t,\mathbf{r}_1,t_1) G^<(\mathbf{r}_1,t_1;\mathbf{r}',t') + \Sigma^<(\mathbf{r},t,\mathbf{r}_1,t_1) G^A(\mathbf{r}_1,t_1;\mathbf{r}',t'), \tag{3.51}$$

$$\left(\mathrm{i}\hbar\frac{\mathrm{d}}{\mathrm{d}t} - H_0(\mathbf{r})\right) G^>(\mathbf{r},t;\mathbf{r}',t') = \int \mathrm{d}\mathbf{r}_1 \int_{t_0}^{\infty} \mathrm{d}t_1 \Sigma^A(\mathbf{r},t,\mathbf{r}_1,t_1) G^>(\mathbf{r}_1,t_1;\mathbf{r}',t') + \Sigma^>(\mathbf{r},t,\mathbf{r}_1,t_1) G^R(\mathbf{r}_1,t_1;\mathbf{r}',t'). \tag{3.52}$$

3.2.5 Steady-state condition

Under steady-state condition, the Green's functions depend on time difference $\tau = t - t'$. We can Fourier transform the time difference coordinate τ to energy

$$G^{R,A,<,>}(\mathbf{r},\mathbf{r}';E) \equiv \int \frac{\mathrm{d}\tau}{\hbar} e^{\mathrm{i}E\tau/\hbar} G^{R,A,<,>}(\mathbf{r},\mathbf{r}';\tau), \tag{3.53}$$

and also for the self-energies

$$\Sigma^{R,A,<,>}(\mathbf{r},\mathbf{r}';E) \equiv \int \frac{\mathrm{d}\tau}{\hbar} e^{\mathrm{i}E\tau/\hbar} \Sigma^{R,A,<,>}(\mathbf{r},\mathbf{r}';\tau). \tag{3.54}$$

The equations (3.49-3.52) then becomes

$$(E - H_0(\mathbf{r}))\, G^R(\mathbf{r},\mathbf{r}';E) = \delta(\mathbf{r}-\mathbf{r}') - \int \mathrm{d}\mathbf{r}_1 \Sigma^R(\mathbf{r},\mathbf{r}_1;E) G^R(\mathbf{r}_1,\mathbf{r}';E), \tag{3.55}$$

$$(E - H_0(\mathbf{r}))\, G^A(\mathbf{r},\mathbf{r}';E) = \delta(\mathbf{r}-\mathbf{r}') - \int \mathrm{d}\mathbf{r}_1 \Sigma^A(\mathbf{r},\mathbf{r}_1;E) G^A(\mathbf{r}_1,\mathbf{r}';E), \tag{3.56}$$

$$(E - H_0(\mathbf{r}))\, G^<(\mathbf{r},\mathbf{r}';E) = \int \mathrm{d}\mathbf{r}_1 \Sigma^R(\mathbf{r},\mathbf{r}_1;E) G^<(\mathbf{r}_1,\mathbf{r}';E) + \Sigma^<(\mathbf{r},\mathbf{r}_1;E) G^A(\mathbf{r}_1,\mathbf{r}';E), \tag{3.57}$$

$$(E - H_0(\mathbf{r}))\, G^{>}(\mathbf{r}, \mathbf{r}'; E) = \int \mathrm{d}\mathbf{r}_1 \Sigma^{A}(\mathbf{r}, \mathbf{r}_1; E) G^{>}(\mathbf{r}_1, \mathbf{r}'; E) + \Sigma^{>}(\mathbf{r}, \mathbf{r}_1; E) G^{R}(\mathbf{r}_1, \mathbf{r}'; E). \tag{3.58}$$

3.3 Observables

The Green's functions allows us to obtain the average value of important observable quantities, as the charge and the current.

3.3.1 Charge

The lesser $G^{<}$ and greater $G^{>}$ Green's functions are related directly to the observables. The electron and hole concentration are respectively given by

$$n(\mathbf{r}, t) = \left\langle \hat{\psi}^{\dagger}(\mathbf{r}, t) \hat{\psi}(\mathbf{r}, t) \right\rangle = -\mathrm{i}\hbar G^{<}(\mathbf{r}, t; \mathbf{r}, t), \tag{3.59}$$

$$p(\mathbf{r}, t) = \left\langle \hat{\psi}(\mathbf{r}, t) \hat{\psi}^{\dagger}(\mathbf{r}, t) \right\rangle = +\mathrm{i}\hbar G^{>}(\mathbf{r}, t; \mathbf{r}, t). \tag{3.60}$$

Under the steady-state condition, the relations can be expressed in the energy domain

$$n(\mathbf{r}) = -\mathrm{i} \int \frac{\mathrm{d}E}{2\pi} G^{<}(\mathbf{r}, \mathbf{r}; E), \tag{3.61}$$

$$p(\mathbf{r}) = +\mathrm{i} \int \frac{\mathrm{d}E}{2\pi} G^{>}(\mathbf{r}, \mathbf{r}; E). \tag{3.62}$$

The total space charge density is therefore given by

$$\rho(\mathbf{r}) = e[p(\mathbf{r}) - n(\mathbf{r}) + N_D(\mathbf{r}) - N_A(\mathbf{r})] \tag{3.63}$$

where e is the absolute value of the electron charge, N_D and N_A are the donors and acceptors concentrations.

3.3.2 Local density of states

The retarded G^R and advanced G^A Green's functions define the spectral function as

$$A(\mathbf{r}, \mathbf{r}'; E) = \mathrm{i}[G^{R}(\mathbf{r}, \mathbf{r}'; E) - G^{A}(\mathbf{r}, \mathbf{r}'; E)]. \tag{3.64}$$

The spectral function provides information about the nature of the allowed electronic states, regardless of whether they are occupied or not, and can be considered as a generalized density of states. The diagonal elements of the spectral function

give the local density of states (LDOS)

$$D(\mathbf{r}, E) = \frac{1}{2\pi} A(\mathbf{r}, \mathbf{r}; E). \tag{3.65}$$

Therefore the trace of the spectral function gives the density of states

$$N(E) = \mathrm{Tr}[A(E)] = \int \mathrm{d}\mathbf{r} A(\mathbf{r}, \mathbf{r}; E). \tag{3.66}$$

3.3.3 Current

To determine the current density, we use the continuity equation to build a relationship between the current density $\vec{J}$ and the charge density ρ

$$\frac{\mathrm{d}}{\mathrm{d}t}\rho(\mathbf{r}) + \nabla_{\mathbf{r}} \cdot \vec{J} = 0. \tag{3.67}$$

To obtain the time derivative of the charge density, we can proceed by deriving the lesser Green's function $G^<$ with respect to t and t'. Using the Eq.(3.51), we obtain

$$\mathrm{i}\hbar(\frac{\mathrm{d}}{\mathrm{d}t} + \frac{\mathrm{d}}{\mathrm{d}t'})G^<(\mathbf{r}, t; \mathbf{r}', t') = [H_0(\mathbf{r}) - H_0(\mathbf{r}')]G^<(\mathbf{r}, t; \mathbf{r}', t'), \tag{3.68}$$

by assuming that the terms containing self-energies must vanish so that the momentum and the energy are also conserved [124]. Using such a relation one can write

$$\begin{aligned} \frac{\mathrm{d}}{\mathrm{d}t}\rho(\mathbf{r}, t) &= \lim_{\mathbf{r}' \to \mathbf{r}, t' \to t} (-\mathrm{i}\hbar e)(\frac{\mathrm{d}}{\mathrm{d}t} + \frac{\mathrm{d}}{\mathrm{d}t'})G^<(\mathbf{r}, t; \mathbf{r}', t') \\ &= -e \lim_{\mathbf{r}' \to \mathbf{r}} [H_0(\mathbf{r}) - H_0(\mathbf{r}')]G^<(\mathbf{r}, t; \mathbf{r}', t) = \nabla_{\mathbf{r}} \cdot \vec{J}. \end{aligned} \tag{3.69}$$

Recalling the definition of the single particle Hamiltonian $H_0(\mathbf{r})$

$$H_0(\mathbf{r}) = \phi(\mathbf{r}) + \frac{p^2}{2m_0} = \phi(\mathbf{r}) + \frac{\hbar}{2m_0}\nabla^2_{\mathbf{r}}, \tag{3.70}$$

Eq.(3.69) can be written as

$$\begin{aligned} \nabla_{\mathbf{r}} \cdot \vec{J} &= \frac{e\hbar}{2m_0} \lim_{\mathbf{r}' \to \mathbf{r}} (\nabla^2_{\mathbf{r}'} - \nabla^2_{\mathbf{r}})G^<(\mathbf{r}, t; \mathbf{r}', t) \\ &= \frac{e\hbar}{2m_0} \lim_{\mathbf{r}' \to \mathbf{r}} (\nabla_{\mathbf{r}'} + \nabla_{\mathbf{r}}) \cdot (\nabla_{\mathbf{r}'} - \nabla_{\mathbf{r}})G^<(\mathbf{r}, t; \mathbf{r}', t) \\ &= \frac{e\hbar}{2m_0} \nabla_{\mathbf{r}} \cdot \lim_{\mathbf{r}' \to \mathbf{r}} (\nabla_{\mathbf{r}'} - \nabla_{\mathbf{r}})G^<(\mathbf{r}, t; \mathbf{r}', t). \end{aligned} \tag{3.71}$$

By identification, we can define the current density vector as

$$\vec{J} = \frac{e\hbar}{2m_0} \lim_{\mathbf{r}' \to \mathbf{r}} (\nabla_{\mathbf{r}'} - \nabla_{\mathbf{r}}) G^{<}(\mathbf{r}, t; \mathbf{r}', t). \tag{3.72}$$

In practice, to evaluate $\vec{J}$ the lesser Green's function is expanded in a local basis, and the ∇-operator and m_0 are replaced by appropriate matrix elements $h_{m,n}$. In the next Chapter, the current density is given in a finite difference discretized grid with effective mass Hamiltonian, see Sec.4.1.2.

Noticing that at steady-state the time derivative of the charge density is zero. This implies that the $\nabla_{\mathbf{r}} \cdot \vec{J} = 0$ and the stationary current should be conserved in the device. In the presence of elastic scattering alone, the current density is conserved for electron at any given energy. With the inelastic scattering, the total current (integrated over energy) should be conserved.

3.4 Self-energies

The self-energies allow us to easily account for the effects of many-body interaction and perturbation. In this Section, the Hamiltonian operators and then the self-energies are given for different interactions [132].

3.4.1 Electron-electron interaction

We recall the Hamiltonian operator for electron-electron interaction

$$\hat{V} = \frac{1}{2} \int \mathrm{d}\mathbf{r}\mathrm{d}\mathbf{r}' \hat{\psi}^{\dagger}(\mathbf{r}) \hat{\psi}^{\dagger}(\mathbf{r}') V(\mathbf{r} - \mathbf{r}') \hat{\psi}(\mathbf{r}') \hat{\psi}(\mathbf{r}). \tag{3.73}$$

This Hamiltonian operator leads to an infinite hierarchy of self-energies. The first order approximation contains Hartree and Fock contributions. The Hartree self-energy is expressed as

$$\Sigma^{\text{Hartree}}(\mathbf{r}_1, t_1) = -\mathrm{i}\hbar \int \mathrm{d}t_3 \int \mathrm{d}\mathbf{r}_3 \delta(t_1 - t_3) V(\mathbf{r}_1 - \mathbf{r}_3) G(\mathbf{r}_3, t_3; \mathbf{r}_3, t_3). \tag{3.74}$$

with only one time variable t_1, because the Hartree self-energy is instantaneous. It can be proven that the Hartree self-energy is nothing else than the solution of the

Poisson's equation

$$\begin{aligned}\Sigma^{\text{Hartree}}(\mathbf{r}_1, t_1) &= \int \mathrm{d}\mathbf{r}_3 V(\mathbf{r}_1 - \mathbf{r}_3) n(\mathbf{r}_3, t_1) \\ &= \int \mathrm{d}\mathbf{r}_3 \frac{e^2}{4\pi\epsilon|\mathbf{r}_1 - \mathbf{r}_3|} \frac{\rho(\mathbf{r}_3, t_1)}{-e} \\ &= -e\varphi(\mathbf{r}_1).\end{aligned} \tag{3.75}$$

The potential φ is the solution of the Poisson's equation, as

$$\nabla_{\mathbf{r}} \cdot [\epsilon(\mathbf{r}) \nabla_{\mathbf{r}} \varphi(\mathbf{r})] + \rho(\mathbf{r}) = 0, \tag{3.76}$$

with the charge density ρ, and the dielectric constant ϵ. Since the potential depends on the charge density, which is given by the lesser $G^<$ Green's function, the exact Green's function G both determines and is determined by the self-energy. The coupling between Green's function and the Poisson's equation needs to be solved self-consistently.

3.4.2 Electron-phonon interactions

We start from the unperturbed Hamiltonian of phonons, which is equivalent to a collection of quantum harmonic oscillators

$$H^0_{\mathbf{q}} = \sum_{\mathbf{q}} \omega_{\mathbf{q}} (\hat{a_{\mathbf{q}}}^{\dagger} \hat{a_{\mathbf{q}}} + 1/2), \tag{3.77}$$

where $\hat{a_{\mathbf{q}}}^{\dagger}$ and $\hat{a_{\mathbf{q}}}$ are respectively the boson creation and annihilation operators, and $\mathbf{q}$ is the phonon momentum for a given branch index. The electron-phonon interaction Hamiltonian $V^{e-ph}_{\mathbf{q}}$ is expressed as

$$V^{e-ph}_{\mathbf{q}} = \sum_{\boldsymbol{k}} M_{\mathbf{q}} \hat{c}^{\dagger}_{\boldsymbol{k}+\mathbf{q}} \hat{c}_{\boldsymbol{k}} (\hat{a}_{\mathbf{q}} + \hat{a}^{\dagger}_{-\mathbf{q}}), \tag{3.78}$$

where $\hat{c}$ and $\hat{c}^{\dagger}$ are the usual annihilation and creation operators for fermions with given momentum, and $M_{\mathbf{q}}$ is the deformation matrix element that accounts for the strength of the interaction between electrons and phonons The values of $M_{\mathbf{q}}$ are usually taken from first-principle calculations. Using Wick's theorem and the Feynman diagrams, the first order self-energy for electron-phonon interactions is obtained as

$$\Sigma_{e-ph}(\mathbf{r}_1, t_1; \mathbf{r}_2, t_2) = \mathrm{i} \sum_{\mathbf{q}} e^{\mathrm{i}\mathbf{q}\cdot(\mathbf{r}_1 - \mathbf{r}_2)} |M_{\mathbf{q}}|^2 D^0_{\mathbf{q}}(t_1, t_2) G^0(\mathbf{r}_1, t_1; \mathbf{r}_2, t_2), \tag{3.79}$$

with $D^0_{\mathbf{q}}$ the unperturbed phonon Green's function [132]. Electron-phonon self-energy is usually evaluated within the self-consistent Born approximation (SCBA), which replaces the unperturbed Green's function G^0 of the first order approximation

by the full Green's function G. We thus obtain a self-consistent relation between the Green's function and the self-energy that must be accurately solved to ensure current conservation.

3.5 Summary

This Chapter contains a theoretical framework of the present thesis. We reviewed the NEGF formalism and derived the quantum kinetic equations starting from a general Hamiltonian in the second quantization presentation. The equations of motion for the contour-ordered Green's function was presented, then the retarded, the advanced, and the lesser Green's functions were obtained. Since the full Green's function in the time domain is extremely time consuming to compute, we simulate a stationary system and thus transform the Green's function into the energy domain. The relation between the Green's function and the self-energy is given through the Dyson equation. We also derived the self-energy for the electron-phonon interactions. The procedure to calculate observables from the Green's function were introduced.

Chapter 4

Implementation of Quantum Transport Model

In the previous Chapter, I introduced the quantum kinetic equations and the NEGF formalism for a general quantum system is described. Solving the Green's functions (3.55-3.58) is computationally very expensive due to the required inversion and multiplication of matrices as large as the Hamiltonian operator of the whole system. In addition, the SCBA cycle, which is important for the current conservation, needs many iterations before reaching the convergence. The complexity of the NEGF formalism increases rapidly with the size of simulated system.

In this Chapter, first a layered structure representation is introduced for the system under study, which transforms the original 3-D quantum kinetic equations to coupled quasi-1D equations. Then, I include the effects of the semi-infinite source and drain leads by introducing self-energy functions, which enables us to consider only the device region with the open-boundary condition. Then I present an adaptive algorithm to integrate the Green's functions to calculate the observables such as the charge and the current distributions. Finally, I explain the iteration between the Poisson and the transport equations to obtain the self-consistent solution and give an outline of the main code structure used in the simulations.

The implementation of optimized numerical codes needed for simulations is a considerable and important part of the present thesis. The programs are written in Fortran90 language and run on a multi-processor server with Linux. The Intel Fortran compiler and the MKL libraries for linear algebra have been adopted. The graphic visualization of the results has been obtained with the Gnuplot, with the scripts both for the homogeneity of the figures and for efficiency purpose. From the output of the code for the evaluation of space and energy-resolved currents and other physical quantities, it is possible to obtain colormaps of their distributions.

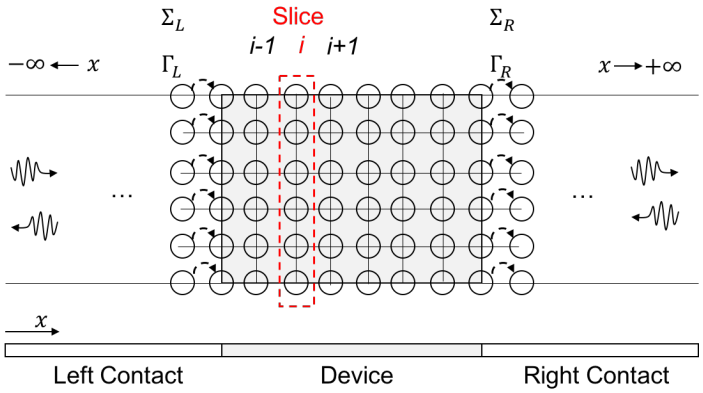

FIGURE 4.1: Schematic cross-section of a system in the simulation, which has a layered structure. Layer i only interacts with its left and right neighbors i-1 and i+1.

4.1 NEGF for layered structures

The typical devices that we simulate extend between source and drain contacts at the extremities of the channel. By using a finite difference discretization, the system can be divided into consecutive layers that are coupled to the nearest neighbor sections only. As shown in Fig.4.1, each layer with index i interacts only with itself and its nearest neighbor layers with indices $i-1$ and $i+1$. The idea is to express the Hamiltonian in a basis of states localized in each layer. The Hamiltonian in this basis turns out to be a block tridiagonal matrix, where the diagonal blocks H_i represent the Hamiltonian of the layer i and off-diagonal blocks T_i represent coupling between neighbor layers i and $i+1$:

$$\mathbf{H} = \begin{pmatrix} H_1 & T_1 & & & & & & \\ T_1^\dagger & H_2 & T_2 & & & & & \\ & T_2^\dagger & H_3 & T_3 & & & & \\ & & \cdot & \cdot & \cdot & & & \\ & & & \cdot & \cdot & \cdot & & \\ & & & & \cdot & \cdot & T_{i-1} & \\ & & & & & T_{i-1}^\dagger & H_i & \cdots \\ & & & & & & \cdots & \cdots \end{pmatrix}. \tag{4.1}$$

As we reviewed in the previous Chapter, in general, the retarded Green's function equation for the whole system in the presence of electron-phonon scattering, under the steady-state, represented in the matrix form is

$$[E\mathbf{I} - \mathbf{H} - \mathbf{\Sigma}_{\text{ph}}^R]\mathbf{G}^{\mathbf{R}} = \mathbf{I}, \tag{4.2}$$

where, $\mathbf{\Sigma}^R_{\text{ph}}$ is the retarded self-energy due to electron-phonon scattering, which is discussed in Sec.3.4.2. The lesser Green's function equation in the matrix form is

$$\mathbf{G}^< = \mathbf{G}^\mathbf{R}\mathbf{\Sigma}^<_{\text{ph}}\mathbf{G}^{\mathbf{R}\dagger}, \tag{4.3}$$

where, $\mathbf{\Sigma}^<_{\text{ph}}$ is the lesser self-energy matrix due to electron-phonon scattering, which is defined using the relation (3.46).

4.1.1 Semi-infinite leads

We partition the layered structure into left contact, device and right contact as shown in Fig.4.1. We do not need to solve the Green's function for the entire structure because of the macroscopic size of the contacts and the outside circuit. Moreover, once an electron is collected at the outside circuit, its subsequent dynamics is practically impossible to follow, and this electron is "lost" into the outside circuit, most likely without changing the internal state of the latter. The outside circuit contacts effectively act as electron reservoirs with a stable Fermi energy. For these reasons, we are dealing with open boundary condition on the left and right contacts.

The device corresponds to the region of interest where we solve for the NEGF equations. However, this partition is, to some extent, arbitrary. For instance, it could be advantageous to include part of the contacts into the central device region, or to include only a limited portion of the device into the central region.

The Green's function of the device region is determined by the Dyson equation

$$\mathbf{G}^{\mathbf{R},\mathbf{A}} = \mathbf{g}^{\mathbf{R},\mathbf{A}} + \mathbf{g}^{\mathbf{R},\mathbf{A}}\mathbf{T}\mathbf{G}^{\mathbf{R},\mathbf{A}}, \tag{4.4}$$

with $\mathbf{G}^{\mathbf{R},\mathbf{A}}$ the retarded/advanced Green's function for the full system, the $\mathbf{g}^{\mathbf{R},\mathbf{A}}$ the retarded/advanced Green's function for the disconnected system and $\mathbf{T}$ the coupling matrix.

Then we introduce some useful quantities. The retarded and the advanced self-energy of the left(right) contact $\mathbf{\Sigma}^{\mathbf{R},\mathbf{A}}_{\mathbf{L},\mathbf{R}}$, the lesser and the greater self-energy of the contacts $\mathbf{\Sigma}^{\lessgtr}_{\mathbf{L},\mathbf{R}}$, and the rate operator $\mathbf{\Gamma}_{\mathbf{L},\mathbf{R}}$. Here we are interested in the central device region, therefore these operators are projected onto the Hilbert subspace corresponding to the central part. Because of the layered structure, only the interface layers are connected together. We have the following equations

$$\mathbf{\Sigma}^{\mathbf{R},\mathbf{A}}_{\mathbf{L},\mathbf{R}} = \mathbf{T}_{\mathbf{L},\mathbf{R}}\, \mathbf{g}^{\mathbf{R},\mathbf{A}}_{\mathbf{L},\mathbf{R}}\, \mathbf{T}^\dagger_{\mathbf{L},\mathbf{R}}; \tag{4.5}$$

$$\mathbf{\Sigma}^{\lessgtr}_{\mathbf{L},\mathbf{R}} = \mathbf{T}_{\mathbf{L},\mathbf{R}}\, \mathbf{g}^{\lessgtr}_{\mathbf{L},\mathbf{R}}\, \mathbf{T}^\dagger_{\mathbf{L},\mathbf{R}}; \tag{4.6}$$

$$\mathbf{\Gamma}_{\mathbf{L},\mathbf{R}} = \mathrm{i}(\mathbf{\Sigma}^{\mathbf{R}}_{\mathbf{L},\mathbf{R}} - \mathbf{\Sigma}^{\mathbf{A}}_{\mathbf{L},\mathbf{R}}), \tag{4.7}$$

where $\mathbf{T}_{\mathbf{L},\mathbf{R}}$ is the coupling matrix between the surface layer of the left(right) contact with the device, $\mathbf{g}^{\mathbf{R},\mathbf{A},\lessgtr}_{\mathbf{L},\mathbf{R}}$ is the surface Green's functions of the left(right) contact.

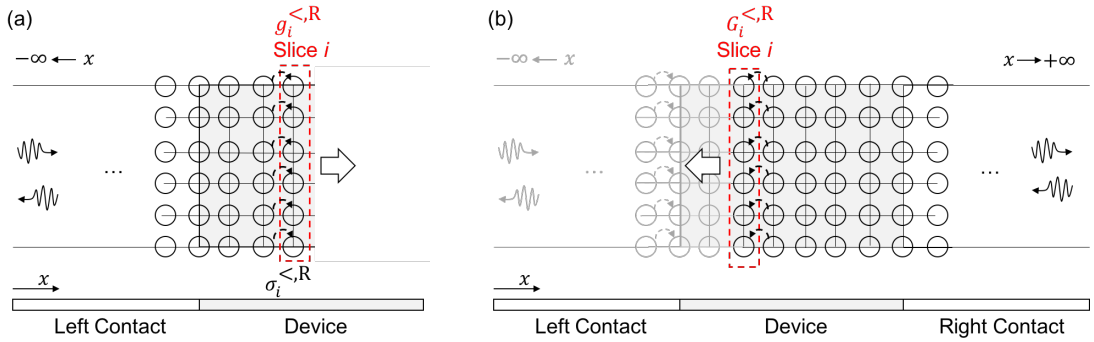

FIGURE 4.2: Illustration of the recursive algorithm for the Green's function in the device region. (a) Starting from the left, we couple layer by layer with the perturbation from the left neighbor layer and compute the left-connected Green's functions. (b) When arriving at the right end of the device region, we couple the right lead onto the last layer. Then we couple layer by layer with the perturbation from the right neighbor layer until arriving at the left end of the device region and obtain the full Green's function on each slice.

We can rewrite Eq.(4.2) as

$$[E\mathbf{I_D} - \mathbf{H_D} - \mathbf{\Sigma}^{\mathbf{R,A}}_{\mathbf{D,ph}} - \mathbf{\Sigma}^{\mathbf{R,A}}_{\mathbf{L}} - \mathbf{\Sigma}^{\mathbf{R,A}}_{\mathbf{R}}]\,\mathbf{G}^{\mathbf{R,A}}_{\mathbf{D}} = \mathbf{I_D}, \tag{4.8}$$

where $\mathbf{\Sigma}^{\mathbf{R}}_{\mathbf{L}}$ and $\mathbf{\Sigma}^{\mathbf{R}}_{\mathbf{R}}$ are the retarded self-energies of the left and the right contact given by the previous equation, the subscript $_{\mathbf{D}}$ shows that the equation is projected onto the device region. For the lesser and the greater Green's function, the NEGF formalism gives the following equations

$$\mathbf{G}^{\lessgtr}_{\mathbf{D}} = \mathbf{G}^{\mathbf{R}}_{\mathbf{D}}\,[\mathbf{\Sigma}^{\lessgtr}_{\mathbf{D,ph}} + \mathbf{\Sigma}^{\lessgtr}_{\mathbf{L}} + \mathbf{\Sigma}^{\lessgtr}_{\mathbf{R}}]\,\mathbf{G}^{\mathbf{A}}_{\mathbf{D}}, \tag{4.9}$$

where $\mathbf{\Sigma}^{\lessgtr}_{\mathbf{D,ph}}$ are the lesser and the greater self-energy of electron-phonon scattering, $\mathbf{\Sigma}^{\lessgtr}_{\mathbf{L}}$ and $\mathbf{\Sigma}^{\lessgtr}_{\mathbf{R}}$ are the lesser and the greater self-energies of the contacts defined previously.

4.1.2 Recursive algorithm for device region

In order to properly describe the system electrostatics, we make use of the Poisson equation (Eq.3.76), whose input is the spatial charge density. This last is obtained by integrating over energy the diagonal elements $\mathbf{G}^{<}_{\mathbf{i,i}}(E)$ of the lesser Green's function, where the index i runs over the points of the device. For the current density, one requires the diagonal and the off-diagonal blocks of the lesser Green's function. Therefore, we do not require to calculate the Green functions on the whole space in order to obtain the quantities that we need for transport simulations. Indeed, we only need the Green's function on the diagonal and off-diagonal blocks. Therefore, it is desirable to reduce the numerical burden by exploiting the layered structure of the device and to only compute the diagonal and off-diagonal blocks of the retarded

and lesser Green's function. In this section, an algorithm that is valid for the block tridiagonal form of matrices is presented [133, 134].

To start, we first compute the left-connected Green's functions for each layers in the device region, which is noted by lowercase $\mathbf{g_i^R}$ and $\mathbf{g_i^<}$, where the index i refers to the layer index. This step is shown in Fig.4.2(a). By using the Dyson equation again, we obtain

$$[E\mathbf{I_i} - \mathbf{H_i} - \mathbf{\Sigma^R_{i,ph}} - \sigma_\mathbf{i}^\mathbf{R}]\ \mathbf{g_i^R} = \mathbf{I_i}, \tag{4.10}$$

where $\sigma_\mathbf{i}^\mathbf{R} = \mathbf{T_i} \mathbf{g}_{\mathbf{i-1}}^\mathbf{R} \mathbf{T}_\mathbf{i}^\dagger$ is the retarded self-energy from the left-connected part. Similarly, for the lesser Green's function, we can obtain

$$\mathbf{g_i^<} = \mathbf{g_i^R}\ [\mathbf{\Sigma^<_{i,ph}} + \sigma_\mathbf{i}^<]\ \mathbf{g_i^{R\dagger}}, \tag{4.11}$$

with $\sigma_\mathbf{i}^< = \mathbf{T_i}\ \mathbf{g_{i-1}^<}\ \mathbf{T}_\mathbf{i}^\dagger$ the lesser self-energy from the left-connected part. By successively applying the above two equations, the central device region is connected onto the left contact layer by layer. For the right-most layer with index N, it is connected at the same time to the rest of the device and the right contact, therefore we obtain its full Green's functions

$$[E\mathbf{I_N} - \mathbf{H_N} - \mathbf{\Sigma^R_{N,ph}} - \mathbf{T_N}\ \mathbf{g^<_{N-1}}\ \mathbf{T}_\mathbf{N}^\dagger - \mathbf{\Sigma^R_R}]\ \mathbf{G^R_N} = \mathbf{I_N}, \tag{4.12}$$

$$\mathbf{G^<_N} = \mathbf{G^R_N}\ [\mathbf{\Sigma^<_{N,ph}} + \mathbf{T_N}\ \mathbf{g^<_{N-1}}\ \mathbf{T}_\mathbf{N}^\dagger + \mathbf{\Sigma^<_R}]\ \mathbf{G_N^{R\dagger}}, \tag{4.13}$$

where $\mathbf{\Sigma^<_R}$ and $\mathbf{\Sigma^R_R}$ are the lesser and the retarded self-energies of the right contact.

At this stage, we can compute the full Green's functions, as shown in Fig.4.2(b). In order to do this, we apply again the Dyson equation and obtain the following relations

$$\mathbf{G_i^R} = \mathbf{g_i^R} + \mathbf{g_i^R}\ \mathbf{T_{i+1}}^\dagger\ \mathbf{G^R_{i+1}}\ \mathbf{T_{i+1}}\ \mathbf{g_i^R}, \tag{4.14}$$

$$\begin{aligned}\mathbf{G_i^<} =& \mathbf{g_i^<} + \mathbf{g_i^<}\ \mathbf{T_{i+1}}^\dagger\ \mathbf{G^R_{i+1}}^\dagger\ \mathbf{T_{i+1}}\ \mathbf{g_i^{R\dagger}} + \mathbf{g_i^R}\ \mathbf{T_{i+1}}^\dagger\ \mathbf{G^<_{i+1}}\ \mathbf{T_{i+1}}\ \mathbf{g_i^{R\dagger}} + \\ & \mathbf{g_i^R}\ \mathbf{T_{i+1}}^\dagger\ \mathbf{G^R_{i+1}}\ \mathbf{T_{i+1}}\ \mathbf{g_i^<},\end{aligned} \tag{4.15}$$

and

$$\mathbf{G^<_{i+1,i}} = \mathbf{G^R_{i+1}}\ \mathbf{T_{i+1}}\ \mathbf{g_i^<} + \mathbf{G^<_{i+1}}\ \mathbf{T_{i+1}}\ \mathbf{g_i^{R\dagger}}, \tag{4.16}$$

where $\mathbf{G_i^<}$ denotes a diagonal block and $\mathbf{G^<_{i+1,i}}$ denotes an off-diagonal block of the full lesser Green's function of the device region, which is useful for calculating the current density $\mathbf{J_{i,i+1}}$ between the neighbor layers with indexes i and $i+1$ using the following formula [134]

$$\mathbf{J_{i,i+1}} = \frac{e}{h}\int \mathrm{d}E\ \mathrm{Tr}\Big[\mathbf{T}_\mathbf{i+1}^\dagger\ \mathbf{G^<_{i+1,i}}(E) - \mathbf{T_{i+1}}\mathbf{G^<_{i,i+1}}(E)\Big]. \tag{4.17}$$

4.1.3 Phonon self-energies

In Eq.(4.10) and (4.11) the phonon self-energies are required. We compute them within the SCBA as described in Sec.3.4.2. To investigate realistic nanodevice structures, some simplifications and approximations have to be considered in the calculation of the phonon self-energies. We use the deformation potential interaction to describe how electrons interact with the local changes in the crystal potential associated with a lattice vibration. Within the deformation potential approximation, the electron-phonon coupling is local in space. For scattering on acoustic phonons, the coupling matrix element is linear in $\mathbf{q}$ in the long-wavelength limit,

$$M_{\mathbf{q}} = D_{ac} q, \tag{4.18}$$

where D_{ac} is the acoustic deformation potential. The acoustic phonon lesser and greater self-energy at the layer i of the device along the transport direction is expressed as

$$\mathbf{\Sigma}^{\lessgtr}_{\mathbf{i,ac}}(n,n;E) = \frac{D_{ac}^2 k_B T}{\rho v_s^2} \mathbf{G}^{\lessgtr}_{\mathbf{i}}(n,n;E), \tag{4.19}$$

where $\mathbf{G}^{\lessgtr}_{\mathbf{i}}(n,n;E)$ is the nth diagonal entry of the ith diagonal block of lesser or greater Green's function, ρ is the mass density, and v_s is the sound velocity [135].

In the case of optical phonon scattering, the interaction *via* the constant zero-order optical deformation potential D_{op} is given by

$$M_{\mathbf{q}} = D_{op}. \tag{4.20}$$

The optical phonon lesser and greater self-energies read

$$\mathbf{\Sigma}^{\lessgtr}_{\mathbf{i,op}}(n,n;E) = \frac{\hbar D_{op}^2}{2\rho\omega}[N\mathbf{G}^{\lessgtr}_{\mathbf{i}}(n,n;E \mp \hbar\omega) + (N+1)\mathbf{G}^{\lessgtr}_{\mathbf{i}}(n,n;E \pm \hbar\omega)], \tag{4.21}$$

where ω is the frequency of the optical branch considered in the simulation, and N is the equilibrium phonon density according to the Bose statistics.

The total phonon self-energy is the sum of that of the acoustic and optical phonon branches

$$\mathbf{\Sigma}^{\lessgtr}_{\mathbf{i,ph}} = \mathbf{\Sigma}^{\lessgtr}_{\mathbf{i,ac}} + \mathbf{\Sigma}^{\lessgtr}_{\mathbf{i,op}}. \tag{4.22}$$

The retarded self-energy $\mathbf{\Sigma}^{\mathbf{R}}_{\mathbf{i,ph}}$ is composed of two parts,

$$\mathbf{\Sigma}^{\mathbf{R}}_{\mathbf{i,ph}}(E) = \frac{1}{2}[\mathbf{\Sigma}^{>}_{\mathbf{i,ph}}(E) - \mathbf{\Sigma}^{<}_{\mathbf{i,ph}}(E)] + \underbrace{\mathrm{i}\mathcal{P}\int \frac{\mathrm{d}E'}{2\pi} \frac{\mathbf{\Sigma}^{>}_{\mathbf{i,ph}}(E') - \mathbf{\Sigma}^{<}_{\mathbf{i,ph}}(E')}{E - E'}}_{\text{neglected}}. \tag{4.23}$$

The second term requires the evaluation of a Cauchy principal integral coupling all the energies together. For computational reasons, this integral term is neglected in

this thesis. Previous studies have shown that this simplification does not introduce significant errors in the calculation of the device current [136, 137].

4.2 Adaptive energy integration

In order to obtain the physical quantities of interest, such as the charge and the current, numerical integration over energy is required. Proper numerical integration methods are essential for the stability and accuracy of the NEGF calculations. The numerical evaluation of these integrals requires a discretization of the energy domain. One approach is using a fixed energy grid that can be either equidistant or based on Gauss–Legendre quadrature. The Gaussian quadrature is typically more accurate if the integrand is smooth. If some narrow resonances are present in the nano-device density of states, a small number of energy grid points will not correctly resolve the Green's function, whereas a vast number can lead to intractable memory and time requirements. These effects can yield instability or poor convergence of the self-consistent Schrödinger-Poisson iteration loop. Therefore, an adaptive energy integration on a non-equidistant energy mesh is useful to increase accuracy, numerical stability, and memory efficiency. In this section, I outline the adaptive energy integration that was implemented and tested within the NEGF formalism. For the electron-phonon interactions, only the elastic scattering is included into this adaptive method, because the inelastic phonon can scatter the electrons from energy E_1 into E_2, thus making the adaptive integration extremely problematic.

This method based on the adaptive Simpson's rule was first proposed by G.F. Kuncir in 1962 [138]. The algorithm uses an estimate of the error we get from calculating the integral. If the error exceeds a predefined tolerance, the algorithm calls for subdividing the interval of integration in two and applying the same method to each subinterval in a recursive manner.

The integral of a function $f(x)$ over an interval $[a, b]$ is given by

$$S(a,b) = \frac{b-a}{6}\left[f(a) + 4f(c) + f(b)\right], \tag{4.24}$$

where $[a, b]$ is the interval to integrate, $S(a, b)$ is the estimates given by Simpson's rule on the corresponding intervals, and c is the midpoint of $[a, b]$. One strategy to decrease the interpolation error is to subdivide the interval into two equal parts and to apply Simpson's rule on each subinterval. This leads to the composite Simpson rule which, for five grid points, writes as

$$S(a,c) + S(c,b) = \frac{b-a}{12}\left[f(a) + 4f\left(\frac{a+c}{2}\right) + 2f(c) + 4f\left(\frac{c+b}{2}\right) + f(b)\right], \tag{4.25}$$

where $S(a, c)$ and $S(c, b)$ are the estimates given by Simpson's rule on the corresponding subintervals.

A criterion for determining when to stop subdividing an interval, suggested by J.N. Lyness [139] is

$$|S(a,c) + S(c,b) - S(a,b)|/15 \leq \epsilon, \tag{4.26}$$

where ϵ is the desired tolerance for the interval. If this condition is satisfied, the integral is considered accurate enough and the energy mesh in the given interval is not further refined.

Using Richardson extrapolation [140], the more accurate Simpson estimate $[S(a,c)+S(c,b)]$ is combined with the less accurate estimate $S(a,b)$ by the formula

$$[16 \times S(a,c) + 16 \times S(c,b) - S(a,b)]/15. \tag{4.27}$$

The obtained estimate is exact for polynomials of degree five or less, which is more accurate than the simple and composite Simpson's rule.

Now we will look more into detail to obtain the criterion (4.26) and to justify the the statement about exactness for the polynomials of degree less than 5. Indeed, since the Simpson's rule is actually obtained from the trapezoidal rule by one step of Richardson extrapolation, it has error expansion of the form

$$S(a,b) = \int_a^b \mathrm{d}x f(x) + \alpha_4 h^4 + \alpha_6 h^6 + ... \tag{4.28}$$

where $h = |b-a|$ is the size of interval. This shows that Simpson's rule provides exact results for any polynomial f of degree three or less. Making the step twice as small we get

$$S(a,c) + S(c,b) = \int_a^b \mathrm{d}x f(x) + \alpha_4 h^4/16 + \alpha_6 h^6/64 + ... \tag{4.29}$$

Multiplying Eq. (4.29) by 16 and subtracting Eq. (4.29) from it we obtain

$$16 \times S(a,c) + 16 \times S(c,b) - S(a,b) = 15 \int_a^b \mathrm{d}x f(x) + \alpha_6' h^6 + ... \tag{4.30}$$

Therefore

$$S(a,c) + S(c,b) + [S(a,c) + S(c,b) - S(a,b)]/15 = \int_a^b \mathrm{d}x f(x) + \beta_6 h^6 + ... \tag{4.31}$$

Comparing Eqs.(4.29) and (4.31), we see that the error in Eq.(4.29) is dominated by $[S(a,c) + S(c,b) - S(a,b)]/15$. Therefore, the stopping criterion Eq.(4.26) and the combining formula Eq.(4.27) are justified.

The implemented energy integration algorithm was applied to a van der Waals TFET structure based on MoS_2 and WTe_2 monolayers. The device structure is described in Chapter 6 with a sketch of the device in Fig.6.1. The colormap in Fig.4.3 shows a large concentration of the density-of-occupied-states in the overlap region

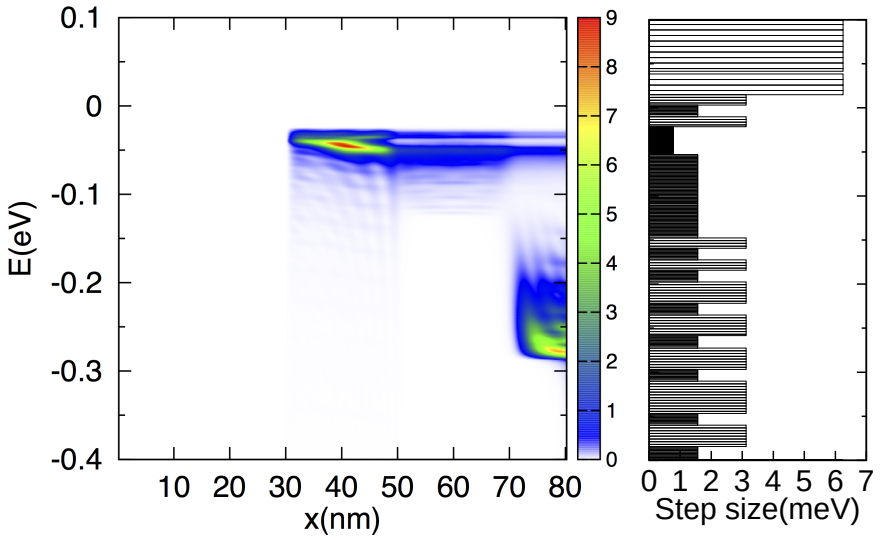

FIGURE 4.3: Example of adaptive Simpson's rule for energy integral. (colormap) Local density-of-occupied-states on the top MoS_2 monolayer (see Fig.6.1) for V_{TG}=0.1 V and V_{DS}=0.3 V. (bar chart) Energy step size vesus energy corresponding to the left colormap. The lowest energy step corresponds to a resonance.

on the top MoS_2 monolayer. The histogram on the right shows the distribution of the step size between two grid points versus energy. The decrease of step size at the maximum of density and the contact chemical potential can be well distinguished. At these energies, more grid points are placed by the algorithm.

This first attempt with adaptive Simpson's rule is functional and significantly increases the stability of the transport simulations. A more general approach with non-equidistant grid points and polynomials of arbitrary degree can be considered. Other more modern adaptive methods based on Gauss–Kronrod quadrature [141] and Clenshaw–Curtis quadrature [142] can also be considered to further increase the numerical accuracy of the simulator.

4.3 Structure of the codes

Since object-oriented programming is not directly supported by Fortran90, we need to carefully organize the codes into separate modules in order to ensure their readability and reusability. The programs developed are divided into modules, each with a specific well-defined task to accomplish. The source codes of each module are contained in an individual file. Each module contains both the data structure definitions and the subroutines to achieve its task. For instance, the "Green" module that solves the NEGF equations, contains the definition of the data structure for storing the retarded, the lesser and the greater Green's functions, together with the subroutines to solve the equation and the subroutines to extract observables, as

charge and current densities. A clear definition of the interfaces and the boundaries of the modules are important to create independent and interchangeable codes.

The algorithmic flow in modeling nanodevices using the NEGF consists of the following steps (Fig.4.4). We first find a guess for the electrostatic potential $\phi(\mathbf{r})$ and calculate the self-energies due to the contacts. The self-energies due to electron-phonon scattering are set to zero. The NEGF equations for $\mathbf{G}^{\mathbf{R}}$ and $\mathbf{G}^{\lessgtr}$ (Section 4.1.2) are then solved. Following this, the self-energies due to electron-phonon scattering and contacts are calculated. As the equations governing the Green's functions depend on the self-energies, we iteratively solve for the Green's function and self-energies, as indicated by the inner loop of Fig.4.4. Then, the electron density calculated from $\mathbf{G}^{<}$ is used in Poisson's equation to obtain a new potential profile $\phi(\mathbf{r})$. We use this updated electrostatic potential profile as an input to solve for updated NEGF, and continue the above process iteratively until convergence is achieved.

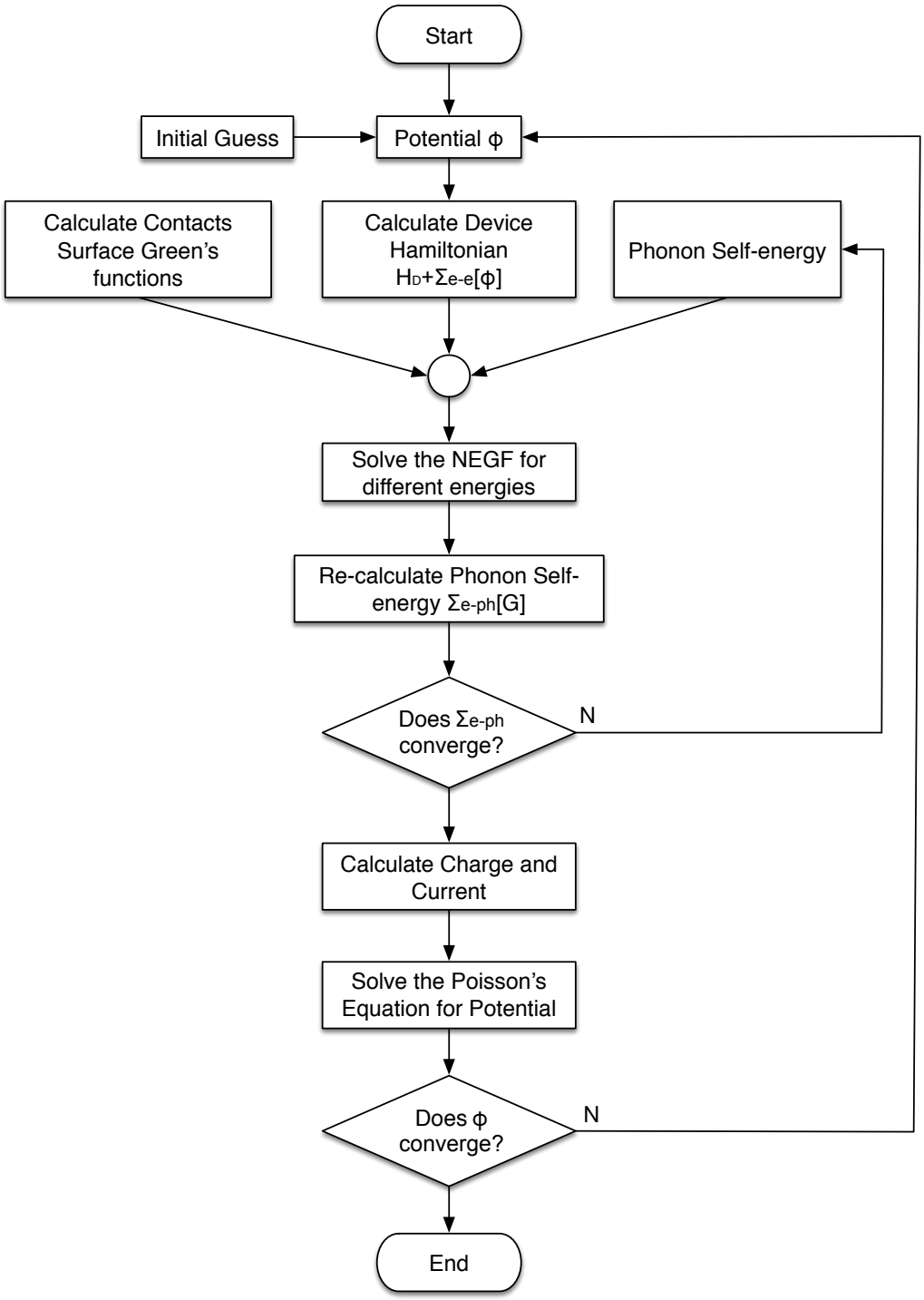

FIGURE 4.4: Flowchart of a typical simulation involved in modeling electronic transport of a nano-device.

Chapter 5

Vertical Tunnel-FETs based on 2-D materials

The TFET may enable a more aggressive V_{DD} scaling than the MOSFETs and allow for ultra-low-power applications, by lowering the sub-threshold swing (SS) under the thermionic limit of 60mV/dec at room temperature. As shown in Chapter 2, the use of monolayers of Transition Metal Dichalcogenides (TMDs), such as MoS_2 and WTe_2, may represent an extremely advantageous alternative for their intrinsic 2-D nature and sub 1 nm thinness, the absence of dangling bonds, as well as the variety of available materials, which results in a large range of energy band gaps and band alignments. Some vertical TFETs based on 2-D TMDs have been recently proposed in [17, 20, 26, 28, 143].

In this Chapter, the IV-characteristics at room temperature of a 2-D TMD-based vertical TFET are simulated based on an Effective Mass Approximation (EMA) Hamiltonian and the NEGF formalism presented in Chapter 3 and 4. The model self-consistently accounts for the device electrostatics and the electron-phonon scattering. In particular, Sec.5.1 defines the device geometry under this study. In Sec.5.2, the electronic intra- and inter-layer transport is calibrated to be coherent to the available experimental data [96, 101]. Section 5.3 addresses several aspects related to the device design, including (a) chemical doping and back-gate potential; (b) top gate geometrical alignment; (c) current scaling with channel length. The influence of each of these parameters on the device performance is illustrated by plotting systematically the IV-characteristics and providing some physical interpretations by calculating the representative physical quantities such as the LDOS and the carrier density. Finally, two metrics are calculated for the delay and energy corresponding to the switching of a digital inverter based on this TFET. The results in this Chapter have been published in [144, 145].

5.1 Device description

The MoS_2/h-BN/WTe_2 vertical TFET studied in this work is sketched in Fig.5.1 and consists of a WTe_2 mono-layer on the bottom as the source, a MoS_2 mono-layer on

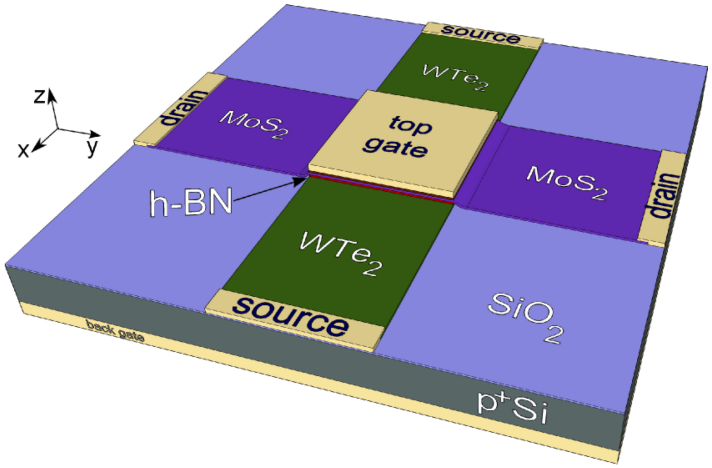

FIGURE 5.1: 3-D sketch of the MoS_2-WTe_2 TFET under study.

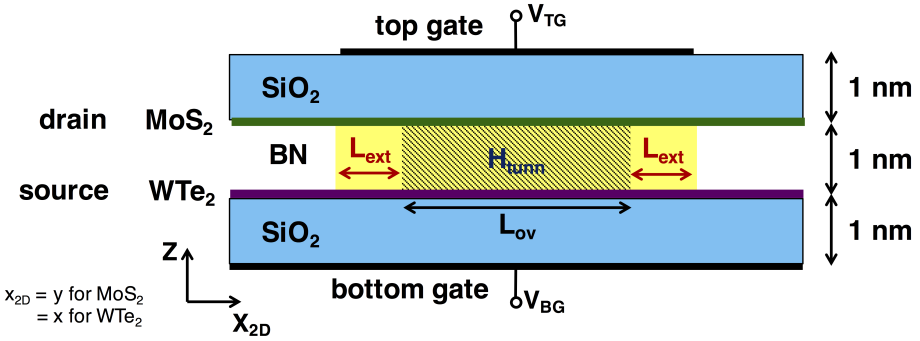

FIGURE 5.2: Sketch of the 2-D structure in our simulations, where x_{2D} corresponds to the y direction in MoS_2 and to x in WTe_2 layer, as defined in Fig.5.1. The top and back gate oxides have an EOT of 1 nm. No interlayer tunneling is possible outside the overlap region. The shadowed green region indicates the h-BN interlayer where the two layers are electrostatically coupled, which is larger than the overlap region L_{TG}>L_{OV}).

the top as the drain, and a 1 nm thick h-BN interlayer, which acts as a tunnel barrier. The channel is defined by the overlap region between the WTe_2 and MoS_2 layers. A bottom gate, with voltage V_{BG}, electrostatically controls the charge density in the WTe_2 layer. The top MoS_2 layer is chemically doped with a donor concentration N_D. The top gate, with voltage V_{TG}, exceeds the overlap region by an extension length L_{ext} on each side to suppress the leakage current in the off-state.

To simulate this device, the equivalent 2-D model sketched in Fig.5.2 is considered in order to decrease the computational burden. This model is obtained by virtually rotating the top layer by $\pi/2$ and by considering an inter-layer coupling only over an overlap length L_{OV} corresponding to the square overlap region. The new coordinate x_{2D} indicated in Fig.5.2 corresponds to x for the WTe_2 layer and to y for the MoS_2 layer. We consider the lateral extension of the layers is infinite, thus taking advantage of the simplified planar symmetry. The top gate length L_{TG} exceeds the overlap length L_{OV} by the extension length L_{ext}. The MoS_2 and the WTe_2 monolayers are

TABLE 5.1: Parameters used to simulate the 2-D layers.

Parameters	**units**	**MoS_2**	**WTe_2**
m_e/m_0		0.378	-
m_h/m_0		-	0.319
E_{gap}	eV	1.8	0.9
χ	eV	4.3	3.65

described by an effective mass Hamiltonian obtained by fitting the band structure calculated in Ref. [68] with the Density Functional Theory (DFT):

$$H(x) = \begin{pmatrix} H_t(x) & H_{tb}(x) \\ H_{bt}(x) & H_b(x) \end{pmatrix}, \tag{5.1}$$

where x stands for x_{2D} and the top and bottom intra-layer Hamiltonian elements H_t and H_b are given by

$$\begin{cases} H_t(x) = -\dfrac{\hbar^2\partial_x^2}{2m_t} - eU_t(x) - \chi_t \\ H_b(x) = \dfrac{\hbar^2\partial_x^2}{2m_b} - eU_b(x) - \chi_b - E_{gap} \end{cases} \tag{5.2}$$

with m_t the effective mass of the MoS_2 conduction band in the top layer, m_b the effective mass of the WTe_2 valence band in the bottom layer, U_t and U_b the electrostatic potentials on the two layers, which are obtained by self-consistently coupling the quantum transport equations with the Poisson equation, χ_t and χ_b the electron affinities, and E_{gap} the WTe_2 band gap. The corresponding parameters are reported in Tab.5.1.

The electronic inter-layer transport is an out-of-plane vertical tunneling process, which is quite weak and is expected to have modest influence on the electrostatics of this device. The coupling energy, H_{tb}=H_{bt}, is constant and equal to H_{tunn} in the overlap region, and zero elsewhere. Section 5.2 determines this parameter H_{tunn} and its influence on the simulation results.

An important remark here is that the equivalent 2-D model of Fig.5.2 is expected to be able to properly capture the physics of the actual 3-D device of Fig.5.1. While the electrostatics could differ in the two cases, all the other key features play exactly the same role. In particular, this is true for the length L_{ext} of the top gate exceeding the overlap region, which determines the *exponential* suppression of the current in the off-state, as it will be clear from the numerical simulations in the Sec.5.3.

The Keldysh-Green's function formalism presented previously in Chapter 3 is adopted to compute the electron transport in this device, with the inclusion of the scattering

with acoustic phonons by means of local self-energies. The charge density is injected into the non-linear Poisson solver to take into account the device electrostatics self-consistently.

5.2 Calibration of the model

Up to the present, few experimental data about electronic intra- and inter-layer transport are available for MoS_2 and WTe_2 monolayers. In this work, we have calibrated the phonon and interlayer coupling parameters of our model to make the simulations consistent with these experiments.

First, in order to calibrate the deformation potential of elastic acoustic phonons, we have simulated a monolayer MoS_2 MOSFET structure with the same geometry as in the experiments at room-temperature presented in [96]. The simulated effective mobility is extracted in the linear transport regime and given by the following equation

$$\mu_{\text{eff}} = \frac{G L_{\text{ch}}}{q N_{\text{2D}}} \tag{5.3}$$

where the G is the conductance, L_{ch} is the channel length, and N_{2D} is the channel electron density per unit surface. As discussed in [146], we restricted the density N_{2D} evaluation over a section characterized by an almost uniform electron distribution, which gives a more accurate evaluation of the effective mobility. Fig.5.3 shows the simulated phonon-limited mobility versus electron density, and compared to the experimental mobility from [96]. Assuming that the experimental mobility is dominated by acoustic phonons, with a deformation potential of acoustic phonon D_{ac}=15eV, the simulated mobility can track fairly well the experimental data. We adopted thus this value of D_{ac} throughout this chapter.

The inter-layer coupling energy H_{tunn}, see Fig.5.2, determines the probability for the electrons with energy inside the tunneling window to tunnel through the h-BN barrier. Here H_{tunn} is calibrated on the I_{ON} of the device. Fig.5.4 reports the source-drain current I_{DS} versus V_{TG} for the TFET with L_{OV}=20nm and different values of inter-layer coupling. For H_{tunn}=1meV, we obtain an $I_{\text{DS}}/L_{\text{OV}}$ in the same order of magnitude reported for the graphene/h-BN/graphene system in [101], which can be considered as a reasonable reference with a tunneling barrier height close to the MoS_2/h-BN/WTe_2 system considered in this work. In the rest of this chapter, H_{tunn} is always set to 1 meV. Figure 5.4 also verifies that the current I_{DS} in both on- and off-state is modulated by H_{tunn} and the SS is almost insensitive to this parameter, confirming the fact that the weak tunneling considered has indeed a modest influence on the electrostatics in the off-state.

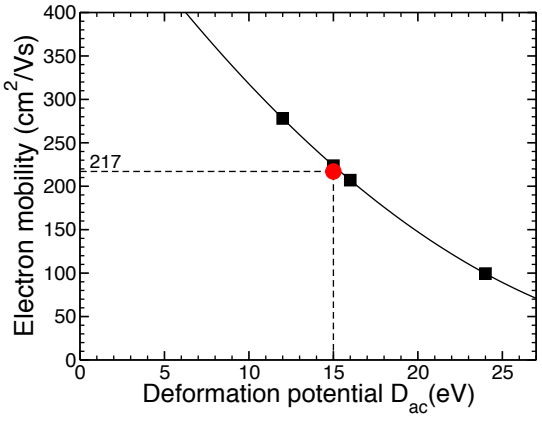

FIGURE 5.3: Simulated acoustic phonon limited mobility versus electron density in the MoS_2 MOSFET compared to experiments from [96] at room temperature. Results are shown for different values of the deformation potential D_{ac}.

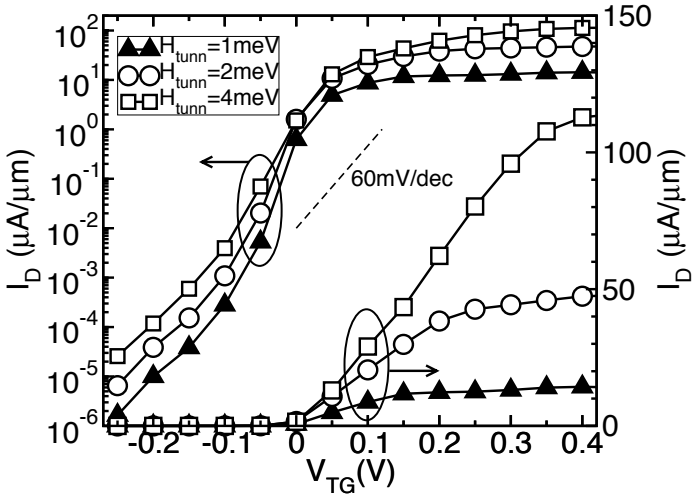

FIGURE 5.4: I_{DS} vs. V_{TG} curves at V_{DS}=0.3 V for the TFET sketched in Fig 5.2 with different values of the band-to-band tunneling coupling H_{tunn}.

5.3 Results and discussion

The working mechanism of the device is illustrated by Fig.5.5, which shows the inter-layer tunneling spectral current distribution along the x_{2D} direction in the off- and on-state, together with the profiles of the conduction band edge of the top MoS_2 layer (E_{CT}) and valence band edge of the bottom WTe_2 layer (E_{VB}). Note that outside the overlap region the states of the valence band are completely located in the bottom layer, and those of the conduction band in the top layer. In the overlap region, on the contrary, the states on the two layers are mixed due to the inter-layer coupling H_{tunn}, thus allowing electrons to pass from one layer to the other.

At low V_{TG}, the E_{CT} is higher than the E_{VB} in the region under the top gate, thus

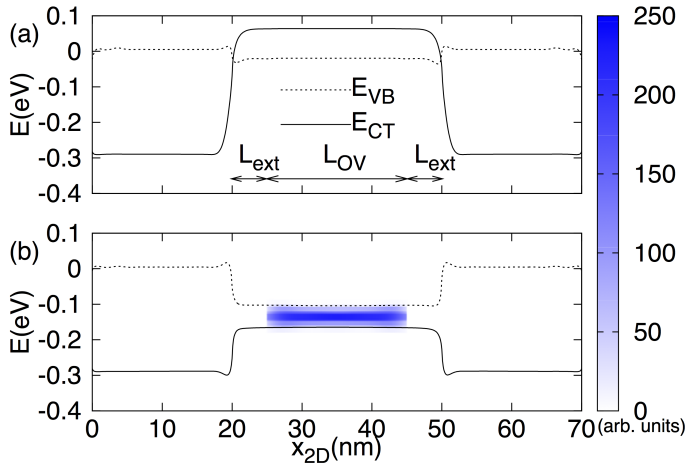

FIGURE 5.5: Energy spectrum of the current density with the top layer conduction band edge E_{CT} and the bottom layer valence band edge E_{VB} vs. x_{2D} (see Fig 5.2) for: (a) $V_{TG}= -0.2$ V and (b) $V_{TG}= 0.2$ V. Other parameters: L_{ext}=5 nm, $V_{BG}= -0.5$ V and N_D=4×10^{12} cm^{-2}.

suppressing the tunneling current between them. This corresponds to the off-state represented in Fig.5.5(a). Note that the tunneling current is so small here that cannot be observed with the color scale used in the figure. By increasing the top gate voltage V_{TG}, the potential in the top layer increases, thus lowering E_{CT}. When E_{CT} is moved below E_{VB} in the overlap region, the inter-layer tunneling is strongly enhanced. This is the on-state reported in Fig.5.5(b). The current is non-null inside the energy window [E_{CT}, E_{VB}], with a maximum at the middle energy (E_{CT}+E_{VB})/2, which is consistent with the previous analysis reported in Ref.[17]. Being based on quantum tunneling and not suffering from the thermionic limit, this switching mechanism can enable very small SS values. In what follows, we analyze some key design elements that determine the SS and that can be optimized to improve the TFET performances.

While the MOSFETs show a fairly constant SS, in TFETs the SS changes with the gate voltage. Therefore, in order to compare the SS of different device configurations, the average SS is calculated from the I_{DS}-V_{TG} characteristics by the following formula

$$SS = \frac{V_{TG,TH} - V_{TG,OFF}}{\log_{10}(I_{TH}/I_{OFF})} \tag{5.4}$$

where $V_{TG,TH}$ and $V_{TG,OFF}$ correspond to the top gate voltage V_{TG} at I_{DS}=I_{TH}=10 pA/ μm and I_{DS}=I_{OFF}=1 μA/ μm respectively, which is the requirement for low-power transistors defined by the *ITRS* [1].

In the I_{DS}-V_{TG} characteristics throughout this chapter, the curves with filled triangle symbols refer to the results obtained for the reference device configuration with the parameters indicated in Tab.5.2.

TABLE 5.2: Reference device configuration

L_{ext}(nm)	L_{OV}(nm)	N_D(cm^{-2})	V_{BG}(V)
5	20	4×10^{12}	-0.5

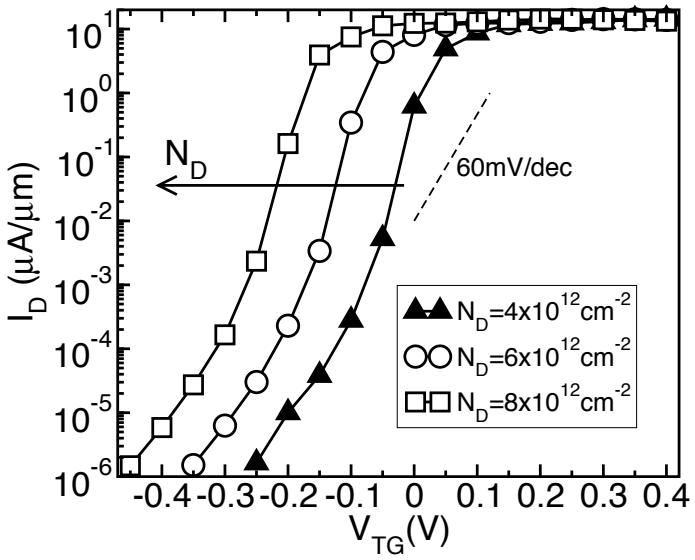

FIGURE 5.6: I_{DS} vs. V_{TG} for different doner concentration N_D in the MoS_2 top layer with $V_{BG} = -0.5$ V. Other parameters: $L_{ext} = 5$ nm and $V_{DS} = 0.3$ V.

5.3.1 Role of doping and back-gate potential

Figure 5.6 reports the transfer characteristics I_{DS}-V_{TG} of the device for different chemical donor concentrations N_D in the MoS_2 top layer. The threshold (top gate) voltage decreases as N_D increases. However, the SS turns out to remain fairly constant, since the I_{DS}-V_{TG} curve just shifts along V_{TG}. The increase of n-doping in MoS_2 induces a lowering of the E_{CT}, thus decreasing the gap between E_{CT} and E_{VB} in the off-state. Subsequently, a smaller V_{TG} can inverse the E_{CT} and E_{VB} in the overlap region and turn the TFET on. A similar behavior is observed when decreasing the back-gate voltage V_{BG}, which corresponds to increasing the electrostatic p-doping in the WTe_2 bottom layer. Fig.5.7 reports the I_{DS}-V_{TG} curves for V_{BG} varying from -1 V to -0.5 V.

These results, obtained for V_{DS}= 0.3 V, indicate that the transistor performances should not be much affected by chemical/electrostatic doping, which simply results in a shift of the transfer characteristic.

However, this is no more the case when V_{DS} is very small. Fig.5.8 illustrates the output characteristics I_{DS} vs. V_{DS} of the device in the on-state, at $V_{TG} = V_{TG,TH} + 0.3$ V, for two different dopant concentrations and back gate voltages. When $N_D = 4 \times 10^{12}$ cm^{-2} and $V_{BG} = -0.5$ V, we observe that the supposedly linear Ohmic region at

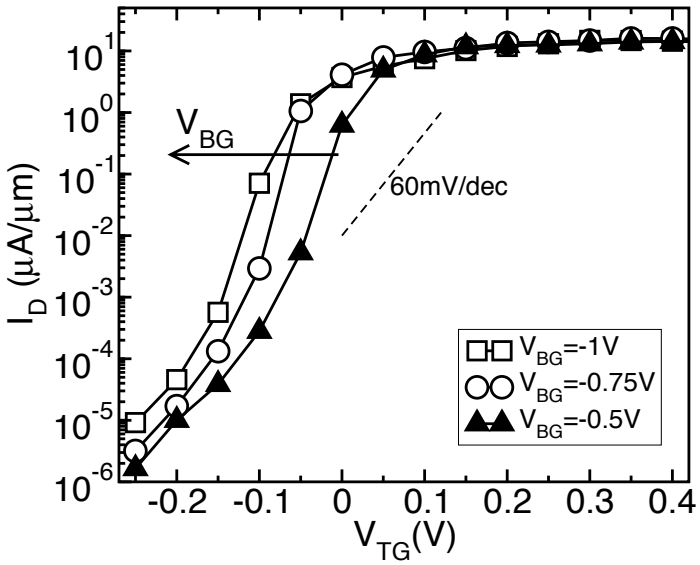

FIGURE 5.7: I_{DS} vs. V_{TG} for different back gate voltage V_{BG} with $N_D = 4 \times 10^{12}$ cm^{-2}. Other parameters: $L_{ext} = 5$ nm and $V_{DS} = 0.3$ V.

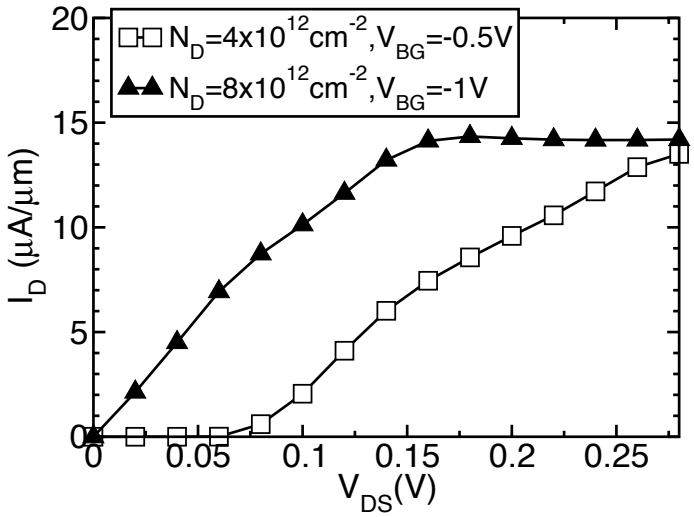

FIGURE 5.8: Output characteristics I_{DS}-V_{DS} of the TFET at $V_{DS} = 0.06$ V for $N_D = 4 \times 10^{12}$ cm^{-2} and $V_{BG} = -0.5$ V, and for $N_D = 8 \times 10^{12}$ cm^{-2} and $V_{BG} = -1$ V, and with the source/drain Fermi level $\mu_S = 0$ eV and $\mu_D = -0.06$ eV.

small V_{DS} is deteriorated. This effect is due to non-degenerate condition in the drain region of the top MoS_2 layer, as shown in Fig.5.9. In fact, with lower chemical doping concentration in the MoS_2 layer, the E_{CT} (the solid lines) near the drain moves up to an energy above the drain Fermi level $\mu_D = -0.06$ eV. The electrons have then fewer states available to pass from the channel region to the drain region, which entails the observed current suppression. Similarly, the back gate voltage affects the electrostatic doping in the source region of the bottom WTe_2 layer. Consequently, a low $|V_{BG}|$ value decreases the carrier density in the WTe_2 layer and therefore the current I_{DS}. In order to avoid this problem, the chemical doping N_D and the back gate

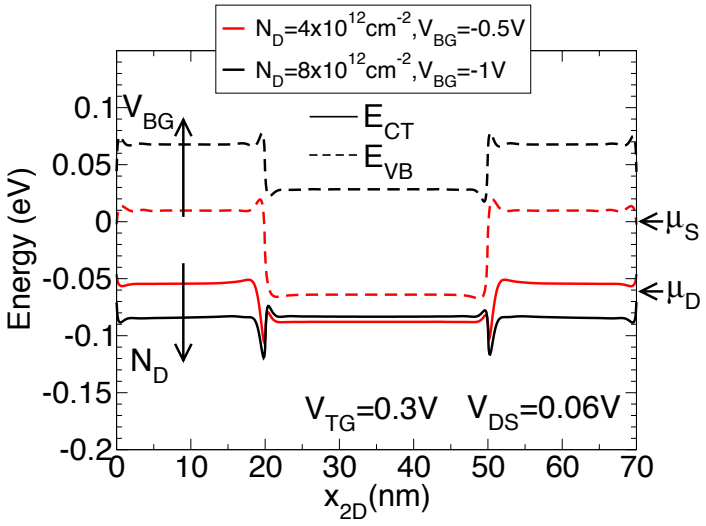

FIGURE 5.9: Conduction band and valence band edge profiles at $V_{DS} = 0.06$ V for $N_D = 4 \times 10^{12}$ cm^{-2} and $V_{BG} = -0.5$ V, and for $N_D = 8 \times 10^{12}$ cm^{-2} and $V_{BG} = -1$ V, and with the source/drain Fermi level $\mu_S = 0$ eV and $\mu_D = -0.06$ eV.

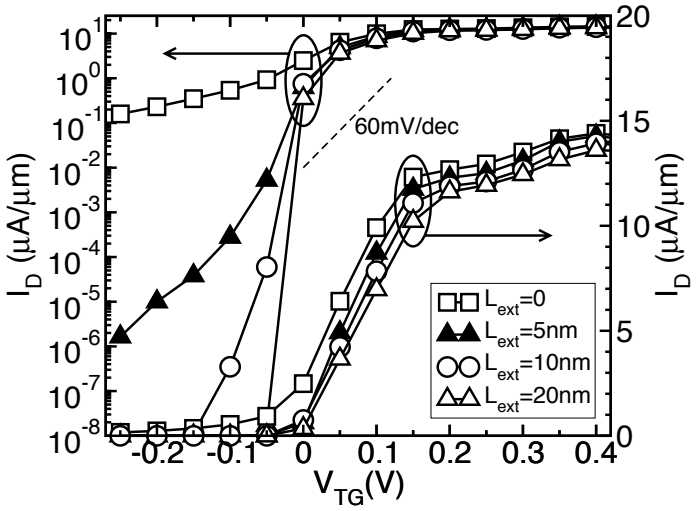

FIGURE 5.10: Transfer characteristics I_{DS} vs. V_{TG} for different values of the top gate extension length L_{ext}. The SS values are 42, 15, and 7 mV/dec for L_{ext} of 5, 10 and 20 nm, respectively.

potential $|V_{BG}|$ need to be increased. As shown in Fig.5.8, with $N_D = 8 \times 10^{12}$ cm^{-2} and $V_{BG} = -1$ V, the low V_{DS} part of the output characteristics I_{DS}-V_{DS} becomes more linear.

5.3.2 Role of top gate extension region

In the simulations discussed so far, the top gate extends for a length $L_{ext} = 5$ nm beyond each side of the overlap region. In this Section, the influence of L_{ext} is studied. As we will see, L_{ext} plays an important role for assuring the off-state performance of this TFET, i.e. to assure a low SS. Fig.5.10 shows the transfer characteristic I_{DS}-V_{TG} of the TFET obtained with different values of L_{ext}.

For the configuration with no extension region ($L_{ext} = 0$), the SS rapidly degrades and the current in the off-regime of the TFET increases significantly. In order to understand this behavior, Fig.5.11 shows the energy-resolved tunneling current density spectra of the device in the off-state, for two different values of L_{ext}. All the other parameters, as L_{OV} and V_{BG}, are exactly the same as in the previous simulations. The effect of a non-zero L_{ext} is to push the crossing between E_{VB} of WTe_2 and the E_{CT} of MoS_2 far from the overlap region, where the tunneling between the 2D layers is possible. This suppresses the edge tunneling current when the device is in off-state.

By increasing the L_{ext} we can significantly further decrease the SS of this TFET. With $L_{ext} = 20$ nm, the device can even attain SS = 7 mV/dec. To explain such a result, we can consider the case of Fig.5.11(a) and follow the path of electrons with a fixed energy. In fact, since in this simulation only elastic phonon scattering is included, this energy is preserved by the electrons throughout their travel from source to drain. In Fig.5.12, two sketches are drawn to illustrate this process. When the electrons are injected from the source, they need to have energy close or below the valence band E_{VB} in the overlap region in order to find available states. As mentioned before, in this region the states are given by a superposition of the top layer and the bottom layer states. The degree of mixing is very small in the off-state, and it depends on the inter-layer coupling and potential difference. By virtue of this coupling, electrons can marginally pass to the top layer. At this point, they need to evacuate the overlap region to end in the conduction band in the drain top layer. To do this, they have to pass through the extension region. As shown in Fig.5.12(b), the E_{CT} in the extension region is much higher than in the drain region, thus representing an *intra-layer* potential barrier for electrons, which have to tunnel through evanescent states. Such a tunneling process is *exponentially* suppressed when increasing L_{ext}. This determines the reduction of the current with the length of the gate extension region. Moreover, the spectral tunneling current is maximum at energies close to the top of the WTe_2 valence band, because the intralayer tunneling distance increases at smaller energy values, together with the reduced mixing of states belonging to the two layers in the overlap region. Incidentally, for a given V_{TG} in the off-state, the current is verified to decrease *exponentially* with L_{ext}, as expected on the basis of our explanation. In conclusion, the top gate extension length L_{ext} plays a central role in the suppression of the off-state current and it is thus a very important design parameter for the optimization of the sub-threshold performance of this kind of devices.

The values of SS predicted in our simulations are very competitive with respect to experiments. However, it is important to remark that in the present simulation

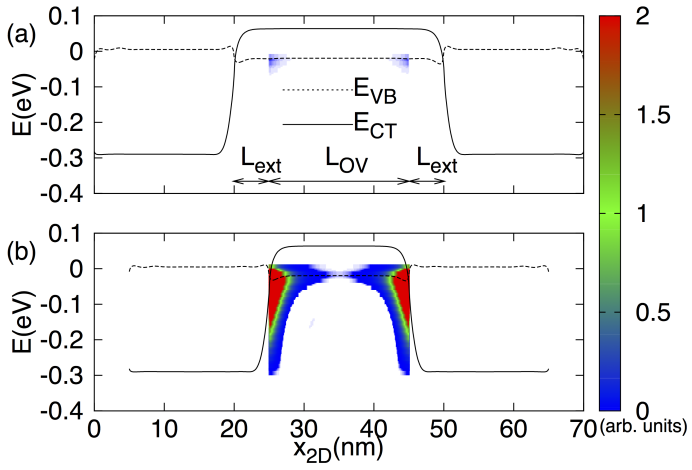

FIGURE 5.11: Tunneling current spectra in off-state at V_{TG}=-0.2 V for two different L_{ext} values: (top) L_{ext}=5 nm and (bottom) L_{ext}=0.

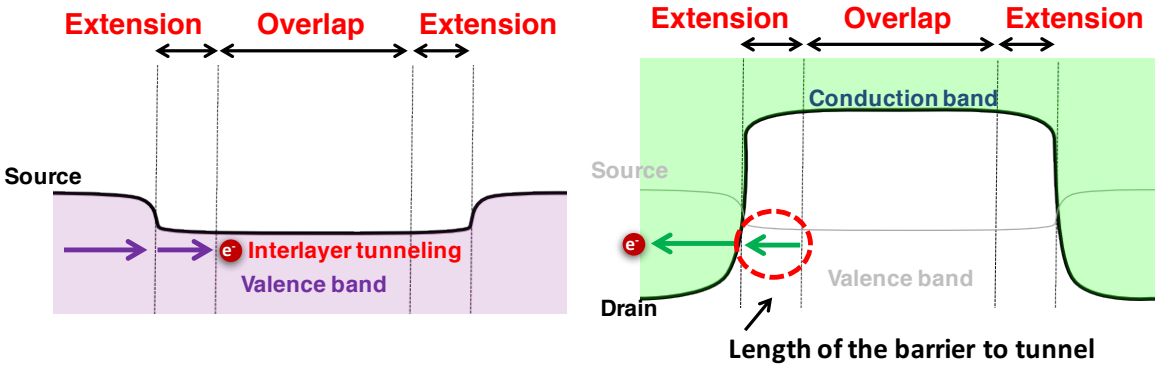

(A) (B)

FIGURE 5.12: Sketches of the conduction band and valence band edge profiles in the off state with the path of electrons (A) from source to overlap region (B) and then to drain. The shadowed areas indicate the possible states for electrons.

approach we have not considered the presence of defects and traps, which could deteriorate the SS by activating possible paths for trap-assisted, inelastic tunneling in the off-state of the TFET [14, 15]. Our results thus represent an upper limit for the real transistor performances. Nevertheless, the influence of design parameters on the device performance should still have the same trend, thus unchanging our conclusions.

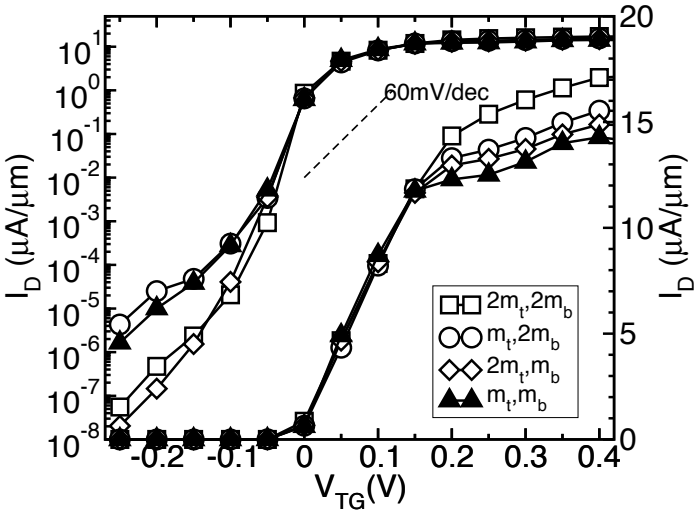

FIGURE 5.13: I_{DS} vs. V_{TG} for different values of the effective mass in the top layer (m_t) and in the bottom layer (m_b). Other parameters: $N_D = 4 \times 10^{12}$ cm^{-2}, $L_{ext} = 5$ nm, $L_{OV} = 20$ nm, $V_{BG} = -0.5$ V and $V_{DS} = 0.3$ V.

5.3.3 Effective mass

The previous discussion in Sec.5.3.2 shows that the *intra-layer* tunneling in the gate extension region affects the off-state current and thus SS considerablely. This suggests another possible optimization of the TFET performance by choosing the 2D materials with larger effective masses. In the gate extension region, the electron states decay more rapidly for larger in-plane effective masses, thus determining a further suppression of the off-state current and therefore a smaller SS. Fig.5.13 illustrates the I_{DS}vs. V_{TG} characteristics of the TFET for different sets of effective masses in the top and bottom layers with the same gate extension length L_{ext}. As expected, the off-state tunneling current is reduced by increasing the effective mass in the top layer m_t, whereas it is almost unchanged by doubling the effective mass in the bottom layer m_b. This is further evidence that the off-current is determined by evanescent states in the top layer tunneling from the channel to the drain region. In addition to this, an increase of on-current is obtained by doubling the effective masses (see Fig.5.13), because electrons can have more available states in MoS_2 and/or WTe_2 to move from source to drain. In conclusion, using materials with larger effective mass for the drain layer is an optimization option to improve both the on and the off-state device performance.

5.3.4 Scalability of device

This Section investigates the scalability of this TFET. Different L_{OV} values are considered while keeping the other parameters unchanged. Fig.5.14 shows the computed I_{DS} vs. V_{TG} characteristics and Fig.5.15 summarizes the extracted values of the I_{ON} at $V_{TG} = 0.3$ V and the SS calculated by using the Eq.5.4. The SS remains around

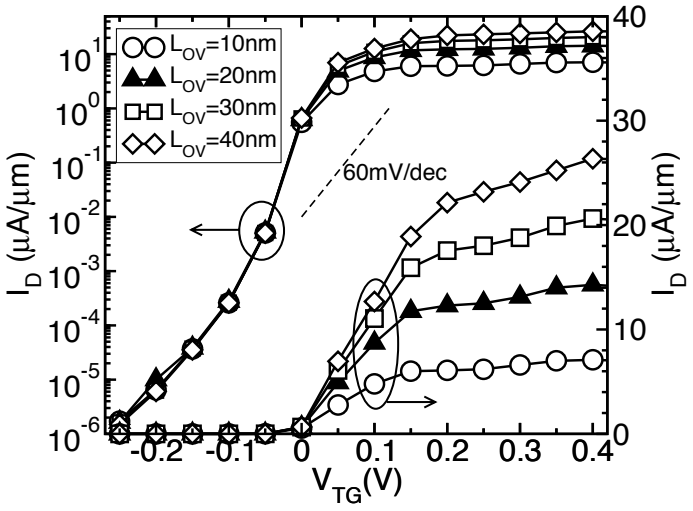

FIGURE 5.14: I_{DS} vs. V_{TG} for different values of the overlap length L_{OV}. Other parameters: $N_D = 4 \times 10^{12}$ cm^{-2}, $L_{ext} = 5$ nm, $V_{BG} = -0.5$ V and $V_{DS} = 0.3$ V.

40 mV/dec for different L_{OV} values. As we discussed previously in Sec.5.3.2, due to the intra-layer tunneling from overlap region to drain, the off-current is dominated by edge tunneling, as shown in Fig.5.11. Consequently, the SS is unaffected by the scaling of L_{OV}, which is a favorable behavior for ultra-scaled switches.

Figure 5.15(b) shows that the on-current increases proportionally with L_{OV} up to about $L_{OV} = 30$ nm. For larger L_{OV}, I_{ON} increases sublinearly with L_{OV}. This can be understood by looking at the spatial distribution of the current density tunneling from bottom layer to top layer $J_{B\to T}$(integrated along transverse direction) in Fig.5.16 for $V_{TG} = 0.3$ V, in the on-state. The $J_{B\to T}$ is zero outside of the overlap region, where the two layers are not coupled, and has larger values on the edges of the overlap region than on its center. For large L_{OV}, for example 100 nm, the $J_{B\to T}$ gradually decreases from the edges to the center of the overlap region. A possible explanation is that the in-plane current in the bottom source layer decreases to the center since part of it tunnels into the top drain layer, thus decreasing the tunneling current density $J_{B\to T}$. Because the tunneling probability related to H_{tunn} is considered constant inside the overlap region, we can easily deduce that $J_{B\to T}$ follows the exponential decrease from the edges to the center as

$$J_{B\to T}(x_{2D}) = J_0 \left(e^{-(x_{2D}-x_1)/d} + e^{-(x_2-x_{2D})/d} \right) \tag{5.5}$$

where J_0 is the $J_{B\to T}$ value at the edges of the overlap region, x_1 and x_2 are the x_{2D} coordinates of the edges and d is related to the tunneling probability from bottom layer to top layer. This function with $d = 62$ nm fits quite well the simulation results for $L_{OV} = 100$ nm, as shown in Fig.5.16.

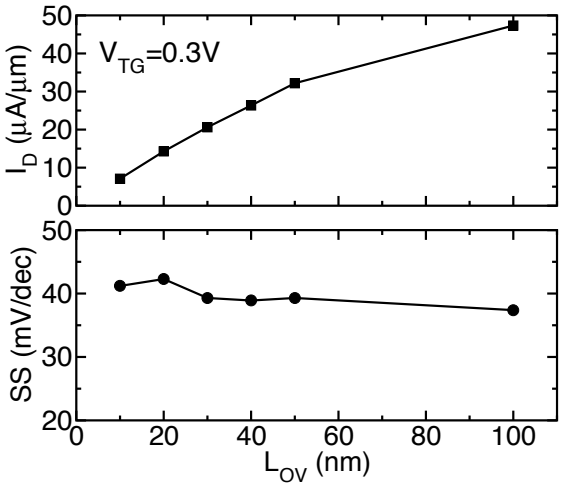

FIGURE 5.15: The extracted on-current (top) and average SS (bottom) vs. L_{OV} from Fig.5.14. Other parameters: $N_D = 4 \times 10^{12}$ cm^{-2}, $L_{ext} = 5$ nm, $V_{BG} = -0.5$ V and $V_{DS} = 0.3$ V.

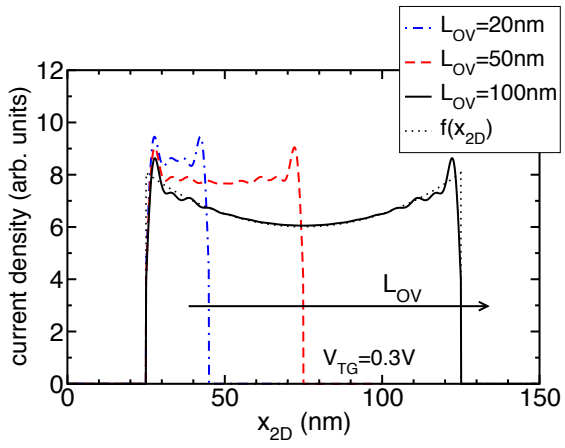

FIGURE 5.16: Spatial profile of the tunneling current density integrated along transverse direction in on-state at $V_{TG} = 0.3V$ for the simulations with $L_{OV} = 20$, 50 and 100 nm in Fig.5.14. The fitting function $f(x_{2D})$ is discussed in Sec.5.3.4.

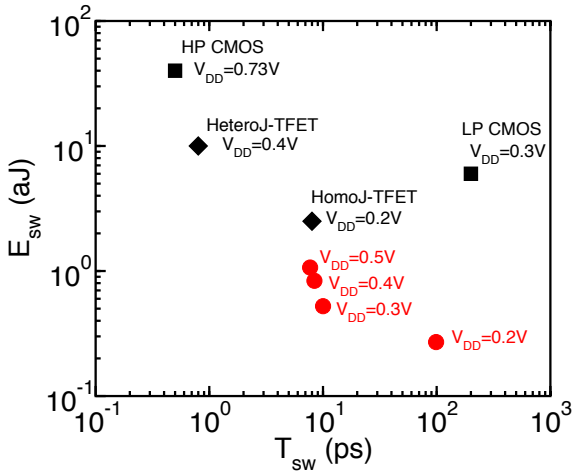

FIGURE 5.17: The intrinsic switching energy and delay for the inter-layer TFET with $V_{\mathrm{DD}}$from 0.2 to 0.5 V with $L_{\mathrm{OV}} = 20$ nm and $L_{\mathrm{ext}} = 5$ nm.

5.3.5 Delay and energy metrics

In order to estimate the dynamic performance of this TFET and compare to some other recent TFETs and MOSFETs in the experiments, we evaluated some simple metrics for the delay and energy corresponding to the switching of a digital inverter with the same definition in [147]. In particular, the first-order estimation of the switching time T_{sw} is defined as

$$T_{\mathrm{sw}} = \frac{Q_{\mathrm{ON}} - Q_{\mathrm{OFF}}}{I_{\mathrm{ON}}}, \tag{5.6}$$

where Q_{ON} and Q_{OFF} are the sum of the mobile charge in the two 2D layers for V_{TG}=$V_{\mathrm{TG,OFF}}$+V_{DD}, V_{DS}=V_{DD}, and for V_{TG}=$V_{\mathrm{TG,OFF}}$; V_{DS}=V_{DD}, respectively. A similar simple metric for the switching energy E_{sw} can be defined as

$$E_{\mathrm{sw}} = V_{\mathrm{DD}}(Q_{\mathrm{ON}} - Q_{\mathrm{OFF}}). \tag{5.7}$$

In Fig.5.17, I plot E_{sw} vs. T_{sw} for different operating voltage V_{DD}. As expected, for increasing V_{DD} E_{sw} increases and T_{sw} decreases. We observe a larger decrease of T_{sw} when increasing V_{DD} from 0.2 V to 0.3 V than observed at larger V_{DD} values. This is a consequence of the current saturation that this device exhibits at $V_{\mathrm{DS}} > 0.3$ V (see Fig.5.8). In Fig.5.17 we also compare this device to high-power (HP) and low-power (LP) CMOS and to TFETs as reported in Refs. [148, 149]. As can be seen, the TFET simulated in this work can be quite competitive for low-power applications.

5.4 Summary

This Chapter presented the results of a self-consistent quantum transport simulation study of vertical TFETs based on WTe_2 and MoS_2 monolayers with an h-BN interlayer, in terms of performance and the possible optimization. In particular, in Sec.5.3.1, I have shown that a larger chemical doping in the top-layer and a more negative V_{BG} can result in a well-behaved I_{DS} vs. V_{DS} output characteristics at small V_{DS}. In Sec.5.3.2 it was predicted that the device can reach an extremely steep sub-threshold slope SS. It was shown that the top gate extension L_{ext} is extremely important for a good SS and to limit the off-state current by suppressing the intra-layer tunneling in the off-state. In Sec.5.3.4, a fairly good scalability of the device has also been proven. Finally, in Sec.5.3.5 the dynamic switching performance of this TFET was shown to be theoretically very attractive comparing to the other state-of-the-art logical transistors. In summary, this Chapter suggested that carefully designed MoS_2/h-BN/WTe_2 vertical TFETs can offer excellent and stable SS values (< 45 mV/dec) and therefore represent a promising technology for future low-power nanoelectronics.

Chapter 6

Van der Waals Tunnel-FETs: 3-D quantum-transport simulations

Recently, van der Waals tunneling and Esaki diodes have been experimentally demonstrated [26, 27], and a first device with sub-thermionic characteristics realized [28], but the design of van der Waals tunnel transistors (vdW-TFETs) is still largely unexplored [20].

This Chapter presents a self-consistent three-dimensional quantum transport simulation for electron transport in vdW-TFETs based on MoS_2 and WTe_2 monolayers. The results in this Chapter have been published in [150, 151]. In order to describe the van der Waals coupling between the 2-D gapped crystals, we propose in Sec.6.2 a model Hamiltonian relying on few physical parameters, which we calibrate against DFT band structure calculations. This Chapter addresses several fundamental as well as design aspects related to vdW-TFETs, including the current scaling with the device area in Sec.6.3.2, the impact of the top gate geometrical alignment in Sec.6.3.1 and the back-oxide thickness on the device performance in Sec.6.3.3. As an important innovative contribution, the simulations in Sec.6.3.4 take into account the influence of inelastic phonon scattering on the device operation and on the sub-threshold swing.

6.1 Device description

The simulated vdW-TFET is sketched in Fig.6.1. This vdW-TFET combines a WTe_2 bottom layer acting as the source and an MoS_2 top layer acting as the drain. The lattice parameters for unstrained WTe_2 and MoS_2 monolayers are 3.55 Å and 3.19 Å, respectively. In these simulations, however, we followed [19] and introduced a compressive strain on WTe_2 and tensile strain on MoS_2 layer to obtain a commensurate lattice parameter of 3.411 Å in the two materials. With such a strain, WTe_2 is expected to be more stable in its H-phase, as suggested by DFT calculations [152], so that the simulations actually refer to an H-phase WTe_2. The corresponding energy gaps for the strained WTe_2 and MoS_2 monolayers are 1.77 eV and 0.321 eV, respectively. The van der Waals gap between the two 2-D layers acts as the tunneling

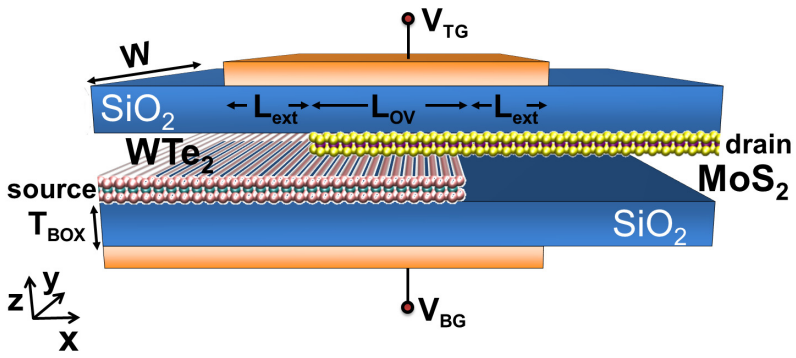

FIGURE 6.1: Sketch of the vdW-TFET structure considered in the simulations. L_{OV} denotes the length of the overlap region between the MoS_2 top and the WTe_2 bottom layer. L_{ext} is the top gate extension beyond the L_{OV} region. $L_{\mathrm{TG}} = L_{\mathrm{OV}} + 2L_{\mathrm{OV}}$ is the length of the top gate.

barrier, which is assumed 0.35 nm thick and with the same dielectric constant as air ($\kappa = 1.0$). The two 2-D layers are assumed to have a thickness of 0.6 nm [96, 153], and relative dielectric permittivity of κ=5.7 for the WTe_2 and κ=4.8 for the MoS_2 [154]. The length of the overlap region between the two 2-D layer is denoted by L_{OV}, while L_{ext} indicates the top gate extension length. The SiO_2 layers (κ=3.9), acting as top-gate and back-gate oxide, are assumed 1 nm thick, except in the Sec.6.3.3. We consider a chemically n-doped MoS_2 layer with $N_{\mathrm{D}} = 4 \times 10^{12}$ cm^{-2}, while the WTe_2 layer is electrostatically doped by the back-gate with $V_{\mathrm{BG}} = -0.5$ V.

Figure 6.2(a) shows a sketch of the band diagram that corresponds to a cross-section of the overlap region along the vertical z direction in the device off- and on-state, in order to illustrate the working principle. At low V_{TG} the conduction band minimum (E_{CT}) of the top MoS_2 layer is higher than the valence band maximum (E_{VB}) of the bottom WTe_2 layer, thus suppressing the tunneling current and resulting in very low off-current. By increasing V_{TG}, E_{CT} of MoS_2 is lowered so as to cross and then move below E_{VB} of WTe_2, hence enabling the vertical band-to-band tunneling.

6.2 Simulation model

6.2.1 Model Hamiltonian

In order to describe this system, the following effective mass model Hamiltonian is adopted

$$H(\boldsymbol{k}) = \begin{bmatrix} E_0 + \frac{\hbar^2 k^2}{2m_{\mathrm{c}}} & t_\perp \\ t_\perp & -\frac{\hbar^2 k^2}{2m_{\mathrm{v}}} \end{bmatrix} \tag{6.1}$$

where $t_\perp$ is the coupling energy between the WTe_2 valence and the MoS_2 conduction band. The parameters E_0, m_{c} and m_{v} refer to the system of uncoupled layers, and

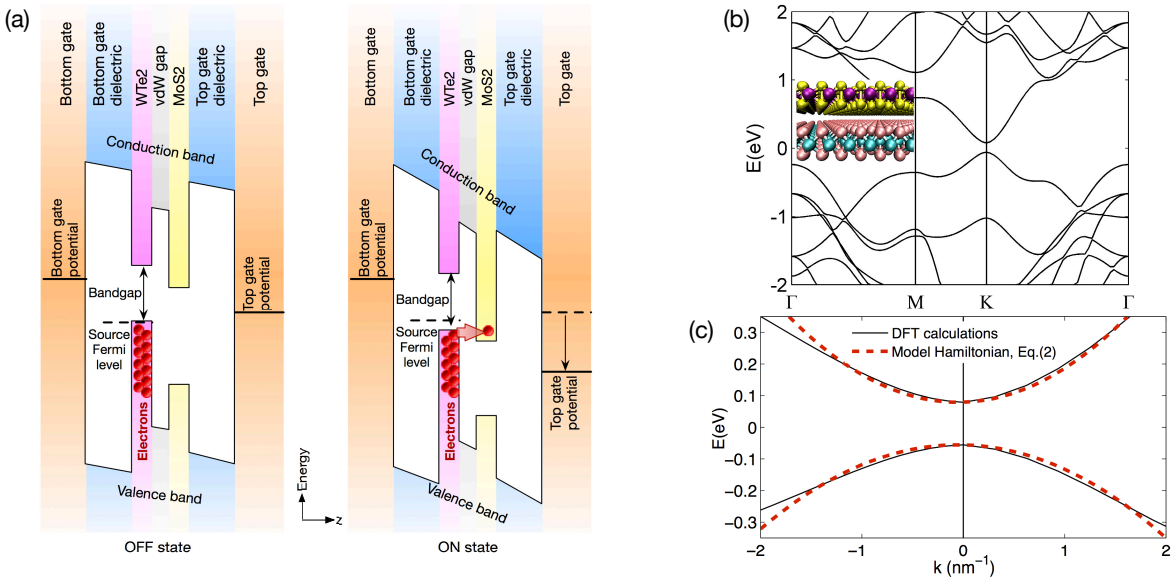

FIGURE 6.2: (a) Sketch of the conduction and the valence band edges in the center of the overlap region along the z direction. (b) DFT band structure of the coupled WTe_2-MoS_2 system reported in the inset. (c) Band-structure close to the K point for the coupled WTe_2-MoS_2 system. The parameters of the model Hamiltonian are calibrated so as to obtain a close agreement with DFT calculations.

denote the energy gap between the WTe_2 valence band and the MoS_2 conduction band, and the effective mass in MoS_2 and in WTe_2, respectively.

6.2.2 Calibration of tunneling coefficient

For the WTe_2-MoS_2 coupled system, the energy bands, the gap and the effective masses can be analytically expressed as

$$E_{\pm}(\boldsymbol{k}) = \frac{E_0}{2} + \frac{\hbar^2}{2}\frac{m_c - m_v}{2m_c m_v}k^2 \pm \sqrt{t_\perp^2 + \left[\frac{E_0}{2} + \frac{\hbar^2}{2}\frac{m_c + m_v}{2m_c m_v}k^2\right]^2} \tag{6.2}$$

$$E_g = E_+(\mathbf{0}) - E_-(\mathbf{0}) = \sqrt{4t_\perp^2 + E_0^2} \tag{6.3}$$

$$m_\pm = \frac{\partial^2 E_\pm}{\partial k^2}(\mathbf{0}) = \frac{2m_c m_v\sqrt{1 + 4t_\perp^2/E_0^2}}{(m_v - m_c)\sqrt{1 + 4t_\perp^2/E_0^2} \pm (m_v + m_c)}\,. \tag{6.4}$$

Hence, as it can be seen in Eq.(6.3) and (6.4), the coupling between the two materials enforced by $t_\perp$ modifies both the energy gap and the effective masses of the coupled system compared to the two isolated materials. It is thus possible to estimate the parameters $t_\perp$ and E_0 in the Hamiltonian by comparing the energy band structures of coupled and uncoupled 2-D layers. In order to obtain the energy bands, we used plane wave DFT simulations based on the VASP code [155] with

a cut-off energy of 33Ry, electron–ion interactions described by the projector augmented wave method [156], and generalized gradient approximation of Perdew-Burke-Ernzerhof functional [157]. Self-consistent solutions were obtained by employing the (24×24×1) Monkhorst-Pack grid of k-points and a vacuum region of 28 Å. As shown in Fig.6.2(b), from the simulation of coupled and uncoupled layers, we extracted the parameters of the model Hamiltonian as $E_0 = 134$ meV, $t_\perp \approx 6$ meV, $m_\mathrm{c} = 0.391\ m_0$ and $m_\mathrm{v} = 0.543\ m_0$, corresponding to $E_\mathrm{g} = 135$ meV, $m_+ = 0.392\ m_0$, $m_- = 0.548\ m_0$ for the WTe_2-MoS_2 coupled system. The small changes from E_0 to E_g and from m_c, m_v to $m_\pm$ are consistent with the weak van der Waals coupling. Figure 6.2(c) shows that the band structure in the coupled WTe_2-MoS_2 system obtained by (6.2) and with the calibrated E_0, $t_\perp$, m_c, m_v parameters is in good agreement with DFT calculations close to the K point.

6.2.3 Transport model

The wave-function is defined as $\Phi(\mathbf{r}) = (\psi(\mathbf{r}), \phi(\mathbf{r}))^\mathrm{T}$, where $\psi(\mathbf{r})$ and $\phi(\mathbf{r})$ are the wave-functions in the WTe_2 and MoS_2 layers, respectively, and $\mathbf{r}$ is the coordinate in the (x,y) plane. Hence, the real-space Hamiltonian $\hat{H}(\partial_x, \partial_y)$ derived from $H(\boldsymbol{k})$ in (6.1) reads

$$\hat{H}(\partial_x, \partial_y)\Phi(\mathbf{r}) = \begin{bmatrix} E_0 - \frac{\hbar^2}{2m_\mathrm{c}}(\partial_x^2 + \partial_y^2) & t_\perp \\ t_\perp & \frac{\hbar^2}{2m_\mathrm{v}}(\partial_x^2 + \partial_y^2) \end{bmatrix} \begin{bmatrix} \psi(\mathbf{r}) \\ \phi(\mathbf{r}) \end{bmatrix} . \tag{6.5}$$

By using a five-point stencil finite difference discretization, the Hamiltonian is mapped into a block tridiagonal matrix with non-zero submatrices $H(i,j)$, where i identifies the transverse section of the 2-D layers at position $x = x_i$ and j=$i-1$, i or $i+1$. Each $H(i,j)$ is a square matrix with rank $2N_y$ with N_y being the number of discretization points along the y direction (see Fig.6.1).

The NEGF formalism, which is used to solve the transport problem, was discussed previously in Chapter 3. In these simulations, both elastic acoustic and inelastic optical phonon scatterings are considered in the SCBA.

The results of NEGF simulations allow us to obtain charge density and current density in the 2-D layers. Subsequently, the 2-D charge density is converted to a 3-D charge density by distributing it over the layer thickness $z_\mathrm{th} = 0.6$ nm according to a normalized envelope function $a(z) = a_0 \cos(z/z_\mathrm{th}\pi)^2$ for $z \in [-z_\mathrm{th}/2, z_\mathrm{th}/2]$ and $a_0 = 2/z_\mathrm{th}$. This volumetric charge density is used in the non-linear Poisson equation, which is solved in entire 3-D domain of the device for the electrical potential field. The simulation repeats this Schrödinger-Poisson self-consistent cycle until the potential converges (see Fig.4.4 for the simulation flowchart).

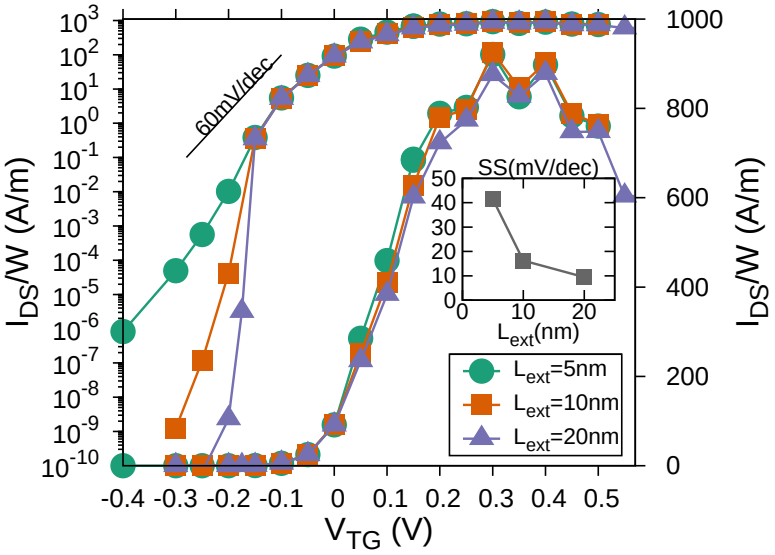

FIGURE 6.3: $[I_{DS}/W]$ vs. V_{TG} at $V_{DS} = 0.3$ V for different lengths L_{ext} of the top gate extension (see Fig.6.1). Other parameters: $L_{OV} = W = 20$ nm, $T_{BOX} = 1$ nm. Inset: SS versus L_{ext}.

6.3 Results and discussions

In this Section, I examine several design options and relate them to the physical mechanisms involved in the operation of vdW-TFETs. I present the role of top gate extension in Sec.6.3.1, of the overlap length in Sec.6.3.2, and of the back-oxide thickness in Sec.6.3.3. The simulations in these Sections only include the coupling of electrons with acoustic phonon modes (D_{ac}=3 eV [158]). In Sec.6.3.4, I add scattering with inelastic optical phonons and discuss their impact on the SS of the vdW-TFETs. In the reality these diffusive phenomena cannot be eliminated, and substantially affect the device performance. In Sec.6.3.5, I study the large overdrive regime.

6.3.1 Effect of the top gate extension

Figure 6.3 illustrates the transfer characteristic I_{DS}-V_{TG} for L_{ext}=5, 10 and 20 nm. The inset in this figure highlights the substantial subthreshold swing (SS) improvement at large L_{ext}. In particular, for $L_{ext} = 20$ nm the device can attain a SS as low as 11 mV/dec. In this work, all the SS values correspond to average values for I_{DS} between 10 pA/ μm and 1 μA/ μm as defined previously in (5.4). In order to explain this feature, Fig.6.4 shows the LDOS versus the transport direction in the off-state for $L_{ext} = 10$ nm and 5 nm. The reference energy is the source Fermi level $E_{F,S} = 0$ eV.

Electrons are injected from the left source contact into the valence band of WTe_2. When reaching the overlap region, they can tunnel into the top MoS_2 layer, where,

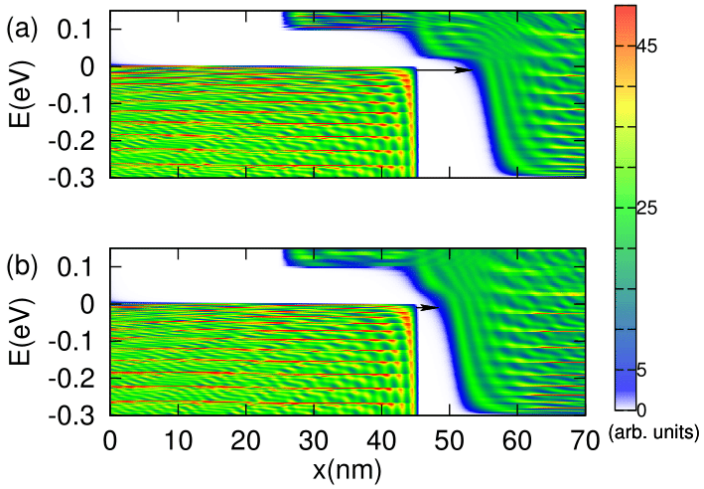

FIGURE 6.4: Energy spectra of LDOS integrated over the transverse direction y (see Fig.6.1) for $L_{\text{ext}} = 10$ nm (top) and $L_{\text{ext}} = 5$ nm (bottom) in the sub-threshold regime ($V_{\text{TG}} = -0.2$ V). Arrows indicate the electron tunneling path. The reference energy is the source Fermi level $E_{\text{F,S}} = 0$ eV.

however, their energy corresponds to states deep in the energy band gap. Electrons have to continue their tunneling path in the band gap of MoS_2 through the top gate extension region to finally reach the conduction band in the drain region. By increasing the length L_{ext}, we increase the length of the intralayer tunneling region, thus *exponentially* suppressing the off-state current. This explains the large sensitivity of I_{DS} to L_{ext} in Fig.6.3. For the same reason, the interlayer tunneling in the off-state occurs essentially at the edge of the overlap region closer to the drain. The subthreshold current can be written as

$$I = I_0 T e^{\beta L_{\text{ext}}(V_{\text{TG}} - V_{\text{T}})}, \tag{6.6}$$

where T is the interlayer tunneling probability and β is a qualitative factor for the intralayer tunneling process. From the results in Fig.6.3, we can estimate β=5.4 (nm V)$^{-1}$ from the current values at V_{TG}=-0.2 V.

6.3.2 Effect of the overlap length

In order to investigate the scalability of the vdW-TFET, let us consider different overlap lengths L_{OV} while keeping the same top gate extension length and width $L_{\text{ext}} = W = 20$ nm. Figure 6.5 illustrates the I_{DS}-V_{TG} curves for L_{OV}= 10, 20, 30 and 40 nm. At low V_{TG}, the drain current I_{DS} is almost independent of L_{OV}. In order to provide a physical explanation for these results, we plot in Fig.6.6 (a-d) the off-state and on-state interlayer tunneling current density in the overlap region for L_{OV}= 10 and 30 nm.

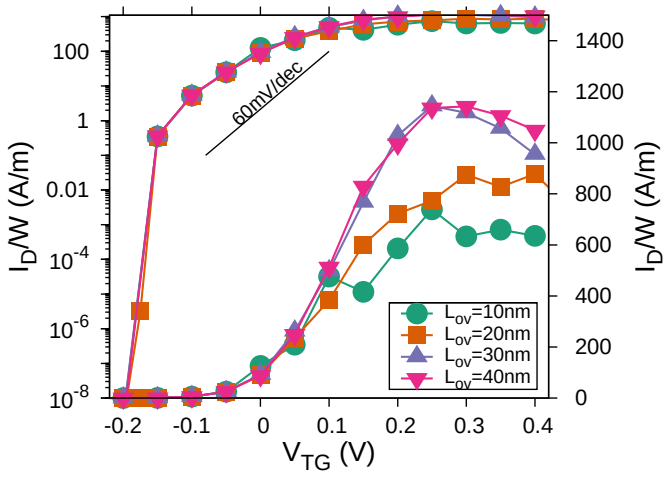

FIGURE 6.5: $[I_{DS}/W]$ vs. V_{TG} at $V_{DS} = 0.3$ V and for different lengths L_{OV} of the overlap region between the WTe_2 and the MoS_2 layers (Fig.6.1).

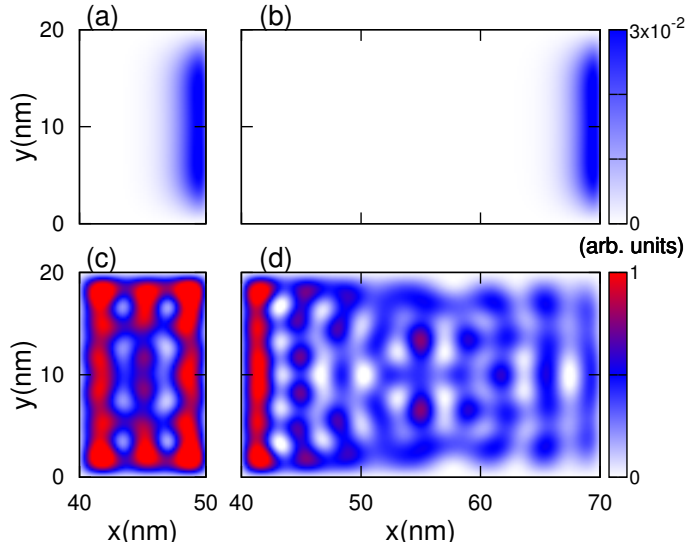

FIGURE 6.6: (colormap) Spatial distribution of the interlayer tunneling current density in the overlap region for $V_{DS} = 0.3$ V. (a),(c) L_{OV}= 10 nm; (b),(d) L_{OV}= 30 nm; (a),(b) V_{TG}= -0.2 V; (c),(d) V_{TG}= 0.1 V. (x,y)=(50,10) is the center of the overlap region (see Fig.6.1).

In the off-state, the interlayer tunneling occurs only on the edge of the overlap region closer to the drain (see Fig.6.6a,b), due to the intralayer tunneling process in the MoS_2 layer, previously discussed in Sec.6.3.1. Consequently, the overlap length L_{OV} has almost no influence on the off-state I_{DS} and the SS of the vdW-TFET.

In the on-state, the tunneling current density exhibits appreciable fluctuations along the longitudinal direction (see Fig.6.6c,d). We observe very similar features in the LDOS resolved along the x direction (see Fig.6.4). We ascribe this effect to the abrupt termination of the materials at the edges of the 2D layers, which induces standing

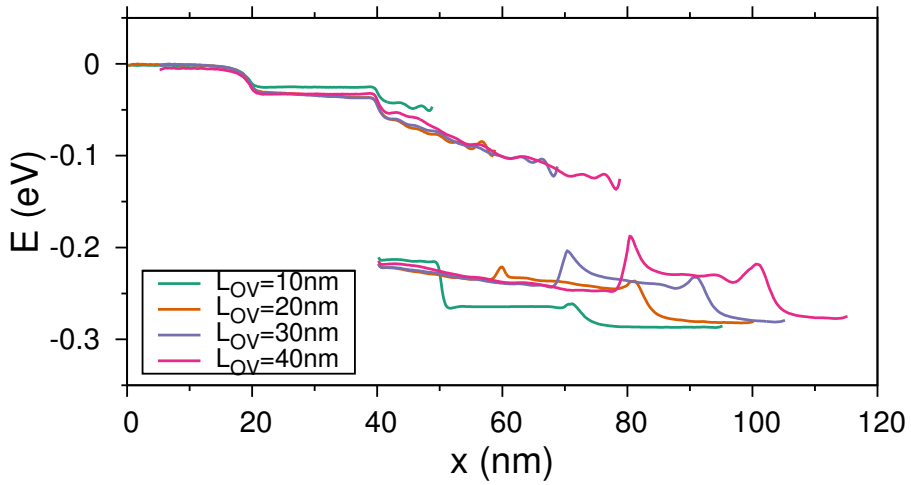

FIGURE 6.7: Top layer conduction band edge and bottom layer valence band edge along the x direction at V_{TG}=0.3 V and V_{DS}=0.3 V, for different values of L_{OV}=10, 20, 30 and 40 nm.

wave LDOS oscillations in the longitudinal direction. Since electron tunneling requires the presence of states in both the top and the bottom layers, the LDOS on the two layers modulates the tunneling current density. In conclusion, the fluctuations of the current density stem from the quantum confinement of electrons in the longitudinal direction of the overlap region. At larger V_{TG}, the wavelength of such fluctuations decreases, as expected for more energetic electrons. Very short overlap regions could entail strong confinement effects and finally affect significantly the on-current, as we can see in Fig.6.5 for $L_{OV} = 10$ nm and around $V_{TG} = 0.2$ V. For L_{OV} larger than 30 nm, however, the effects of quantum confinement in the longitudinal direction become small, the ripples in the I_{DS} versus V_{TG} characteristics tend to disappear and the I_{DS} becomes fairly independent of the overlap length, as can be seen in Fig.6.5. Such a saturation of I_{DS} with L_{OV}, also observed in analogous tight-binding simulations [20], is due to the limited density of states, scattering mechanisms and the resulting finite resistivity of the 2–D materials. As shown in Fig.6.7 and also in Fig.6.14(a), in fact, a significant voltage drop is observed along the overlap region, especially in the valence band of the bottom layer, which is more resistive than the top layer mainly because of the lower carrier density. When L_{OV} is increased, such a drop in the subband profile induces a reduction of the tunneling energy window and explains the tunneling current crowding at the edges of the overlap region, see also Fig.6.6(d). This indicates that at such high current levels the device tends to behave as a point tunneling FET. This is in contrast to what observed for TFETs based on standard semiconductors, where the line tunneling has been shown to be dominant [159, 160].

In Fig.6.6(d), the tunneling current density shows similar oscillation patterns also along the transverse direction. This is because our 3-D simulator takes into account also the confinement induced by the finite width (i.e. $W = 20$ nm) of the 2D layers.

There is admittedly a significant uncertainty in the current densities attainable in

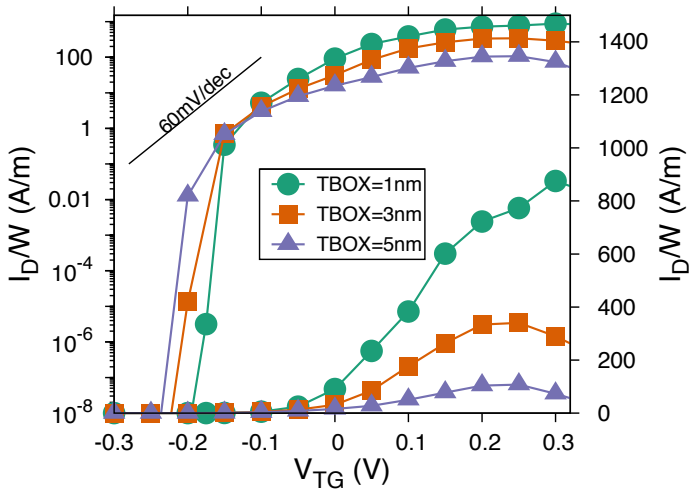

FIGURE 6.8: $[I_{DS}/W]$ vs. V_{TG} at $V_{DS} = 0.3$ V for different values of the back-oxide thickness T_{BOX}.

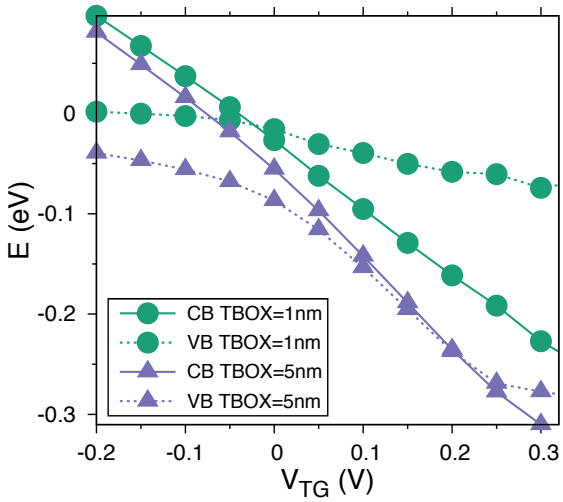

FIGURE 6.9: Valence (VB) and conduction band (CB) edges in the center of the overlap region vs. V_{TG} at V_{DS}=0.3 V for T_{BOX}=1 nm and 5 nm.

vdW-TFETs. New experimental work is indispensable in order to improve the status of models through validation and calibration. In real devices, the relevance of the voltage drop effects discussed in Fig.6.7 depends on the current level and on the resistivity of the single (or maybe few) layer(s) materials in the source and drain regions, which will finally set the range of L_{OV} in which the current scales proportionally to L_{OV}.

6.3.3 Effect of back-oxide thickness

Since the back-oxide is usually thicker than the top-oxide in the experiments, the effect of the back-oxide thickness is studied in this Section. As shown in Fig.6.8, in

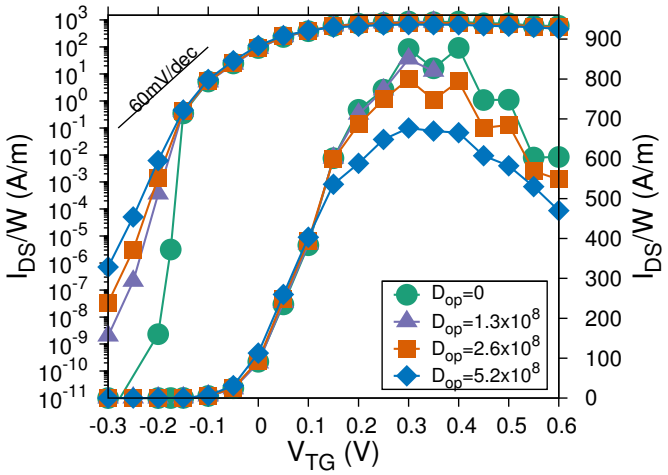

FIGURE 6.10: $[I_{DS}/W]$ vs. V_{TG} at V_{DS}= 0.3 V for different values of the optical phonon deformation potential D_{op}. The optical phonon energy is $\hbar\omega$ = 50 meV [158]. Other parameters are: D_{ac} = 3 eV, L_{ext} = 20 nm, $L_{OV} = W$ = 20 nm, T_{BOX} = 1 nm.

the on-state the I_{DS} and the trans-conductance g_m=$[\partial I_{DS}/\partial V_{TG}]$ are reduced as T_{BOX} increases. This can be explained by considering that, for a fixed V_{BG}, an increase in T_{BOX} lowers the back-gate capacitance and entails a reduced electrostatic p-type doping in the WTe_2 bottom layer, which is a smaller hole concentration in the WTe_2 layer. As a result, the WTe_2 layer is less screened from the effects of the top gate bias, so that the WTe_2 valence band edge tends to move together with the MoS_2 conduction band edge as V_{TG} increases (see Fig.6.9). This behavior is detrimental for the device operation, because it hinders the opening of the tunneling window with increasing V_{TG}, thus degrading I_{DS} and g_m. The T_{BOX} has instead only a modest impact on the SS, because for negative V_{TG} the hole density in the WTe_2 layer is preserved for all the T_{BOX}, which effectively screens the effect of V_{TG} and makes the WTe_2 valence band fairly insensitive to V_{TG}, as can be seen in Fig.6.9.

6.3.4 Effect of inelastic scattering

All previous simulations in this Chapter were performed by including only the elastic acoustic phonons. The dependence of the SS on the value of D_{ac} is verified to be very weak. The on-current is reduced while increasing D_{ac}, due to the fact that the elastic acoustic phonons generate back-scattering.

In this Section, we focus on the impact of the inelastic optical phonons on the transport properties of the vdW-TFET. Figure 6.10 reports the transfer characteristics for different values of the deformation potential D_{op}. The strength of the inelastic phonon scattering can largely impact on the subthreshold current, as the SS is substantially degraded when increasing D_{op}. To better appreciate the influence of

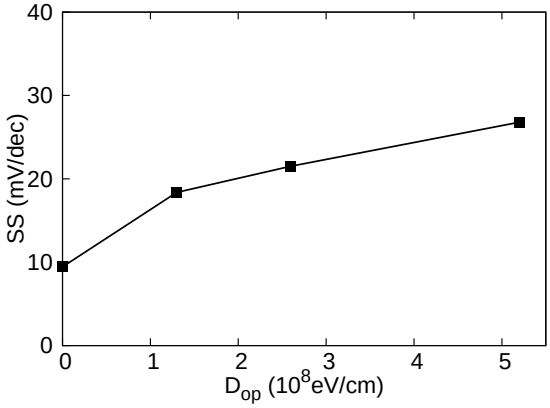

FIGURE 6.11: Average SS vs. D_{op} at V_{DS}= 0.3 V. SS is calculated with Eq.(5.4)

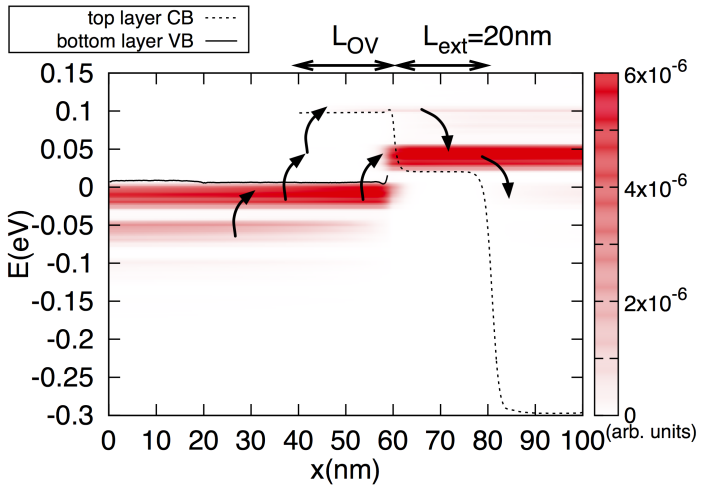

FIGURE 6.12: Energy spectrum of the transport current density and (dashed line) conduction and (solid line) valence band edges along the transport direction x in the presence of inelastic optical phonons with $D_{\text{op}} = 2.6\times10^8$ eV/cm, at V_{DS}=0.3 V and V_{TG}=-0.2 V. Phonon absorption in the source and overlap region and phonon emission in the drain are represented by arrows.

optical phonons, the average SS is calculated using the definition Eq.(5.4) and reported in Fig.6.11. Recalling that in the off-state, the conduction band of MoS_2 is higher than the valence band of WTe_2, as shown in Fig.6.2. Without the inelastic phonon, the electrons injected from source keep the same energy level, which is within the band gap of the MoS_2. Therefore, the off-current is strongly suppressed. However, with the inelastic optical phonon, the electrons are able to change their energy by interacting with the phonon. In order to visualize this effect and its impact, Fig.6.12 reports the spectral density of the current $J(x, E)$ versus the transport direction in the off-state for $D_{\text{op}} = 2.6 \times 10^8$ eV/cm, which is the effective D_{op} value for the longitudinal optical phonon mode in MoS_2 [158]. In this figure, $J(x, E)$ refers

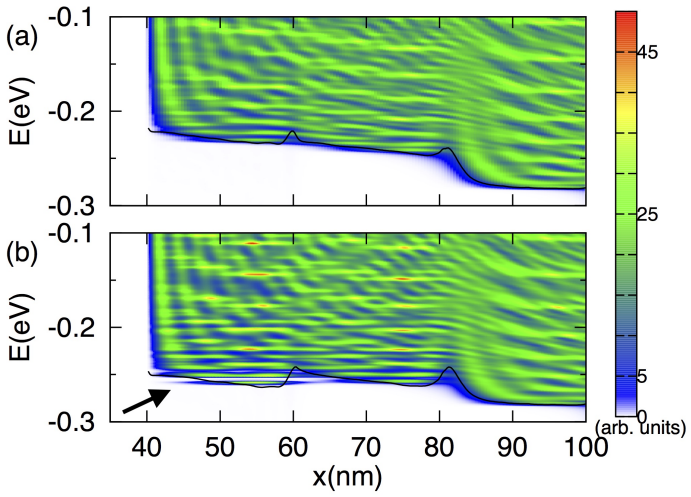

FIGURE 6.13: (colormap) LDOS in the top MoS_2 layer for the device with $L_{ext} = 20$ nm in Fig.6.3, and for (a) $V_{TG} = 0.3$ V and (b) $V_{TG} = 0.35$ V. Lines: top layer conduction band edge along the x direction.

to the current density that passes through a vertical plan perpendicular to the x-axis at the position x. The electrons are injected from the source (at x=0) into the valence band of WTe_2 layer. As can be seen, electrons gain energy *via* optical phonon absorption in the WTe_2 layer while traveling from source to the overlap region (from x=40 nm to x=60 nm), and tunnel into the top MoS_2 layer, where they release energy *via* optical phonon emission and arrive at the drain contact. By exchanging energy with the electrons, optical phonons promote the electrons to higher energy levels in the conduction band of MoS_2 thus making the interlayer tunneling possible in the off-state. For this reason, the optical phonons can enhance the off-state tunneling process, thus degrading the SS and increasing the off-current. On the other hand, the reduction in the on-state current with increasing D_{op} observed in Fig.6.10 is ascribed to the enhancement of the back-scattering induced by optical phonon, similar to the effect of elastic phonons.

6.3.5 Large overdrive regime

In Fig.6.3, at large V_{TG} values, some ripples are observed in the I_{DS} versus V_{TG} characteristics. We can elucidate this behavior by focusing on the simulation results for L_{ext}= 20 nm and considering the LDOS in the top MoS_2 layer for V_{TG}= 0.3 V and V_{TG}= 0.55 V (Fig.6.13). The increase of the top-gate voltage V_{TG} lowers the conduction band of the MoS_2 layer in the overlap region, forming a quantum well and creating localized states, as can be observed in the LDOS color map.

Moreover, as shown in Fig.6.14, the lowering of the top layer conduction band also moves down the energy window for tunneling. As the tunneling window approaches the Fermi level in the drain $E_{F,D} = -0.3$ eV, the I_{DS} current is degraded,

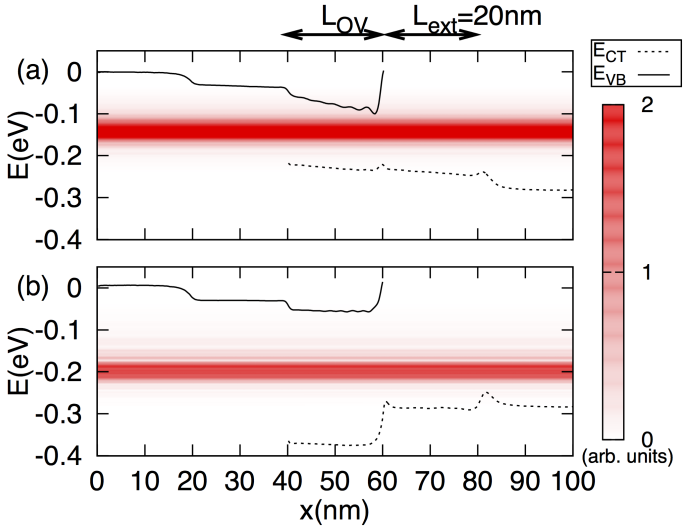

FIGURE 6.14: (colormap) Energy spectra of the transport current density in the device with $L_{\text{ext}} = 20$ nm in Fig.6.3, and for (a) $V_{\text{TG}} = 0.3$ V and (b) $V_{\text{TG}} = 0.55$ V. Continous (Dashed) lines: top layer conduction band edge (bottom layer valence band edge) along the x direction.

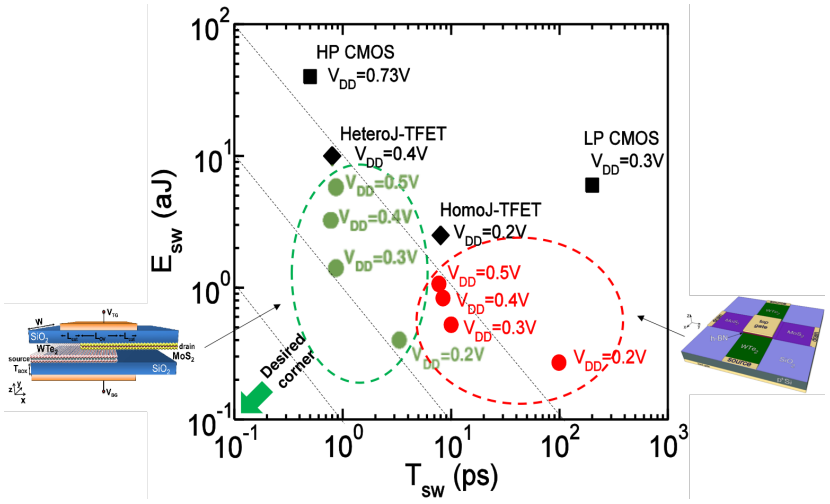

FIGURE 6.15: Comparison of the intrinsic switching energy and delay for the Van der Waals TFET and the inter-layer TFET with $V_{\text{DD}}$from 0.2 to 0.5 V.

which results in the negative trans-conductance observed in Fig.6.3 at large V_{TG} values. These effects at large top-gate voltage are observed also in the presence of inelastic optical phonon scattering, as shown in Fig.6.10.

6.4 Comparison of delay and energy metrics

In Fig.6.15, I plot E_{sw} vs. T_{sw} of the TFET in Chapter 6 and of the TFET in this Chapter, for different operating voltage V_{DD}. These two metrics are defined in Sec.5.3.5.

I also compare these two devices to high-power (HP) and low-power (LP) CMOS and to TFETs as reported in Refs. [148, 149]. As can be seen, the van der Waals TFET in this Chapter has a better switching time comparing the LP CMOS, the homojunction TFET and the TFET in the previous Chapter. The switching energy of the van der Waals TFET is slightly higher than the TFET in the previous Chapter, however it is still lower than the LP CMOS. Based on these two metrics, the van der Waals TFET in this Chapter is more suitable to work under V_{DD} in the range of 0.2-0.3 V rather than >0.4 V. The TFET in the previous Chapter is more competitive for the low power applications, because of its very low switching energy.

6.5 Summary

This Chapter presented the simulation results of a vertical van der Waals TFET based on 2D transition metal dichalcogenide in terms of performance and the possible optimization parameters. The 3-D NEGF-based quantum transport simulator includes both elastic and inelastic phonon scattering. In particular, Sec.6.3.1 showed that off-state current and SS can be dramatically improved with an appropriate engineering of the top gate extension region. In Sec.6.3.2, I have shown that the length of the overlap region between the two 2D layers has a small influence on SS and off-current I_{DS}due strong concentration of tunneling at the edge of the overlap region. However, very short overlap regions could entail strong quantum confinement effects and finally affect significantly the on-current. In Sec.6.3.3, simulations showed that an increase of the back-oxide thickness can degrade the current I_{DS} and the trans-conductance g_m of vdW-TFETs, but with a modest impact on the SS. Furthermore, in Sec.6.3.4 the simulations suggested that inelastic optical phonon scattering may have a profound impact on the off-state current and the SS of vdW-TFETs by activating possible paths for phonon assisted, inelastic tunneling processes.

The values of SS and current is confirmed by another recent study by Chen *et al.* [161] using a tight-binding (TB) Hamiltonian including spin-orbit coupling. Their TB parameters are well calibrated to match the band structure and effective mass from the DFT calculation. The similarity of results shows that the effective mass approximation used in our simulations can track pretty well the transport properties of the MoS_2 and WTe_2 monolayers with much less computational time and resources.

Chapter 7

Impact of rotational misalignment on the performance of vdW-TFETs

The derivation in the previous Chapter 6 assumes that there is a perfect rotational alignment between the top and bottom monolayers and tunneling occurs between equivalent valleys in the Brillouin zone, e.g. from a K to a K points (or from K' to K'). In this Chapter, the same vdW-TFET structure as in Chapter 6 is investigated by taking into account the rotational misalignment between the MoS_2 and WTe_2 monolayers as shown in Fig.7.1. Self-consistent 3-D quantum transport simulations are performed to investigate how such a misalignment affects the device performance.

This Chapter is organized as following. The geometrical structure of the rotated layers together with a model Hamiltonian are presented in Sec.7.1. This model Hamiltonian is used in the self-consistent 3-D quantum transport simulation in order to calculate the electron transport in the vdW-TFETs. The simulation results are reported in Sec.7.2, including the impact of rotation angle on the off- and on-state performance and the influence of inelastic optical phonon scatterings.

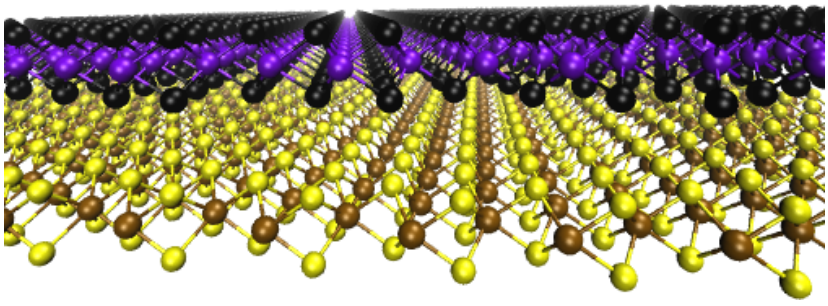

FIGURE 7.1: Sketch of the stacked MoS_2 and WTe_2 layers with a rotational misalignment in the simulations. The two monolayers are separated by a van der Waals gap of 0.6 nm.

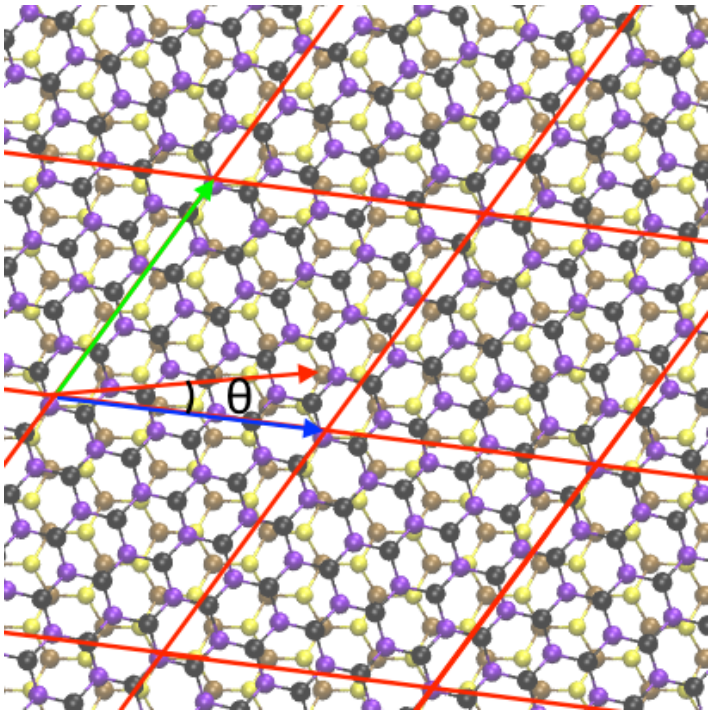

FIGURE 7.2: Atomistic structure of two monolayers with same lattice size and rotated by a small angle. The rotation turns the vector red to the vector blue. The red lines indicate that the bilayer system has a larger periodicity, with a super-cell defined by two new translation vectors: the green and blue arrows in the figure.

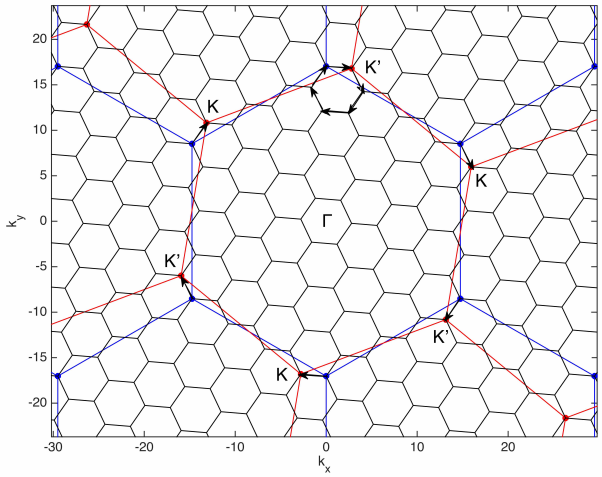

FIGURE 7.3: The Brillouin zones (red and blue hexagons) of the two monolayers , and the Brillouin zones (small black hexagons) of the super-cell of the bilayer system as defined in Fig.7.2.

7.1 Simulation model

The same device structure as in the previous Chapter (see Fig.6.1) is considered here, with the following geometry parameters $L_{\mathrm{OV}} = 20$ nm, $L_{\mathrm{ext}} = 5$ nm and $T_{\mathrm{BOX}} = 1$ nm. Figure 7.1 shows a partial sketch of the overlap region where the MoS_2 and the WTe_2 monolayers are overlapped and stacked with a rotation angle θ between them. Without the rotation, the two materials form a commensurate lattice with lattice parameter a_0=3.411 Å. This can be achieved by introducing a compressive strain on WTe_2 and tensile strain on MoS_2 layer as described in the previous Chapter. The van der Waals gap between the two monolayers is assumed to be 0.6 nm thick and with the same dielectric constant as air.

The lattices of the two rotated monolayers are sketched in Fig.7.2, with the relative rotation angle θ comprised between the red and the blue arrows in the figure. In general, the two lattices are not commensurate any more, and only for a certain values of θ, it is possible to define a super-cell for the two stacked layers. In Fig.7.2, the super-cells are indicated by the red lines with the two translation vectors indicated by the green and blue arrows. As we can see, the number of atoms within the super-cell depends on the rotation angle θ.

Figure 7.3 shows the rotated Brillouin zones of the two separate lattices (red and blue hexagons) and the smaller Brillouin zones of the super-cell (black hexagons). The conduction band in MoS_2 and the valence band in WTe_2 have valleys at the K and K' points located on the six corners of their hexagonal single-layer Brillouin zones, which are rotated by the angle θ around their common Γ point. The indirect band gaps between the two layers are indicated by the black arrows (shift vectors) in the same figure. The valleys of the MoS_2 and the WTe_2 are both folded onto the K and K' points of the super-cell Brillouin zone. After folding, the shift vectors fall along the six edges of the small hexagon.

For each pair of valleys, the following EMA model Hamiltonian is adopted

$$\mathbf{H_i}(\boldsymbol{k}) = \begin{bmatrix} E_0 + \frac{\hbar^2(\boldsymbol{k}-\boldsymbol{\Delta k_i})^2}{2m_{\mathrm{c}}} & t_\perp \\ t_\perp & -\frac{\hbar^2\boldsymbol{k}^2}{2m_{\mathrm{v}}} \end{bmatrix}, \tag{7.1}$$

where the parameters $t_\perp$, m_{c}, m_{v} and E_0 are defined in the same way as in Chapter 6. The new parameter $\boldsymbol{\Delta k_i}$ defines the shift vector of the corresponding valley couple. The six $\boldsymbol{\Delta k_i}$ vectors have the same norm but different directions separated by $\pi/3$ angle, as shown in Fig.7.3.

The wave-vector space Hamiltonian is converted into the real space representation by applying the quantum mechanics prescription $\boldsymbol{k} \rightarrow -\mathrm{i}\nabla$, and then it is discretized with the finite difference method. The transport problem is solved within the NEGF formalism. In the simulations, both elastic acoustic and inelastic optical phonon scatterings are taken into account within the SCBA described in Chapter 3.

The results of NEGF simulations allow us to obtain six charge density and current density contributions from those six pairs of valleys. The total charge and current in the device is the sum of them, then renormalized by three, due to the fact that only two valley couples (K and K') are actually "owned" by the Brillouin zone in the MoS_2 and WTe_2.

7.2 Results and discussions

In this Section, I will present the impact of the rotation angle on the device performance in Sec.7.2.1. The simulations include phonon scattering, with the acoustic deformation potential D_{ac}=3 eV and optical deformation potential $D_{\text{op}} = 2.6 \times 10^8$ eV/cm, with phonon parameters taken from the work of Kaasbjerg *et al.* [158]. In Sec.7.2.2, I study the impact of optical and acoustic phonon modes on the SS and I_{ON} by varying the value of D_{op} and D_{ac} respectively.

7.2.1 Effect of rotation angle

Figure 7.4(e) illustrates the transfer characteristic I_{DS}-V_{TG} in both linear and logarithmic scales for different rotation angles θ=0, 10.5°and 21°.

For a given top gate voltage V_{TG}, the rotational misalignment entails notable reduction on the current I_{DS}. As we expected, the rotation of one layer induces the indirect band gap that makes the interlayer tunneling more difficult, since a momentum change is requires for the electron to pass from one band to the other as shown in the panels (c, d) of Fig.7.4.

In the subthreshold regime, the current is suppressed by both the *interlayer* and the *intralayer* tunneling process, as discussed in the Sec.6.3.1. We can write the current as

$$I = I_0 T(\theta) e^{\beta L_{\text{ext}}(V_{\text{TG}} - V_{\text{T}})}, \tag{7.2}$$

where T is the interlayer tunneling probability and β is a qualitative factor for the intralayer tunneling process. T is a function of the rotation angle θ due to the indirect band gap. Figure 7.4 confirms that the rotational misalignment indeed has quite modest influence on the subthreshold slope, and a SS smaller than 60 mV/dec is observed for different θ. The steep slope is given by the intralayer tunneling mechanism, which is not influenced by the rotational misalignment. Figures 7.5 (a,b) show the tunneling current density in the off-state of the devices with θ=10.5°and θ=21°. In both cases, the tunneling occurs only on the edge of the overlap region, which is similar to the result obtained without the rotation misalignment.

After crossing the extrema of the conduction and the valence bands, the transport properties of the vdW-TFET depends a lot on the rotation angle. For a relatively small rotation angle ($\theta \leq 10°$), the two bands remain close. With helps of the elastic and inelastic phonon scatterings, the electrons can still tunnel from the valence band

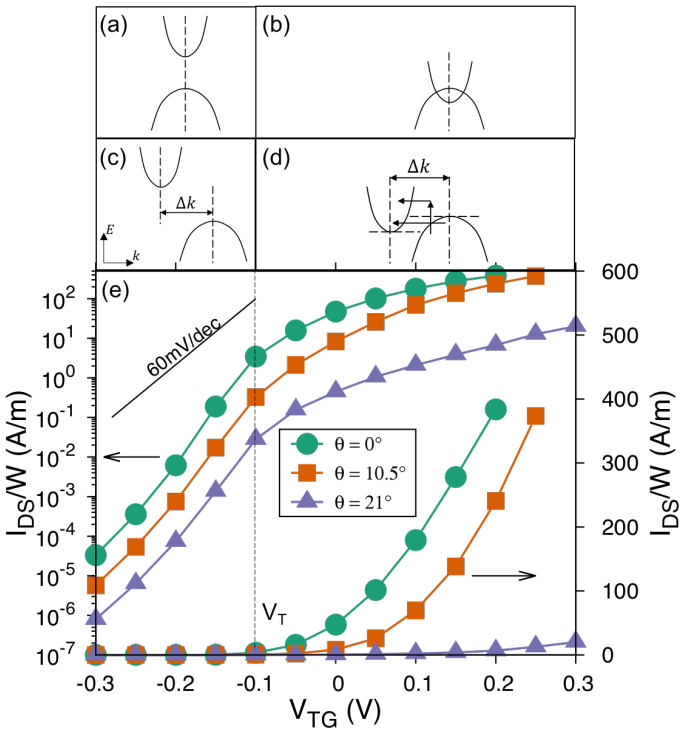

FIGURE 7.4: Schematics of the alignment of the MoS_2 conduction and WTe_2 valence bands (a, b) without and (c, d) with rotational misalignment. With the rotation, the band gap becomes indirect with a shift vector Δk. Panels (a, c) correspond to the subthreshold V_{TG}<V_T, and panels (b, d) correspond to V_{TG}>V_T. (e) I_{DS}/W vs. V_{TG} for different values of the rotation angles θ=0, 10.5°and 21°, at V_{DS}=0.3 V.

to the conduction band even when they do not cross each other, as indicated by the black arrows in Fig.7.4(d). Therefore, for the same $(V_{TG} - V_T)$ value, the current and the trans-conductance g_m=$[\partial I_{DS}/\partial V_{TG}]$ is similar with or without the rotational misalignment. The influence of the latter is similar to a threshold voltage shift.

However, if we continue increasing the rotation angle, the device on-state performance degrades radically. The current I_{DS} is already significantly reduced with a rotation angle of 21°. In this situation, the vdW-TFET cannot operate correctly in the optimal mode. Figure 7.5 reports the interlayer tunneling current density for the vdW-TFET in the OFF and ON state with θ=10.5°and θ=21°. Figure 7.5(c) shows that with a relatively small rotation angle the tunneling occurs inside the overlap area. However, if the rotation angle increases, the tunneling current turns out to be non-zero only very close to the edges of the overlap region, as shown in Fig.7.5(d). In addition to the indirect band gap induced by the rotation, this localized tunneling also decreases the current, thus resulting in very poor device performance, as observed in the IV figure 7.4.

The boundary condition on the edges of such small device generate sharp potential variation, which are similar to short-range scattering. Since the Fourier transform of a step-like function extends over a large range in the wave-vector domain, these

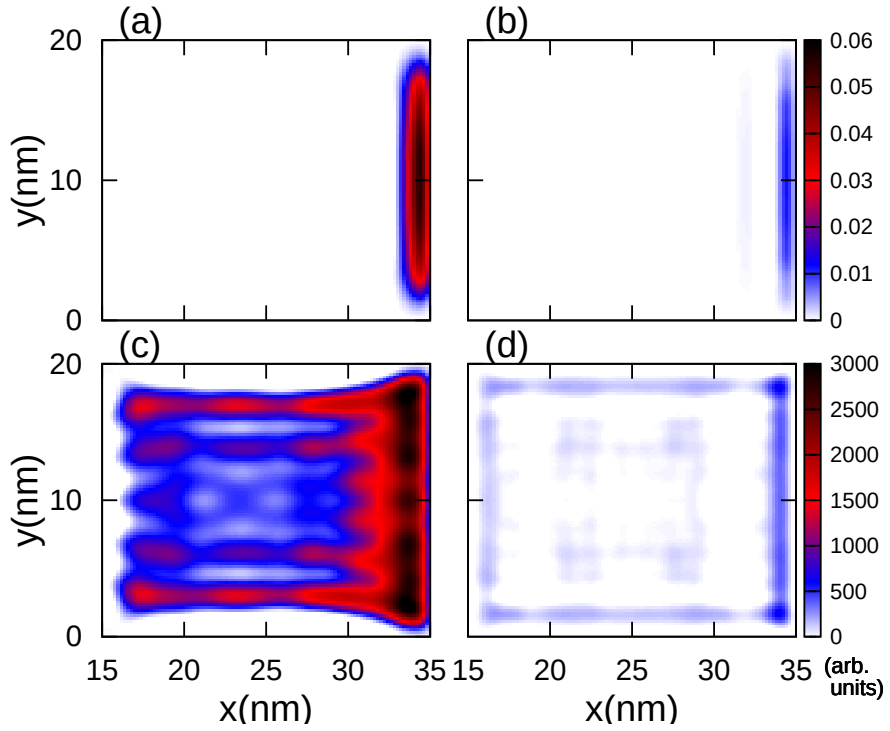

FIGURE 7.5: (colormap) Spatial distributions of the interlayer tunneling current density in the overlap region for V_{DS}=0.3 V. (a, c) θ=10.5°; (b,d) θ=21°; (a, b) V_{TG}=-0.2 V; (c, d) V_{TG}=0.2 V.

edges are able to change considerably the electron wave-vector and allow tunneling between the indirect valleys. In the center of overlap, the tunneling is very weak due to the fact that phonons alone are not enough to scatter the electrons over a large Δk.

In order to better illustrate this short-range scattering effect, a modified structure with a hole inside the overlap region has been simulated. This vdW-TFET has the same structure except that the MoS_2 and WTe_2 monolayers are cut and removed inside a square hole (4×4 nm) in the center of the overlap region (20×20 nm). All the other parameters are the same and the rotation angle θ=21°. In this simulation, I take the same electrostatic potential from the result in Fig.7.5(d) and disable the Schrödinger-Poisson self-consistent cycle, in order to compare the results under the exact same condition. Figure 7.6 reports the interlayer tunneling current density for this modified structure. Comparing to Fig.7.5(d), we can see additional concentration of tunneling around the hole. This result confirms the influence of the short-range scattering on the tunneling current for large rotation angles.

If we continue increasing V_{TG}, the conduction band and valence band will eventually cross each other. The needed energy shift ΔE for crossing depends on Δk,

$$\Delta E = \frac{\hbar^2}{m_v + m_c}\Delta k^2, \tag{7.3}$$

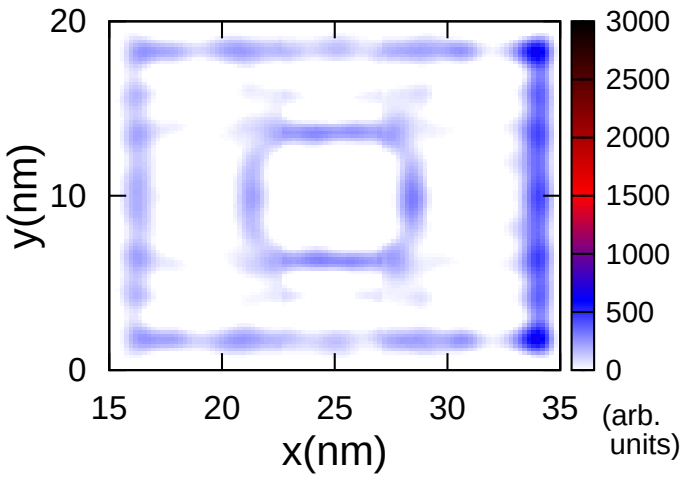

FIGURE 7.6: (colormap) Spatial distributions of the interlayer tunneling current density in the overlap region, with a modified structure containing a square hole in the center, for V_{DS}=0.3 V, V_{TG}=0.2 Vand θ=21°.

where m_v is the valence band effective mass of WTe_2 monolayer, m_c is the conduction band effective mass of MoS_2 monolayer. ΔE increases parabolically with Δk. In the V_{TG} ranged and the angles considered in these simulations presented, the devices with rotational misalignment never enter this working regime. For very small rotation angles, it is possible to enter this condition at a small V_{TG}. In this case, however, the effect on the transfer characteristic will be just a shift of the threshold voltage V_T.

7.2.2 Effect of phonons

The schematics in Fig.7.4 show that the phonon scattering can assist the tunneling process when the two layers are misaligned. In this Section, let us focus on the impact of the phonons on the transport properties of the vdW-TFET with a large rotation angle θ=21°.

Figure 7.7 reports the transfer characteristics for different values of D_{ac} and D_{op}. The strength of the phonon scatterings can substantially increase I_{DS} in the on-state. As indicated in Fig.7.4(d), two possible mechanisms can enhance the electron tunneling, either by exchanging energy with inelastic phonon to move up to a higher energy level, or by changing the wave-vector due to scatterings. Figure 7.7 indicates that the impacts of D_{ac} and D_{op} are very similar in the on-state, which suggests that the increase of I_{DS} is more likely due to the momentum scattering.

Figure 7.7(b) shows an imperceptible impact of D_{op} on the SS of the vdW-TFET, which is different from the previous results in Sec.6.3.4. With such a misalignment,

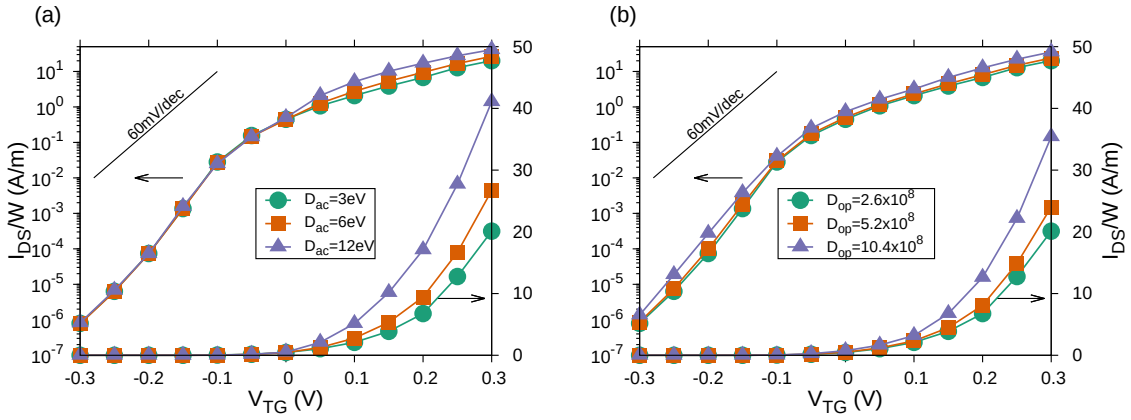

FIGURE 7.7: I_{DS}/W vs. V_{TG} for different values of (a) acoustic deformation potential D_{ac} and (b) optical deformation potential D_{op}, with the rotation angles θ=21°, at V_{DS}=0.3 V. The optical phonon energy is $\hbar\omega = 50$ meV. Other parameters are: $D_{ac} = 3$ eV, $L_{ext} = 5$ nm, $L_{OV} = W = 20$ nm, $T_{BOX} = 1$ nm.

the energy band gap in the off-state is increased following Eq.7.3 and becomes much larger than the optical phonon energy of monolayer MoS_2 [158]. Therefore, the inelastic phonon scattering has a quite modest impact on the vdW-TFET off-state performance when a large rotational misalignment is present in the device. As we have expected, the elastic acoustic phonons do not influence the subthreshold current since they do not change the electron energy and cannot promote inelastic tunneling.

7.3 Summary

The simulation results presented in this Chapter suggest that a possible rotational misalignment is expected to affect the absolute value of the tunneling current, but not to change significantly its dependence on the terminal voltages. The impact on SS is negligible for a modest rotational misalignment, only a variation of the threshold voltage is observed in this situation. However, the device performance starts to degrade rapidly by increasing the rotational misalignment angle. In this case, the electrons need the assistance of short-range scatterers to tunnel. When a rotational misalignment is present, the acoustic and optical phonons have a quite positive impact on the device transport properties by enhancing the tunneling process, without introducing noticeable degradation of SS.

In these simulations, important approximations are made in the use of the EMA Hamiltonian. The results are expected to be valid only for limited angles, since large angles could entail the involvement of other bands and valleys that are not considered in this simple model. The results in this Chapter can be seen as preliminary and exploratory work on the influence of rotational misalignment. More theoretical studies are needed in the future. Full band models, such as tight-binding, are

expected to give more accurate descriptions of the band structures. However, the computational complexity of these models could limit us from using them in the transport simulations.

From a technological viewpoint, if the stack of 2-D materials is obtained using a dry transfer method the rotational misalignment is inevitable [101, 162]. Experimental results have shown that, when the stack is obtained by using CVD techniques to grow one layer on top of the other, the two layers can have a fairly good angular alignment [163].

A publication reporting the results in this Chapter is currently under preparation.

Chapter 8

Conclusion and Outlook

In this thesis, a quantum simulator based on non-equilibrium Green's functions (NEGF) formalism was developed to simulate the carrier transport in a novel tunnel field-effect transistor structure with vertical heterojunction of two-dimensional materials, such as MoS_2 and WTe_2.

In Chapter 2, a brief introduction about the various types of 2-D materials, their synthesis and application was provided. In Chapter 3, the second quantization formalism was used for the Hamiltonian and for the definition of the Green's functions, then the NEGF formalism was concisely reviewed. The lesser Green's function contains information on the density of occupied states, and then it allows us to calculate the charge distribution inside the device and to evaluate self-consistently the potential profile for the electrons by means of the Poisson equation. From the charge continuity equation, it is possible to calculate the spectral current density flowing inside the nanodevice. The second quantization formalism and the Green's functions permit us to include many-body interactions, in particular the electron-acoustic-phonon and electron-optical-phonon interactions. The developed software takes advantage of the device slice structure. This allowed us to reduce considerably the rank of the matrices, and to make numerical investigation of device structures of realistic sizes. In Chapter 4, the code structure was reported briefly, with a description of the implemented adaptive energy integration method based on the adaptive Simpson scheme.

Two applications of theory and codes were reported and deeply analyzed. In Chapter 5, by using a 2-D version of the NEGF code, I investigated a vertical tunnel FET based on WTe_2 and MoS_2 monolayers with an h-BN interlayer. We predicted its extremely steep sub-threshold slope. This work has shown that a larger chemical doping in the top-layer and a more negative back-gate voltage can result in a well-behaved I_D versus V_{DS} characteristic at small V_{DS}. The top gate extension length has been found to be extremely important for a good sub-threshold slope and to limit the off-current. This work has also proven a good scalability of this device.

In Chapter 6, by using a 3-D version of the NEGF code, particular attention has been given to a vertical heterojunction TFET, where the interlayer tunneling barrier was replaced by the van der Waals gap between the 2-D monolayers of MoS_2

and WTe_2. This results in a thinner tunneling barrier and a larger on-current potentially expected for these devices. The results have confirmed that the off-state current and sub-threshold slope can be dramatically improved with an appropriate engineering of the top-gate extension. The length of the overlap region between the two 2-D monolayers has a small influence on sub-threshold slope and the current, because the current is strongly localized. This work not only demonstrated the ultra-steep subthreshold slope, but also provided a physical insight into the impact of the phonon scattering on the device performances. In particular, I showed that inelastic optical phonon may have a profound impact on the off-current by activating possible paths for phonon-assisted tunneling processes.

In Chapter 7, the effect of rotation misalignment within the two layers of the heterostructure was investigated with the inclusion of both elastic-acoustic- and inelastic-optical-phonon scatterings. This kind of misalignment is difficult to avoid in experiments. This work has shown that the device current can substantially depend on the rotation angle. However, the device can still offer a steep sub-threshold slope, thus representing a promising technology for future low-power digital electronics.

For these presented simulations, the most computational expensive part is the SCBA iteration. The good convergence is crucial for the current conservation. In order to accelerate the convergence of this part, I made some attempts that used the Broyden's method in numerical analysis, which is a quasi-Newton method for finding the roots of a function depending on n variables. The idea was to construct the Jacobian matrix for the SCBA cycle and to update the phonon self-energies along the gradient direction defined by this Jacobian. However, the major drawback of this attempt was the heavy memory requirement to store the Jacobien matrix, which was almost impossible for the inelastic-optical phonon case.

In the present simulator, the adaptive energy integration algorithm is limited to elastic electron-phonon coupling. The implementation is more complex if we want to include also the inelastic-optical phonon because different energy-levels need to be coupled together, and the energy mesh needs to be refined globally. As a result, the actual simulator uses a fixed energy mesh when we need to include the inelastic electron-phonon scattering. Further effort can be made to incorporate the adaptive mesh when inelastic phonons are taken into account.

In the present simulations, some many-body scattering effects have already been included, such as the electron-phonon and electron-electron Hartree interactions. With some further effort, it will be possible to include other sources of scattering, in particular short-range disorder and edge roughness. However, the simulations with such disorders are more memory demanding and more difficult to reach the convergence.

In conclusion, the theoretical and numerical results presented in this thesis provide both reliable performance predictions and insights of the working mechanisms of two novel structures of tunnel field effect transistor based on 2-D materials. In particular, the analysis revealed that carefully designed van der Waals TFETs can offer

excellent subthreshold swing values (<30 mV/dec) and represent a promising technology for future low-power nanoelectronics.

Bibliography

[1] P. Gargini, "ITRS Roadmap: 2013 Update", www.itrs.net (2013).

[2] F. Balestra, S. Cristoloveanu, M. Benachir, J. Brini, and T. Elewa, "Double-gate silicon-on-insulator transistor with volume inversion: A new device with greatly enhanced performance", IEEE Electron Device Letters **8**, 410–412 (1987).

[3] S. Cristoloveanu, J. Wan, and A. Zaslavsky, "A review of sharp-switching devices for ultra-low power applications", IEEE Journal of the Electron Devices Society **4**, 215–226 (2016).

[4] H. Lu and A. Seabaugh, "Tunnel field-effect transistors: State-of-the-art", IEEE Journal of the Electron Devices Society **2**, 44–49 (2014).

[5] A. C. Seabaugh and Q. Zhang, "Low-voltage tunnel transistors for beyond CMOS logic", Proceedings of the IEEE **98**, 2095–2110 (2010).

[6] T. N. Theis and P. M. Solomon, "In quest of the next switch: Prospects for greatly reduced power dissipation in a successor to the silicon field-effect transistor", Proceedings of the IEEE **98**, 2005–2014 (2010).

[7] C. Zener, "A Theory of the Electrical Breakdown of Solid Dielectrics", Proceedings of the Royal Society A: Mathematical, Physical and Engineering Sciences **145**, 523–529 (1934).

[8] J. J. Quinn, G. Kawamoto, and B. D. McCombe, "Subband spectroscopy by surface channel tunneling", Surface Science **73**, 190–196 (1978).

[9] T. Baba, "Proposal for Surface Tunnel Transistors", Japanese Journal of Applied Physics **31**, L455–L457 (1992).

[10] W. M. Reddick and G. A. J. Amaratunga, "Silicon surface tunnel transistor", Applied Physics Letters **67**, 494 (1995).

[11] W. Hansch, C. Fink, J. Schulze, and I. Eisele, "Vertical MOS-gated Esaki tunneling transistor in silicon", Thin Solid Films **369**, 387–389 (2000).

[12] C. Aydin, a. Zaslavsky, S. Luryi, S. Cristoloveanu, D. Mariolle, D. Fraboulet, and S. Deleonibus, "Lateral interband tunneling transistor in silicon-on-insulator", Applied Physics Letters **84**, 1780 (2004).

[13] D. Esseni, M. G. Pala, and T. Rollo, "Essential Physics of the OFF-State Current in Nanoscale MOSFETs and Tunnel FETs", English, IEEE Transactions on Electron Devices **62**, 3084–3091 (2015).

[14] D Esseni and M. G. Pala, "Interface Traps in InAs Nanowire Tunnel FETs and MOSFETs—Part II: Comparative Analysis and Trap-Induced Variability", Electron Devices, IEEE Transactions on **PP**, 1 (2013).

[15] D. Esseni and M. G. Pala, "Interface traps in InAs nanowire tunnel FETs and MOSFETs - Part II: Comparative analysis and trap-induced variability", IEEE Transactions on Electron Devices **60**, 2802–2807 (2013).

[16]D. Jena, "Tunneling transistors based on graphene and 2-D Crystals", Proceedings of the IEEE **101**, 1585–1602 (2013).
[17]M. O. Li, D. Esseni, G. Snider, D. Jena, and H. Grace Xing, "Single particle transport in two-dimensional heterojunction interlayer tunneling field effect transistor", Journal of Applied Physics **115**, 074508 (2014).
[18]A. Szabo, R. Rhyner, and M. Luisier, "Ab-initio simulations of MoS2 transistors: From mobility calculation to device performance evaluation", in Technical digest - international electron devices meeting, iedm, Vol. 2015-Febru, February (2015), pp. 30.4.1–30.4.4.
[19]A. Szabo, S. J. Koester, and M. Luisier, "Metal-dichalcogenide hetero-TFETs: Are they a viable option for low power electronics?", English, in Device research conference - conference digest, drc (2014), pp. 19–20.
[20]A. Szabo, S. J. Koester, and M. Luisier, "Ab-initio simulation of van der Waals MoTe2-SnS2 heterotunneling FETs for low-power electronics", IEEE Electron Device Letters **36**, 514–516 (2015).
[21]G. Pizzi, M. Gibertini, E. Dib, N. Marzari, G. Iannaccone, and G. Fiori, "Performance of arsenene and antimonene double-gate MOSFETs from first principles", Nature Communications **7**, 12585 (2016).
[22]F. W. Chen, H. Ilatikhameneh, T. A. Ameen, G. Klimeck, and R. Rahman, "Thickness Engineered Tunnel Field-Effect Transistors based on Phosphorene", IEEE Electron Device Letters **3106**, 1–1 (2016).
[23]R. Rahman, "Few-layer Phosphorene: An Ideal 2D Material For Tunnel Transistors", arXiv **6**, 1–15 (2015).
[24]F. Liu, Q. Shi, J. Wang, and H. Guo, "Device performance simulations of multilayer black phosphorus tunneling transistors", Applied Physics Letters **107**, 1–6 (2015).
[25]S.-c. Lu, M. Mohamed, and W. Zhu, "Novel vertical hetero- and homo-junction tunnel field-effect transistors based on multi-layer 2D crystals", 2D Materials **3**, 011010 (2016).
[26]T. Roy, M. Tosun, X. Cao, H. Fang, D.-H. Lien, P. Zhao, Y.-Z. Chen, Y.-L. Chueh, J. Guo, and A. Javey, "Dual-Gated MoS 2 /WSe 2 van der Waals Tunnel Diodes and Transistors", ACS Nano **9**, 2071–2079 (2015).
[27]R. Yan, S. Fathipour, Y. Han, B. Song, S. Xiao, M. Li, N. Ma, V. Protasenko, D. A. Muller, D. Jena, and H. G. Xing, "Esaki Diodes in van der Waals Heterojunctions with Broken-Gap Energy Band Alignment", Nano Letters **15**, 5791–5798 (2015).
[28]D. Sarkar, X. Xie, W. Liu, W. Cao, J. Kang, Y. Gong, S. Kraemer, P. M. Ajayan, and K. Banerjee, "A subthermionic tunnel field-effect transistor with an atomically thin channel", Nature **526**, 91–95 (2015).
[29]L. D. Landau and E. M. Lifshitz, *Statistical physics, part I*, 1980.
[30]L Landau, "Zur Theorie der Phasenumwandlungen II", Physik. Z. Sowjet **11**, 26–35 (1937).
[31]K. S. Novoselov, A. K. Geim, S. V. Morozov, D Jiang, Y Zhang, S. V. Dubonos, I. V. Grigorieva, and A. A. Firsov, "Electric Field Effect in Atomically Thin Carbon Films", Source: Science, New Series Gene Expression: Genes in Action **306**, 666–669 (2004).

[32]K. S. Novoselov, D Jiang, F Schedin, T. J. Booth, V. V. Khotkevich, S. V. Morozov, and A. K. Geim, "Two-dimensional atomic crystals", Proceedings of the National Academy of Sciences of the United States of America **102**, 10451–10453 (2005).
[33]A. J. Van Bommel, J. E. Crombeen, and A. Van Tooren, "LEED and Auger electron observations of the SiC(0001) surface", Surface Science **48**, 463–472 (1975).
[34]C. Oshima, A. Itoh, E. Rokuta, T. Tanaka, K. Yamashita, and T. Sakurai, "Hetero-epitaxial-double-atomic-layer system of monolayer graphene/monolayer h-BN on Ni(111)", Solid State Communications **116**, 37–40 (2000).
[35]A. H. Castro Neto, F. Guinea, N. M. R. Peres, K. S. Novoselov, and A. K. Geim, "The electronic properties of graphene", Reviews of Modern Physics **81**, 109–162 (2009).
[36]P. Miro, M. Audiffred, and T. Heine, "An atlas of two-dimensional materials", Chemical Society Reviews **43**, 6537–6554 (2014).
[37]A. Kara, H. Enriquez, A. P. Seitsonen, L. C. Lew Yan Voon, S. Vizzini, B. Aufray, and H. Oughaddou, *A review on silicene - New candidate for electronics*, 2012.
[38]M. Xu, T. Liang, M. Shi, and H. Chen, "Graphene-like two-dimensional materials", Chemical Reviews **113**, 3766–3798 (2013).
[39]S. Z. Butler, S. M. Hollen, L. Cao, Y. Cui, J. A. Gupta, H. R. Guti??rrez, T. F. Heinz, S. S. Hong, J. Huang, A. F. Ismach, E. Johnston-Halperin, M. Kuno, V. V. Plashnitsa, R. D. Robinson, R. S. Ruoff, S. Salahuddin, J. Shan, L. Shi, M. G. Spencer, M. Terrones, W. Windl, and J. E. Goldberger, "Progress, challenges, and opportunities in two-dimensional materials beyond graphene", ACS Nano **7**, 2898–2926 (2013).
[40]P. R. Wallace, "The band theory of graphite", Physical Review **71**, 622–634 (1947).
[41]J. W. McClure, "Band structure of graphite and de Haas-van Alphen effect", Physical Review **108**, 612–618 (1957).
[42]J. C. Slonczewski and P. R. Weiss, "Band structure of graphite", Physical Review **109**, 272–279 (1958).
[43]M. O. Goerbig, "Electronic properties of graphene in a strong magnetic field", Reviews of Modern Physics **83**, 1193–1243 (2011).
[44]K. S. Novoselov, A. K. Geim, S. V. Morozov, D Jiang, M. I. Katsnelson, I. V. Grigorieva, S. V. Dubonos, and A. A. Firsov, "Two-dimensional gas of massless Dirac fermions in graphene", Nature **438**, 197–200 (2005).
[45]Y. B. Zhang, Y. W. Tan, H. L. Stormer, and P. Kim, "Experimental observation of the quantum Hall effect and Berry's phase in graphene", Nature **438**, 201–204 (2005).
[46]R. Ribeiro-Palau, F. Lafont, J. Brun-Picard, D. Kazazis, A. Michon, F. Cheynis, O. Couturaud, C. Consejo, B. Jouault, W. Poirier, and F. Schopfer, "Quantum Hall resistance standard in graphene devices under relaxed experimental conditions", Nature Nanotechnology **10**, 1–18 (2015).
[47]X Du, I Skachko, A Barker, and E. Y. Andrei, "Approaching ballistic transport in suspended graphene", Nature nanotechnology **3**, 491–495 (2008).
[48]F. Schwierz, "Graphene transistors", Nature Publishing Group **5**, 487–496 (2031).

[49]Q. H. Wang, K. Kalantar-Zadeh, A. Kis, J. N. Coleman, and M. S. Strano, "Electronics and optoelectronics of two-dimensional transition metal dichalcogenides", Nature nanotechnology **7**, 699–712 (2012).
[50]X. Huang, Z. Zeng, and H. Zhang, "Metal dichalcogenide nanosheets: preparation, properties and applications.", Chemical Society reviews **42**, 1934–46 (2013).
[51]J. A. Wilson and A. D. Yoffe, "The transition metal dichalcogenides discussion and interpretation of the observed optical, electrical and structural properties", Advances in Physics **18**, 193–335 (1969).
[52]D. Voiry, A. Mohite, and M. Chhowalla, "Phase engineering of transition metal dichalcogenides.", Chemical Society Reviews **44**, 2702–12 (2015).
[53]J. E. Moore and L. Balents, "Topological invariants of time-reversal-invariant band structures", Physical Review B - Condensed Matter and Materials Physics **75**, 3–6 (2007).
[54]X. L. Qi, T. L. Hughes, and S. C. Zhang, "Topological field theory of time-reversal invariant insulators", Physical Review B - Condensed Matter and Materials Physics **78**, 1–43 (2008).
[55]D. Kong and Y. Cui, "Opportunities in chemistry and materials science for topological insulators and their nanostructures", Nature Chemistry **3**, 845–849 (2011).
[56]M. Z. Hasan and C. L. Kane, "Colloquium: Topological insulators", Reviews of Modern Physics **82**, 3045–3067 (2010).
[57]B. A. Bernevig, T. L. Hughes, and S. C. Zhang, "Quantum spin Hall effect and topological phase transition in HgTe quantum wells.", Science (New York, N.Y.) **314**, 1757–61 (2006).
[58]H. Zhang, C.-X. Liu, X.-L. Qi, X. Dai, Z. Fang, and S.-C. Zhang, "Topological insulators in Bi2Se3, Bi2Te3 and Sb2Te3 with a single Dirac cone on the surface", Nature Physics **5**, 438–442 (2009).
[59]D. Kong, W. Dang, J. J. Cha, H. Li, S. Meister, H. Peng, Z. Liu, and Y. Cui, "Few-layer nanoplates of Bi2Se3 and Bi 2Te3 with highly tunable chemical potential", Nano Letters **10**, 2245–2250 (2010).
[60]L. Li, Y. Yu, G. J. Ye, Q. Ge, X. Ou, H. Wu, and D. Feng, "Black Phosphorus Field-effect Transistors Black phosphorus field-effect transistors", Nature Nanotechnology **9**, 1–17 (2014).
[61]R. W. Keyes, "The electrical properties of black phosphorus", Physical Review **92**, 580–584 (1953).
[62]A. Carvalho, M. Wang, X. Zhu, A. S. Rodin, H. Su, and A. H. Castro Neto, "Phosphorene: from theory to applications", Nature Reviews Materials **1**, 16061 (2016).
[63]Y. Du, L. Yang, H. Zhou, and P. D. Ye, "Performance enhancement of black phosphorus field-effect transistors by chemical doping", IEEE Electron Device Letters **37**, 429–432 (2016).
[64]F Schwierz, R. Granzner, and J. Pezoldt, "Two-dimensional materials and their prospects in transistor electronics", Nanoscale **7**, 8261–8283 (2015).
[65]Y. P. V. Subbaiah, K. J. Saji, and A Tiwari, "Atomically Thin MoS2: A Versatile Nongraphene 2D Material", Advanced Functional Materials **26**, 2046–2069 (2016).
[66]K. Dolui, C. D. Pemmaraju, and S. Sanvito, "Electric field effects on armchair MoS 2 nanoribbons", ACS Nano **6**, 4823–4834 (2012).

[67] A. Kuc, N. Zibouche, and T. Heine, "Influence of quantum confinement on the electronic structure of the transition metal sulfide ts2", Physical Review B **83**, 245213 (2011).

[68] C. Gong, H. Zhang, W. Wang, L. Colombo, R. M. Wallace, and K. Cho, "Band alignment of two-dimensional transition metal dichalcogenides: Application in tunnel field effect transistors", Applied Physics Letters **103**, 53513 (2013).

[69] S. Ghatak, A. N. Pal, and A. Ghosh, "Nature of electronic states in atomically thin MoS2 field-effect transistors", ACS Nano **5**, 7707–7712 (2011).

[70] R. Fivaz and E. Mooser, "Mobility of charge carriers in semiconducting layer structures", Physical Review **163**, 743–755 (1967).

[71] F. Wang, Z. Wang, Q. Wang, F. Wang, L. Yin, K. Xu, Y. Huang, and J. He, "Synthesis, properties and applications of 2D non-graphene materials", Nanotechnology **26**, 292001 (2015).

[72] J. N. Coleman, M Lotya, A O'Neill, S. D. Bergin, P. J. King, U Khan, K Young, A Gaucher, S De, R. J. Smith, I. V. Shvets, S. K. Arora, G Stanton, H. Y. Kim, K Lee, G. T. Kim, G. S. Duesberg, T Hallam, J. J. Boland, J. J. Wang, J. F. Donegan, J. C. Grunlan, G Moriarty, A Shmeliov, R. J. Nicholls, J. M. Perkins, E. M. Grieveson, K Theuwissen, D. W. McComb, P. D. Nellist, and V Nicolosi, "Two-Dimensional Nanosheets Produced by Liquid Exfoliation of Layered Materials", Science **331**, 568–571 (2011).

[73] G. Cunningham, M. Lotya, C. S. Cucinotta, S. Sanvito, S. D. Bergin, R. Menzel, M. S. P. Shaffer, and J. N. Coleman, "Solvent exfoliation of transition metal dichalcogenides: Dispersibility of exfoliated nanosheets varies only weakly between compounds", ACS Nano **6**, 3468–3480 (2012).

[74] G. Eda, H. Yamaguchi, D. Voiry, T. Fujita, M. Chen, and M. Chhowalla, "Photoluminescence from chemically exfoliated MoS 2", Nano Letters **11**, 5111–5116 (2011).

[75] F. Torrisi, T. Hasan, W. Wu, Z. Sun, A. Lombardo, T. S. Kulmala, G. W. Hsieh, S. Jung, F. Bonaccorso, P. J. Paul, D. Chu, and A. C. Ferrari, "Inkjet-printed graphene electronics", ACS Nano **6**, 2992–3006 (2012).

[76] X. Li, W. Cai, J. An, S. Kim, J. Nah, D. Yang, R. Piner, A. Velamakanni, I. Jung, E. Tutuc, S. Banerjee, L. Colombo, and R. Ruoff, "Large area synthesis of high quality and uniform graphene films on copper foils", Science **324**, 1312–1314 (2009).

[77] X. Li, W. Cai, L. Colombo, and R. S. Ruoff, "Evolution of graphene growth on Ni and Cu by carbon isotope labeling", Nano Letters **9**, 4268–4272 (2009).

[78] K. Xu, Z. Wang, X. Du, M. Safdar, C. Jiang, and J. He, "Atomic-layer triangular WSe 2 sheets: synthesis and layer-dependent photoluminescence property", Nanotechnology **24**, 465705 (2013).

[79] Y. H. Lee, X. Q. Zhang, W. Zhang, M. T. Chang, C. T. Lin, K. D. Chang, Y. C. Yu, J. T. W. Wang, C. S. Chang, L. J. Li, and T. W. Lin, "Synthesis of large-area MoS 2 atomic layers with chemical vapor deposition", Advanced Materials **24**, 2320–2325 (2012).

[80] K. K. Liu, W. Zhang, Y. H. Lee, Y. C. Lin, M. T. Chang, C. Y. Su, C. S. Chang, H. Li, Y. Shi, H. Zhang, C. S. Lai, and L. J. Li, "Growth of large-area and highly crystalline MoS 2 thin layers on insulating substrates", Nano Letters **12**, 1538–1544 (2012).

[81]M. S. Driver, J. D. Beatty, O. Olanipekun, K. Reid, A. Rath, P. M. Voyles, and J. A. Kelber, "Atomic Layer Epitaxy of h-BN(0001) Multilayers on Co(0001) and Molecular Beam Epitaxy Growth of Graphene on h-BN(0001)/Co(0001)", Langmuir **32**, 2601–2607 (2016).

[82]A. T. Barton, R. Yue, S. Anwar, H. Zhu, X. Peng, S. McDonnell, N. Lu, R. Addou, L. Colombo, M. J. Kim, R. M. Wallace, and C. L. Hinkle, "Transition metal dichalcogenide and hexagonal boron nitride heterostructures grown by molecular beam epitaxy", Microelectronic Engineering **147**, 306–309 (2015).

[83]L Jiao, H. J. Liu, J. L. Chen, Y Yi, W. G. Chen, Y Cai, J. N. Wang, X. Q. Dai, N Wang, W. K. Ho, and M. H. Xie, "Molecular-beam epitaxy of monolayer MoSe2 : growth characteristics and domain boundary formation", New Journal of Physics **17**, 053023 (2015).

[84]H. J. Liu, L Jiao, L Xie, F Yang, J. L. Chen, W. K. Ho, C. L. Gao, J. F. Jia, X. D. Cui, and M. H. Xie, "Molecular-beam epitaxy of monolayer and bilayer WSe 2 : a scanning tunneling microscopy/spectroscopy study and deduction of exciton binding energy", 2D Materials **2**, 034004 (2015).

[85]H. C. Diaz, Y. Ma, R. Chaghi, and M. Batzill, "High density of (pseudo) periodic twin-grain boundaries in molecular beam epitaxy-grown van der Waals heterostructure: MoTe2/MoS2", Applied Physics Letters **108**, 1–6 (2016).

[86]F Bonaccorso, Z Sun, T Hasan, and A. C. Ferrari, "Graphene Photonics and Optoelectronics", Nature Photonics **4**, 611–622 (2010).

[87]G. Fiori, F. Bonaccorso, G. Iannaccone, T. Palacios, D. Neumaier, A. Seabaugh, S. K. Banerjee, and L. Colombo, "Electronics based on two-dimensional materials", Nature Nanotechnology **9**, 768–779 (2014).

[88]E. V. Castro, K. S. Novoselov, S. V. Morozov, N. M. R. Peres, J. M.B. L. Dos Santos, J. Nilsson, F. Guinea, A. K. Geim, and A. H. C. Neto, "Biased bilayer graphene: Semiconductor with a gap tunable by the electric field effect", Physical Review Letters **99**, 216802 (2007).

[89]R. Grassi, A. Gnudi, E. Gnani, S. Reggiani, and G. Baccarani, "Mode space approach for tight binding transport simulation in graphene nanoribbon FETs", IEEE Transactions on Nanotechnology **10**, 371–378 (2011).

[90]M. Gryglas-Borysiewicz, B. Jouault, J. TworzydłO, S. Lewińska, W. Strupiński, and J. M. Baranowski, "Transport properties of disordered graphene layers", Acta Physica Polonica A **116**, 838–840 (2009).

[91]R. Lv and M. Terrones, *Towards new graphene materials: Doped graphene sheets and nanoribbons*, 2012.

[92]P. Marconcini, A. Cresti, F. Triozon, G. Fiori, B. Biel, Y. M. Niquet, M. MacUcci, and S. Roche, "Atomistic boron-doped graphene field-effect transistors: A route toward unipolar characteristics", ACS Nano **6**, 7942–7947 (2012).

[93]R Bissessur, J Heising, W Hirpo, and M Kanatzidis, "Toward pillared layered metal sulfides. Intercalation of the chalcogenide clusters Co(6)Q(8)(PR(3))(6) (Q=S, Se, and Te and R=alkyl) into MoS2", Chem. Mater. **8**, 318–& (1996).

[94]V Podzorov, M. E. Gershenson, C Kloc, R Zeis, and E Bucher, "High-mobility field-effect transistors based on transition metal dichalcogenides", Applied Physics Letters **84**, 3301–3303 (2004).

[95] A. Ayari, E. Cobas, O. Ogundadegbe, and M. S. Fuhrer, "Realization and electrical characterization of ultrathin crystals of layered transition-metal dichalcogenides", Journal of Applied Physics **101**, 1–6 (2007).

[96] RadisavljevicB, RadenovicA, BrivioJ, GiacomettiV, KisA, B. Radisavljevic, A. Radenovic, J. Brivio, V. Giacometti, and A. Kis, "Single-layer MoS2 transistors", Nat Nano **6**, 147–150 (2011).

[97] H. Fang, S. Chuang, T. C. Chang, K. Takei, T. Takahashi, and A. Javey, "High-performance single layered WSe 2 p-FETs with chemically doped contacts", Nano Letters **12**, 3788–3792 (2012).

[98] S. B. Desai, S. R. Madhvapathy, A. B. Sachid, J. P. Llinas, Q. Wang, G. H. Ahn, G. Pitner, M. J. Kim, J. Bokor, C. Hu, and A. Javey, "MoS 2 transistors with 1-nanometer gate lengths", Science **354**, 99–102 (2016).

[99] A. K. Geim and I. V. Grigorieva, "Van der Waals heterostructures", Nature **499**, 419–425 (2014).

[100] S. C. Lu, M Mohamed, and W. J. Zhu, "Novel vertical hetero- and homo-junction tunnel field-effect transistors based on multi-layer 2D crystals", 2D Materials **3**, 6 (2016).

[101] L. Britnell, R. V. Gorbachev, R. Jalil, B. D. Belle, F. Schedin, a. Mishchenko, T. Georgiou, M. I. Katsnelson, L. Eaves, S. V. Morozov, N. M. R. Peres, J. Leist, a. K. Geim, K. S. Novoselov, and L. a. Ponomarenko, "Field-Effect Tunneling Transistor Based on Vertical Graphene Heterostructures", Science **335**, 947–950 (2012).

[102] K. I. Bolotin, K. J. Sikes, Z. Jiang, M. Klima, G. Fudenberg, J. Hone, P. Kim, and H. L. Stormer, "Ultrahigh electron mobility in suspended graphene", Solid State Communications **146**, 351–355 (2008).

[103] C. R. Dean, a. F. Young, I Meric, C Lee, L Wang, S Sorgenfrei, K Watanabe, T Taniguchi, P Kim, K. L. Shepard, and J Hone, "Boron nitride substrates for high-quality graphene electronics.", Nature nanotechnology **5**, 722–726 (2010).

[104] P. Avouris, "Graphene: Electronic and photonic properties and devices", Nano Letters **10**, 4285–4294 (2010).

[105] I Meric, M. Y. Han, A. F. Young, B Ozyilmaz, P Kim, and K. L. Shepard, "Current saturation in zero-bandgap, top-gated graphene field-effect transistors", Nature nanotechnology **3**, 654–659 (2008).

[106] V. E. Dorgan, A. Behnam, H. J. Conley, K. I. Bolotin, and E. Pop, "High-field electrical and thermal transport in suspended graphene.", Nano letters **13**, 4581–6 (2013).

[107] Y. Wu, X. Zou, M. Sun, Z. Cao, X. Wang, S. Huo, J. Zhou, Y. Yang, X. Yu, Y. Kong, G. Yu, L. Liao, and T. Chen, "200 GHz Maximum Oscillation Frequency in CVD Graphene Radio Frequency Transistors", ACS Applied Materials and Interfaces **8**, 25645–25649 (2016).

[108] B. Radisavljevic and A. Kis, "Mobility engineering and a metal-insulator transition in monolayer MoS2.", Nature materials **12**, 815–20 (2013).

[109] M. S. Fuhrer and J. Hone, "Measurement of mobility in dual-gated MoS2 transistors", Nature nanotechnology **8**, 146–7 (2013).

[110] Z. Yin, H. Li, H. Li, L. Jiang, Y. Shi, Y. Sun, G. Lu, Q. Zhang, X. Chen, and H. Zhang, "Single-layer MoS 2 phototransistors", ACS Nano **6**, 74–80 (2012).

[111]O. Lopez-Sanchez, D. Lembke, M. Kayci, A. Radenovic, and A. Kis, "Ultrasensitive photodetectors based on monolayer MoS2", Nature Nanotechnology **8**, 497–501 (2013).
[112]A Abderrahmane, P. J. Ko, T. V. Thu, S Ishizawa, T Takamura, and A Sandhu, "High photosensitivity few-layered MoSe2 back-gated field-effect phototransistors.", Nanotechnology **25**, 365202 (2014).
[113]N. Huo, S. Yang, Z. Wei, S.-S. Li, J.-B. Xia, and J. Li, "Photoresponsive and gas sensing field-effect transistors based on multilayer WS2 nanoflakes.", Scientific reports **4**, 5209 (2014).
[114]W. Zhang, M. H. Chiu, C. H. Chen, W. Chen, L. J. Li, and A. T. S. Wee, "Role of metal contacts in high-performance phototransistors based on WSe2 monolayers", ACS Nano **8**, 8653–8661 (2014).
[115]X. Hong, J. Kim, S.-F. Shi, Y. Zhang, C. Jin, Y. Sun, S. Tongay, J. Wu, Y. Zhang, and F. Wang, "Ultrafast charge transfer in atomically thin MoS2/WS2 heterostructures", Nature Nanotechnology **9**, 1–5 (2014).
[116]F. H. Koppens, T Mueller, P Avouris, a. C. Ferrari, M. S. Vitiello, and M Polini, "Photodetectors based on graphene, other two-dimensional materials and hybrid systems", Nat Nanotechnol **9**, 780–793 (2014).
[117]A. Castellanos-Gomez, M. Poot, G. A. Steele, H. S. J. Van Der Zant, N. Agraït, and G. Rubio-Bollinger, "Elastic properties of freely suspended MoS 2 nanosheets", Advanced Materials **24**, 772–775 (2012).
[118]J. Pu, Y. Yomogida, K. K. Liu, L. J. Li, Y. Iwasa, and T. Takenobu, "Highly flexible MoS 2 thin-film transistors with ion gel dielectrics", Nano Letters **12**, 4013–4017 (2012).
[119]M. Y. Zavodchikova, T. Kulmala, A. G. Nasibulin, V. Ermolov, S. Franssila, K. Grigoras, and E. I. Kauppinen, "Carbon nanotube thin film transistors based on aerosol methods.", Nanotechnology **20**, 085201 (2009).
[120]D.-m. Sun, M. Y. Timmermans, Y. Tian, A. G. Nasibulin, E. I. Kauppinen, S. Kishimoto, T. Mizutani, and Y. Ohno, "Flexible high-performance carbon nanotube integrated circuits", Nature Nanotechnology **6**, 156–161 (2011).
[121]M. S. Arnold, A. S. Green, J. F. Hulvat, S. I. Stupp, and M. C. Hersam, "Sorting carbon nanotubes by electronic structure using density differentiation", Nature nanotechnology **1**, 60–65 (2006).
[122]M. Singh, H. M. Haverinen, P. Dhagat, and G. E. Jabbour, "Inkjet printing-process and its applications", Advanced Materials **22**, 673–685 (2010).
[123]D. Kumar, "Brownian motion of a quantum particle", Physical Review A **29**, 1571–1573 (1984).
[124]W. C. S. P.Horwitz and Lawrence, *Quantum Statistical Mechanics* (Benjamin, 2009).
[125]S. Fujita, "Partial self-energy parts of Kadanoff-Baym", Physica **30**, 848–856 (1964).
[126]L. V. Keldysh, "Diagram Technique for Nonequilibrium Processes", Sov. Phys. JETP **47**, 1515–1527 (1964).
[127]E. N. Economou and M. H. Cohen, "Existence of Mobility Edges in Anderson's Model for Random Lattices", Physical Review B **5**, 2931–2948 (1972).
[128]G. D. Mahan, *Many-Particle Physics 3.rd* (Springer Science & Business Media, 2000), p. 785.

[129]M DiVentra, *Electrical Transport in Nanoscale Systems*, Vol. 14 (Cambridge University Press Cambridge, 2008), p. 496.
[130]G. Stefanucci and R. van Leeuwen, *Nonequilibrium Many-Body Theory of Quantum Systems: A Modern Introduction*, Vol. 54, 4 (Cambridge University Press, 2013).
[131]H. Haug, A.-P. Jauho, and M Cardona, *Quantum kinetics in transport and optics of semiconductors*, Vol. 2 (Springer, 2008).
[132]M Pourfath, *Non-equilibrium Green's Function Method for Nanoscale Device Simulation*, Vol. 2014 (Springer, 2014), pp. 9–28.
[133]A. Svizhenko, M. P. Anantram, T. R. Govindan, B. Biegel, and R. Venugopal, "Two-dimensional quantum mechanical modeling of nanotransistors", Journal of Applied Physics **91**, 2343–2354 (2002).
[134]M. P. Anantram, M. S. Lundstrom, and D. E. Nikonov, "Modeling of nanoscale devices", Proceedings of the IEEE **96**, 1511–1550 (2008).
[135]K Rogdakis, S Poli, E Bano, K Zekentes, and M. G. Pala, "Phonon- and surface-roughness-limited mobility of gate-all-around 3C-SiC and Si nanowire FETs", Nanotechnology **20**, 295202 (2009).
[136]A. Svizhenko and M. P. Anantram, "Role of scattering in nanotransistors", IEEE Transactions on Electron Devices **50**, 1459–1466 (2003).
[137]M. Frey, "Scattering in Nanoscale Devices", PhD thesis (2010).
[138]G. F. Kuncir, "Algorithm 103: Simpson's Rule Integrator", Communications of the ACM **5**, 347 (1962).
[139]J. N. Lyness, "Notes on the Adaptive Simpson Quadrature Routine", Journal of the ACM **16**, 483–495 (1969).
[140]L. F. Richardson, "The Approximate Arithmetical Solutions by Finite Differences of Physical Problems involving Differential Equations, with an Applications to the Stresses in a Masonry Dam", Philosophical Transactions of the Royal Society A **210**, 307–357 (1911).
[141]D. P. Laurie, "Calculation of Gauss-Kronrod quadrature rules", Mathematics of Computation **66**, 1133–1146 (1997).
[142]Clenshaw and Curtis, "A method for numerical integration on an automatic computer", Numerische Mathematik **31**, 197–205 (1960).
[143]T. Roy, M. Tosun, M. Hettick, G. H. Ahn, C. Hu, and A. Javey, "2D-2D tunneling field-effect transistors using WSe2/SnSe2 heterostructures", Applied Physics Letters **108**, 083111 (2016).
[144]J. Cao, M. Pala, A. Cresti, and D. Esseni, "Quantum simulation of a heterojunction inter-layer Tunnel FET based on 2-D gapped crystals", in Eurosoi-ulis 2015 - 2015 joint international eurosoi workshop and international conference on ultimate integration on silicon (2015), pp. 245–248.
[145]J. Cao, A. Cresti, D. Esseni, and M. Pala, "Quantum simulation of a heterojunction vertical tunnel FET based on 2D transition metal dichalcogenides", Solid-State Electronics **116**, 1–7 (2016).
[146]S. Poli, M. G. Pala, T. Poiroux, S. Deleonibus, and G. Baccarani, "Size dependence of surface-roughness-limited mobility in silicon-nanowire FETs", IEEE Transactions on Electron Devices **55**, 2968–2976 (2008).

[147]F. Conzatti, M. G. Pala, D. Esseni, E. Bano, and L. Selmi, "Strain-induced performance improvements in InAs nanowire tunnel FETs", IEEE Transactions on Electron Devices **59**, 2085–2092 (2012).
[148]M. O. Li, D. Esseni, J. J. Nahas, D. Jena, and H. G. Xing, "Two-dimensional heterojunction interlayer tunneling field effect transistors (Thin-TFETs)", IEEE Journal of the Electron Devices Society **3**, 200–207 (2015).
[149]D. E. Nikonov and I. A. Young, "Overview of beyond-CMOS devices and a uniform methodology for their benchmarking", Proceedings of the IEEE **101**, 2498–2533 (2013).
[150]J. Cao, D. Logoteta, S. Ozkaya, B. Biel, A. Cresti, M. Pala, and D. Esseni, "A computational study of van der Waals tunnel transistors: fundamental aspects and design challenges", in Iedm, international electron devices meeting (2015), pp. 313–316.
[151]J. Cao, D. Logoteta, S. Ozkaya, B. Biel, A. Cresti, M. G. Pala, and D. Esseni, "Operation and Design of van der Waals Tunnel Transistors: A 3-D Quantum Transport Study", IEEE Transactions on Electron Devices **63**, 4388–4394 (2016).
[152]E. Torun, H. Sahin, S. Cahangirov, A. Rubio, and F. M. Peeters, "Anisotropic electronic, mechanical, and optical properties of monolayer WTe2", Journal of Applied Physics **119**, 074307 (2016).
[153]M. K. Jana, A. Singh, D. J. Late, C. R. Rajamathi, K. Biswas, C. Felser, U. V. Waghmare, and C. N. R. Rao, "A combined experimental and theoretical study of the structural, electronic and vibrational properties of bulk and few-layer Td-WTe2.", en, Journal of physics. Condensed matter : an Institute of Physics journal **27**, 285401 (2015).
[154]A. Kumar and P. K. Ahluwalia, "Tunable dielectric response of transition metals dichalcogenides MX 2 (M=Mo, W; X=S, Se, Te): Effect of quantum confinement", Physica B: Condensed Matter **407**, 4627–4634 (2012).
[155]G. Kresse and J. Furthmüller, "Efficiency of ab-initio total energy calculations for metals and semiconductors using a plane-wave basis set", Computational Materials Science **6**, 15–50 (1996).
[156]P. E. Blöchl, "Projector augmented-wave method", Physical Review B **50**, 17953–17979 (1994).
[157]J. P. J. Perdew, K. Burke, and M. Ernzerhof, "Generalized Gradient Approximation Made Simple", Phys. Rev. Lett. **77**, 3865–3868 (1996).
[158]K. Kaasbjerg, K. S. Thygesen, and K. W. Jacobsen, "Phonon-limited mobility in n-type single-layer MoS 2 from first principles", Physical Review B - Condensed Matter and Materials Physics **85**, 115317 (2012).
[159]M. Schmidt, A. Schäfer, R. A. Minamisawa, D. Buca, S. Trellenkamp, J. M. Hartmann, Q. T. Zhao, and S. Mantl, "Line and point tunneling in scaled Si/SiGe heterostructure TFETs", IEEE Electron Device Letters **35**, 699–701 (2014).
[160]W. G. Vandenberghe, A. S. Verhulst, G. Groeseneken, B. Sorée, and W. Magnus, *Analytical model for point and line tunneling in a tunnel field-effect transistor*, 2008.
[161]F. Chen, H. Ilatikhameneh, Y. Tan, D. Valencia, G. Klimeck, and R. Rahman, "Transport in vertically stacked hetero-structures from 2D materials", arXiv preprint arXiv:1608.05057 **1**, 47906 (2016).

[162]L Britnell, R. V. Gorbachev, A. K. Geim, L. A. Ponomarenko, A Mishchenko, M. T. Greenaway, T. M. Fromhold, K. S. Novoselov, and L Eaves, "Resonant tunnelling and negative differential conductance in graphene transistors", Nature Communications **4**, 1794–1795 (1).

[163]S. Tiefenbacher, C. Pettenkofer, and W. Jaegermann, "Moire pattern in LEED obtained by van der Waals epitaxy of lattice mismatched WS2/MoTe2(0001) heterointerfaces", Surface Science **450**, 181–190 (2000).

List of publications in peer-reviewed journals and conference proceedings

[1]J. Cao, M. Pala, A. Cresti, and D. Esseni, "Quantum simulation of a heterojunction inter-layer Tunnel FET based on 2-D gapped crystals", in Eurosoi-ulis 2015 - 2015 joint international eurosoi workshop and international conference on ultimate integration on silicon (2015), pp. 245–248.

[2]J. Cao, M. Pala, A. Cresti, and D. Esseni, "Quantum simulation of tunnel field-effect transistors based on transition metal dichalcogenides", in Graphene 2015 (2015).

[3]J. Cao, D. Logoteta, S. Ozkaya, B. Biel, A. Cresti, M. Pala, and D. Esseni, "A computational study of van der Waals tunnel transistors: fundamental aspects and design challenges", in Iedm, international electron devices meeting (2015), pp. 313–316.

[4]J. Cao, A. Cresti, D. Esseni, and M. Pala, "Quantum simulation of a heterojunction vertical tunnel FET based on 2D transition metal dichalcogenides", Solid-State Electronics **116**, 1–7 (2016).

[5]J. Cao, D. Logoteta, S. Ozkaya, B. Biel, A. Cresti, M. G. Pala, and D. Esseni, "Operation and Design of van der Waals Tunnel Transistors: A 3-D Quantum Transport Study", IEEE Transactions on Electron Devices **63**, 4388–4394 (2016).

[6]M. G. Pala, C. Grillet, J. Cao, D. Logoteta, A. Cresti, and D. Esseni, "Impact of inelastic phonon scattering in the OFF state of Tunnel-field-effect transistors", Journal of Computational Electronics **15**, 1240–1247 (2016).

Acknowledgements

During three and half years, I had the pleasure to work at the IMEP-LAHC under the direction of Dr. Marco Pala. I would like to thank him for this opportunity, for his great professional competence and for the large freedom in my research work. I am also very grateful to Dr. Alessandro Cresti for co-supervising and guiding me throughout these years. My experience of working as a student of Dr. Pala and Dr. Cresti is a great treasure, which will benefit my whole life.

I wish to thank Prof. David Esseni for his active interest in this work, for his inception of great ideas and for devoting a lot of his precious time. I also wish to thank Dr. Blanca Biel and Dr. Sibel Özkaya for their work on the DFT simulations that allowed me to calibrate my simulation model.

I would like to address my sincere thanks to Dr. Demetrio Logoteta and Dr. Corentin Grillet for extensive discussions that we had together on diverse topics that helped me in developing many of the ideas in this thesis. I also address my sincere thanks to all the members (or ex-members) of the IMEP-LAHC for the time we spent together.

Finally, I express my deep gratitude to my parents, who always supported me during my studies, in the good and in the bad moments.